Thesis Report

Development Of A Preliminary Lifing Analysis Tool For The F135-PW-100 Engine

M.H. Jagtenberg

Technische Universiteit Delft

TUDelft Delft University of Technology

Challenge the future

THESIS REPORT

DEVELOPMENT OF A PRELIMINARY LIFING ANALYSIS TOOL FOR THE F135-PW-100 ENGINE

by

M.H. Jagtenberg

in partial fulfillment of the requirements for the degree of

Master of Science
in Aerospace Engineering

at the Delft University of Technology,
to be defended on Monday February 19, 2018.

Student number:	4081919	
Thesis committee:	Prof. dr. ir. P. Colonna,	TU Delft
	Dr. ir. W. P. J. Visser,	TU Delft
	Ir. P. C. Roling,	TU Delft
	Ir. E. R. Rademaker,	Nederlands Lucht- en Ruimtevaartcentrum

Front image taken at Royal Netherlands Air Force Open Days 2016, Leeuwarden.

Delft
University of
Technology

ABSTRACT

In the past the Netherlands Aerospace centre has aided the Royal Netherlands Air Force with life cycle and deterioration analysis work on the F100-PW-220 engine. The effects of the operating conditions on the engine components have been analysed and with this deterioration and life consuming mechanisms could be detected. Insight in these mechanisms proved to be of vital importance to asses possible consequences for the engine life cycle costs. In the near future the Royal Netherlands Air Force will replace the F-16 Fighting Falcons with the F-35 Lightning II's.

The objective of this research is to develop a preliminary lifing analysis tool for the F135-PW-100 engine first stage turbine rotor blades by designing a gas turbine simulation model coupled to a thermodynamic model and a lifing model. The development of the tool is based on open source data. Development of a lifing analysis tool could prove significant potential to enhance on-condition maintenance and it can be of vital importance to assess possible consequences for the engine life cycle costs. In this manner the maintenance cost can be minimized and component usage optimized.

The gas turbine simulation model has been designed in GSP using performance data from open source literature, theory to determine unknown engine characteristics and analysis by synthesis to optimize the design point. The model shows stable behaviour for the design point, as well as for afterburner mode and for off-design analysis. An inlet mass flow of $147\frac{kg}{s}$ and a fuel flow of $3.15\frac{kg}{s}$ is determined for a turbine inlet temperature of $2175K$. The amount of cooling air required is determined to be 25% of the core mass flow.

A heat transfer model has been developed in Matlab and Abaqus CAE. The temperatures have been derived from theory and the heat transfer coefficients have been estimated using Nusselt number correlations. The correlations found were suitable to integrate into the model, without knowing much about the geometry. Next to the heat transfer model, a thermodynamic model and lifing model have been developed in Abaqus CAE. For the thermo-mechanical model thermal loading en centrifugal loading are applied. The lifing model focusses on creep and low cycle fatigue as failure modes. Case studies have been performed to assess the effect of variations in the power setting, the amount of cooling air, the pattern factor and the TBC thickness. For all cases the trailing edge of the blade is found to be the most critical location.

The power setting is found to reduce the maximum temperature on the blade by 35%. The maximum Von Mises stress is reduced from $550MPa$ to $300MPa$. The creep strain rate shows similar results as the Von Mises stress. For take-off most part of the blade is able to sustain 73 cycles, for idle mode this is increased to 973 cycles until low cycle fatigue failure.

For the amount of cooling air used it is found that a 5% decrease in total amount of cooling air results in an increase of approximately 1% in the maximum blade temperature. No significant difference is found in the Von Mises stresses. The creep strain rate shows similar results as the Von Mises stress. When decreasing the amount of cooling air by 5% the amount of cycles to low cycle fatigue failure is reduced with 4%.

The pattern factor is found to reduce the maximum blade temperature by approximately 2% when decreasing the pattern factor by 5%. The temperatures on the root and tip of the blades have been increased by approximately 2%. No significant difference is found in the Von Mises stresses. Decreasing the pattern factor positively effects the creep strain rate. When decreasing the pattern factor by 5% a decrease of 12% is found for the cycles to low cycle fatigue failure.

For increasing the TBC thickness from $400\mu m$ to $600\mu m$ it is found that the maximum blade temperature is decreased by approximately 4%. No significant difference is found in the Von Mises stresses. Increasing the TBC thickness provides slightly lower creep strain rate results. When increasing the TBC thickness from $400\mu m$ to $600\mu m$ an increase of 18% is found for the cycles to low cycle fatigue failure.

For future research and development of the tool it is recommended to get access to performance data, material data and detailed geometry data of the rotor blades of the F135 engine. When this data is available, the gas turbine simulation model can be validated and more accurate life prediction can be provided. Regarding the detailed geometry it is advised to build a CFD model to perform the heat transfer analysis.

PREFACE

This thesis considers the development of a preliminary lifing analysis tool for the F135-PW-100 engine. The tool focusses on the first stage turbine rotor blades of the engine. This thesis report is a deliverable for fulfilling the degree of Master of Science in Aerospace Engineering at Delft University of Technology. The thesis assignment has been provided by the Netherlands Aerospace Centre. For this thesis I have interned at the Netherlands Aerospace Centre from May 2017 - February 2018 at their facility in Marknesse.

Over the last couple of months I have had the opportunity to work on a challenging project in a high-tech environment with intelligent, experienced and inspiring colleagues. I feel fortunate to have had this opportunity and therefore I would like to express my gratitude towards a number of people. First of all, I would like to thank Anneke Donker and Farid te Winkel for offering the possibility to perform my thesis at the Netherlands Aerospace Centre. Thanks to all my colleagues at the Netherlands Aerospace Centre from the AVGS department for a great time, and especially to Edward Rademaker, Oscar Kogenhop and Rob Brink for their knowledge and advise regarding the gas turbine simulation model, and Gerben van de Vrie and Rob Huls for their knowledge and advise regarding the mechanical model. Of course a big thanks to the colleagues participating in the daily soccer game during lunch brake. Thanks to Hotze Jongstra and Senne Sterk for carpooling the first couple of months.

Furthermore, I would like to thank my university supervisor Wilfried Visser for his time and interest. And also my gratitude towards the thesis comity for evaluating my work from an academic point of view.

On a more personal note I would like to thank Dirk and Karin Wiersma for offering a wonderful place to stay on their farm in Marknesse, my friends in Delft for making the past years as a student an amazing experience, my boyfriend Victor for his love and support and last but not least my mother, father and brother for their care, support and patience during my studies.

Michelle Jagtenberg
Marknesse, January 2018

NOMENCLATURE

ABBREVIATIONS

AB	Afterburner
BPR	Bypass Ratio
CFD	Computational Fluid Dynamics
CMC	Ceramic-Matrix Composite
CTOL	Conventional Take-off and Landing
CV	Carrier Version
DS	Directional Solidification
EB-PVD	Electron Beam Physical Vapor Deposition
EPR	Engine Pressure Ratio
EQ	Equiaxed
GSP	Gas turbine Simulation Program
HPC	High Pressure Compressor
HPT	High Pressure Turbine
ICME	Integrated Computational Materials Engineering
JSF	Joint Strike Fighter
LHV	Lower Heating Value
LP	Low Pressure
LPC	Low Pressure Compressor
LPT	Low Pressure Turbine
MX	Monochrystal
NGV	Nozzle Guide Vane
NLR	Netherlands Aerospace Centre
OEM	Original Equipment Manufacturer
OMC	Organic-Matrix Composite
OPR	Overall Pressure Ratio
P & W	Pratt & Whitney
PR	Pressure Ratio
RIT	Rotor Inlet Temperature
RNLAF	Royal Netherlands Air Force
RTDF	Radial Temperature Distribution Factor
SC	Single Crystal
SLS	Sea Level Static
STOVL	Short Take-off and Vertical Landing
TBC	Thermal Barrier Coating
TIT	Turbine Inlet Temperature
TOBI	Tangential On-Board Injection
TSFC	Thrust Specific Fuel Consumption

LATIN SYMBOLS

A	Area	m^2
BPR	Bypass Ratio	$[-]$
c	Characteristic Length	m
C	Constant	$[-]$
C_1, C_2, C_3	Absolute Velocity	$\frac{m}{s}$
C_P	Specific Heat at Constant Pressure	$\frac{J}{molK}$
D	Diameter	m
FN	Thrust	N
h	Heat Transfer Coefficient	$\frac{W}{m^2K}$
k	Conductivity	$\frac{W}{mK}$
L	Length	m
LHV	Lower Heating Value	$\frac{J}{kg}$
$\dot{m}$	Mass Flow	$\frac{kg}{s}$
M	Mach Number	$[-]$
N	Rotational Speed	RPM
N_{blades}	Number of Blades	$[-]$
N_f	Number of Cycles to Failure	$[-]$
N_{stages}	Number of Stages	$[-]$
Nu	Nusselt Number	$[-]$
OPR	Overall Pressure Ratio	$[-]$
P	Pressure	Pa
p_{blades}	Blade Pitch	$[-]$
Pr	Prandtl Number	$[-]$
PR	Pressure Ratio	$[-]$
$q"$	Heat Flux	$\frac{W}{m^2}$
Q_a	Activation Energy	J
r	Radius	m
R	Gas Constant	$\frac{J}{molK}$
R_D	Degree of Reaction	$[-]$
Re	Reynolds Number	$[-]$
RIT	Rotor Inlet Temperature	$[K]$
$RTDF$	Radial Temperature Distribution Factor	$[-]$
t	Thickness	m
T	Temperature	K
TIT	Turbine Inlet Temperature	K
$TSFC$	Thrust Specific Fuel Consumption	$\frac{kg}{Nh}$
Tu	Turbulence Intensity	$[-]$
U	Rotational Speed	$\frac{m}{s}$
V	Velocity	$\frac{m}{s}$
W	Mass Flow	$\frac{kg}{s}$
W_2, W_3	Relative Velocity	$\frac{m}{s}$
W_{compr}	Work Performed in Compressor Stage	J
W_{HPT}	Work Performed in HPT	J
WF	Fuel Mass Flow	$\frac{kg}{s}$

GREEK SYMBOLS

$\alpha_1, \alpha_2, \alpha_3$	Absolute Velocity Angle	$^\circ$
β	Dimensionless Map Parameter	$[-]$
$\beta_1, \beta_2, \beta_3$	Relative Velocity Angle	$^\circ$
ϵ	Emissivity	$[-]$
$\dot{\epsilon}$	Creep Strain Rate	$\frac{1}{s}$
η	Efficiency	$[-]$
κ	Heat Capacity Ratio	$[-]$
λ	Loading Factor	$[-]$
μ	Dynamic Viscosity	Pas
ϕ	Flow Coefficient	$[-]$
ρ	Density	$\frac{kg}{m^3}$
σ	Stress	MPa
σ_c	Stefan-Boltzmann Constant	$\frac{W}{m^2 K^4}$

CONTENTS

Abstract iii

Preface v

Nomenclature vii

1 Introduction 1
1.1 Problem Statement . . . 1
1.2 Research Objective . . . 1
1.3 Research Questions . . . 2
1.4 Methodology . . . 2
1.5 Report Structure . . . 3

2 Literature Study 5
2.1 JSF Program. . . . 5
2.2 F135-PW-100 Engine . . . 6
2.3 Novel Cooling Techniques . . . 7
2.4 Novel Materials and Coatings . . . 9

3 Engine Modelling 13
3.1 Gas turbine Simulation Program (GSP) . . . 13
3.2 Reverse Engineering . . . 14
3.2.1 Data From Open Source Literature. . . . 15
3.2.2 Unknown Data . . . 15
3.2.3 Analysis by Synthesis Using GSP . . . 18
3.3 Validation . . . 20
3.3.1 Design Point Simulation . . . 21
3.3.2 Afterburner Mode . . . 21
3.3.3 Off-Design Simulation . . . 22
3.4 Discussion on Engine Modelling. . . . 24
3.4.1 Discussion on Assumptions . . . 25
3.4.2 Sensitivity Analysis. . . . 26
3.4.3 GSP Accuracy . . . 26
3.5 Case Studies . . . 27

4 Heat Transfer Analysis 29
4.1 Heat Transfer Basics. . . . 29
4.2 Blade Design . . . 30
4.3 External Temperature Distribution . . . 31
4.4 External Heat Transfer Coefficient . . . 33
4.4.1 Velocity Profile . . . 34
4.4.2 Convection. . . . 34
4.4.3 Radiation . . . 35
4.4.4 Heat Transfer Coefficient Combined with TBC Properties . . . 36
4.5 Internal Heat Transfer Coefficient. . . . 37
4.5.1 Jet Impingement Cooling . . . 37
4.5.2 Channels With Turbulators . . . 38
4.5.3 Pin Fin Cooling . . . 38

4.6 Internal Temperature Distribution . . . 38
4.7 Film Cooling . . . 39
4.8 Results . . . 40
  4.8.1 Case Studies . . . 41
  4.8.2 Effect of Power Setting . . . 43
  4.8.3 Effect of Cooling Air . . . 44
  4.8.4 Effect of Pattern Factor . . . 45
  4.8.5 Effect of TBC Thickness . . . 46
4.9 Discussion on Heat Transfer Analysis . . . 46
  4.9.1 Discussion on Assumptions . . . 47
  4.9.2 Sensitivity Analysis . . . 49
  4.9.3 Future Research . . . 50

5 Lifing Analysis 51
5.1 Thermo-Mechanical Model . . . 51
5.2 Results Thermo-Mechanical Model . . . 52
  5.2.1 Effect of Power Setting . . . 53
  5.2.2 Effect of Cooling Air . . . 54
  5.2.3 Effect of Pattern Factor . . . 55
  5.2.4 Effect of TBC Thickness . . . 55
5.3 Lifing Model . . . 56
5.4 Results Lifing Model . . . 57
  5.4.1 Effect of Power Setting . . . 58
  5.4.2 Effect of Cooling Air . . . 59
  5.4.3 Effect of Pattern Factor . . . 60
  5.4.4 Effect of TBC Thickness . . . 61
5.5 Discussion on Lifing Analysis . . . 62
5.6 Future Research . . . 65

6 Conclusions and Recommendations 67
6.1 Conlusions . . . 67
6.2 Recommendations . . . 68

A Gas Turbine Simulation Program 71
A.1 Performance Simulation . . . 71
A.2 Solution Methodology . . . 72

B Load Cases Results from GSP 75

C Material Properties 77
C.1 CMSX-4 Properties . . . 77
C.2 TBC Properties . . . 78

Bibliography 79

1

INTRODUCTION

In assignment for Delft University of Technology and the Netherlands Aerospace Centre a thesis assignment has been performed covering the development of a preliminary lifing analysis tool for F135-PW-100 engine. This report will provide the reader with the work performed, results found and conclusions and recommendations that are drawn for this research. This chapter will introduce the reader with the problem statement at hand, the research objective and research questions and the methodology used. Furthermore, the report structure will be provided.

1.1. PROBLEM STATEMENT

In the near future the Royal Netherlands Air Force (RNLAF) will replace their fleet of F-16 Fighting Falcons with that of F-35 Lightning II's. For the F-16 the RNLAF was able and allowed to maintain the Pratt & Whitney F100-PW-220 engine in-house. The same is possible for the engine powering the F-35, the F135-PW-100 engine. This opens a window of opportunities.[1]

In the past the Netherlands Aerospace centre (NLR) has aided the RNLAF with life cycle and deterioration analysis work on the F100-PW-220 engine. The effects of the operating conditions on the engine components have been analysed and with this deterioration and life consuming mechanisms could be detected. Insight in these mechanisms proved to be of vital importance to asses possible consequences for the engine life cycle costs. The process of the previously designed tools by the NLR started with the recording of flight data, which was used as input for a gas turbine simulation model. The results of the gas turbine simulation model where coupled to a CFD model and a finite-elements model in order to determine the thermal and mechanical loading on engine components. Subsequently, the thermal and mechanical loadings were coupled to lifing models.

1.2. RESEARCH OBJECTIVE

Understanding the physical system of the engine allows for on-condition maintenance by relating the operational usage of the engine to the condition of a component. In this manner the down time of the engine can be minimized, consequently minimizing the maintenance costs and optimizing component usage. This research could prove significant potential to enhance on-condition maintenance and it can be of vital importance to assess possible consequences for the engine life cycle costs.

The objective of this research is therefore to develop a preliminary lifing analysis tool for the F135-PW-100 engine first stage turbine rotor blades by designing a gas turbine simulation model coupled to a thermodynamic model and a lifing model. The research objective can be further structured into several sub-goals. These are to get a physical understanding of the thermodynamic model of the F135, to analyse the sensitivity of components to the operational conditions and to assess the consequences for the component life.

1.3. RESEARCH QUESTIONS

In order to structure the methodology for this research to the research objective, one main research question and several research sub-questions are defined. These are formulated as follows.

1. To what extend can the methodology of previous lifing analysis as performed by the NLR be applied to this research?
2. What is the effect of the amount of cooling air used on component life?
3. What is the effect of the thickness of the thermal barrier coating on component life?
4. What is the effect of an improved combustor pattern factor on component life?
5. What is the effect of the power setting on component life?

These questions provide a basis for the steps to be taken in order to achieve the research objective. The objective is to develop a preliminary lifing analysis tool for the F135-PW-100 engine first stage turbine rotor blades by designing a gas turbine simulation model coupled to a thermodynamic model and a lifing model.

This tool could prove significant potential to enhance on-condition maintenance and it can be of vital importance to assess possible consequences for the engine life cycle costs.

1.4. METHODOLOGY

The methodology of this research is based on previous lifing analyses as performed by the NLR and is structured as follows. The first part of the research will focus on designing a gas turbine simulation model of the F135. For this purpose the Gas turbine Simulation Program (GSP) will be used. Little data about the F135 characteristics is available from the manufacturer and for this research only open source literature data will be used. It is well known though that it is a direct derivative of the F119 engine. From theory it can be related how the F119 could have been optimized and which novel cooling techniques, materials and coatings are available to do so. It is expected that based on analysis by synthesis, supported by theory, an accurate representation of the F135 engine can be reverse engineered. The output of this step will consist of performance data for each stage of the gas turbine.

For the second step of this research the focus will be on the high pressure turbine rotor blades. The input and output characteristics for this stage have been determined with the simulation model in GSP. Next the heat transfer characteristics of the rotor blade will have to be determined. For this purpose a heat transfer analysis tool will be programmed in Matlab, which will be coupled to the finite-elements program Abaqus CAE.

The last step of this research will consist of a thermal and stress analysis of the rotor blade using the finite-elements program Abaqus CAE. Through this last step it can be evaluated how parameters such as the power setting, the thermal barrier coating thickness, the turbine inlet temperature profile, or the amount of cooling air used influence the life of the rotor blade. In other words, a lifing analysis will be performed in this step. The methodology of this research is depicted in figure 1.1.

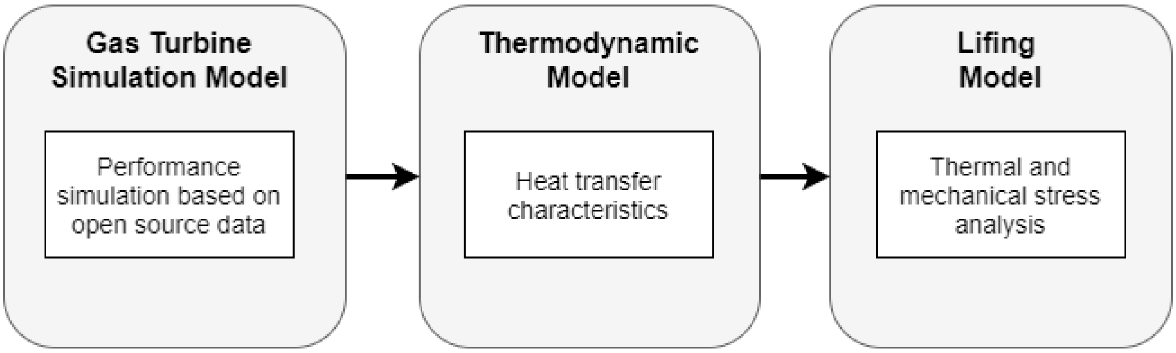
Gas Turbine Simulation Model
Performance simulation based on open source data
Thermodynamic Model
Heat transfer characteristics
Lifing Model
Thermal and mechanical stress analysis

Figure 1.1: Flow chart of the proposed research.

1.5. REPORT STRUCTURE

The structure of this report will follow similar process as described above for the methodology. Firstly the most important findings of the literature study will be provided in chapter 2. The modelling of the engine will be discussed in chapter 3. The theory, methodology and results for the heat transfer analysis will be provided in chapter 4. Subsequently, the preliminary lifing analysis for the first stage turbine rotor blade of the F135-PW-100 engine will be discussed in chapter 5. Lastly, the conclusions and recommendations drawn for this research will be provided in chapter 6.

2

LITERATURE STUDY

This chapter will provide background information for the proposed research. The highlights of the JSF program will be introduced. Data about the performance characteristics of the F135-PW-100 engine will be provided based on open source literature. Furthermore, background information regarding novel cooling techniques and novel materials and coatings will be provided.

2.1. JSF PROGRAM

The JSF program evolved from the growing need of tactical aviation to deploy fewer types of aircraft to reduce acquisition and operational costs. The main purpose of the program was to develop the next generation multi-role aircraft that could be produced in affordable variants to satisfy different operational requirements. [2] Also the program required the aircraft to fulfil both the divergent needs of the U.S. Air Force, the U.S. Marine Corps and the U.S. Navy. This ultimately let to the introduction of Lockheed Martin's F-35 Lightning II. The F-35 Lightning II is a 5th Generation fighter, combining advanced stealth with fighter speed and agility, fully fused sensor information, network-enabled operations and advanced sustainment. The three variants of the F-35, as shown in figure 2.1 will replace the legacy fighters for the U.S. Air Force, U.S. Marine Corps, U.S. Navy and several other countries including the Netherlands. The three variants consist of a conventional take-off and landing (CTOL) version, a carrier version (CV) and a short take-off and vertical landing (STOVL) version. The Royal Netherlands Air Force will acquire the CTOL, or A-variant. Currently, the JSF program is an internationally oriented program consisting of partnerships between the USA, Australia, Canada, Denmark, Italy, the Netherlands, Norway, Turkey and the UK. [3]

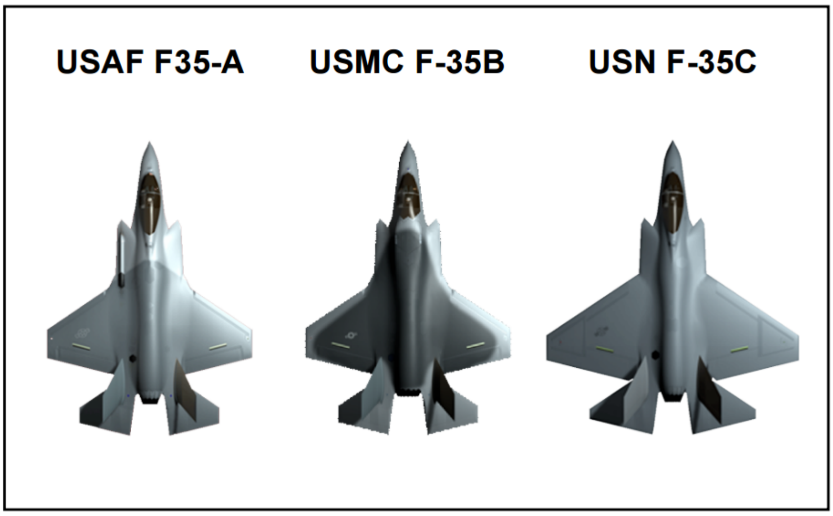

Figure 2.1: F35 Family [4].

2.2. F135-PW-100 ENGINE

The engine powering the F-35 CTOL variant is the F135-PW-100 engine, designed and manufactured by Pratt & Whitney. The F135 engine is a direct derivative of the F119-PW-100 engine that powers the F-22 Raptor. The F135 engine features advanced prognostics and health management systems, and the engine is designed to significantly lower maintenance costs.

The F135-PW-100 is a two-shaft low by-pass ratio augmented turbofan and has been directly derived from the F119-PW-100 engine. A layout of the engine is shown in figure 2.2. The engine consists of the following components. [5]

Intake

The intake consists of a ring containing 21 fixed radial guide vanes, with hinged trailing flaps. These vanes carry the front low pressure (LP) bearing.

Fan

The fan is also considered as the low pressure compressor (LPC). The fan consists of three integrally bladed rotors and is an improved version of the F119 with a higher mass flow and pressure ratio. Also stability, maximum resistance to bird strike and other impact damage has been improved and the fan is significantly lighter than its predecessors. The casing is made from organic-matrix composite (OMC) material. The first-stage vanes (stators) are made from hollow OMC. The second an third rotor are made of a flank-milled titanium alloy. The inlet diameter is $1.168m$, the rotor diameter is $1.100m$. The bypass ratio of the CTOL version is 0.57.

Compressor

The six-stage high pressure compressor (HPC), rotating in opposite direction of the LP spool, is also derived from the F119. The split forward case made from titanium alloy houses two stages of asymmetric variable-incidence guide vanes (stators). The rear stators are casted nickel-alloys and are grouped in segments in rings of titanium-alloy casings of high creep strength. All stators are integrally bladed, the same holds for the six rotors. The first two rotor stages are of damage-tolerant titanium alloy, the other four of high-strength nickel alloy. the overall diameter is $0.635m$, the mass flow for the CTOL version is $129.6kg/s$ and the overall pressure ratio (OPR) is 35.

Combustor

The short annular diffuser/combustor is also derived from the F119. The outer casing is approximately $0.762m$ both in diameter and in length and is capable of handling airflow at $4150kPA$ at $920K$. The combustion chamber itself is about $0.510m$ in diameter and $0.230m$ in length. At full power traversed by internal flow in $0.003s$. Impingement and film cooling are implemented in the liner. The liner also contains Floatwall ceramic-coated nickel-based cast segments. These segments are equipped with thousands of holes, which float from their anchored location. The fuel to air ratio is about 20% higher compared to the F100 engine, resulting in gas temperatures exceeding $2450K$.

High Pressure Turbine

The high pressure turbine (HPT) is single staged with novel airfoil coating and cooling, also based on the F119, but the cooling flow has been doubled. The impingement cooling is augmented by closing down the rear stator angles. The high-strength powder-metallurgy (sintered) high-rotor blades are made of a second-generation single-crystal nickel-based alloy, with advanced outer air seals. The diameter of the HPT is $0.914m$ and it rotates at speeds exceeding $15000RPM$, generating approximately $47725kW$ at a gas temperature over $1920K$. The HPT is cooled by air at $810K$ from the HPC. The rotor blades are cooled by Tangential On-Board Injection (TOBI) to minimize the pressure loss. Consequently, each blade is a complex casting with multiple cooling passages. A slow-responding thermally isolated support ring, selected because of their low thermal expansion, controls the growth in blade tip diameter. This provides passive clearance control through the normal engine-operating range.

Low Pressure Turbine

The low pressure turbine (LPT) is a two-stage design providing more shaft power compared to the single-stage LPT of the F119. It rotates in opposite direction of the HPT. The HPT operates at a temperature of approximately $1360K$ with minimum pressure loss. The casing is fabricated in refractory nickel and Pratt & Whitney proprietary materials.

Afterburner

The afterburner is a variable convergent-divergent nozzle with an advanced flame-holder system capable of handling large-volumes. It contains 15 hydraulically driven hinged flaps which control the propulsive jet at $621kPa$ at temperatures up to $2200K$. The hydraulic actuators vary in area and profile and assist bypass air to reduce the area when maximum loads are encountered.

Furthermore the engine has a maximum take-off thrust of $191.35kN$ and an intermediate thrust of $124.6kN$. The specific fuel consumption is approximately $20.46mg/Ns$. The main engine specifications as provided by Pratt & Whitney are shown in figure 2.3. [6]

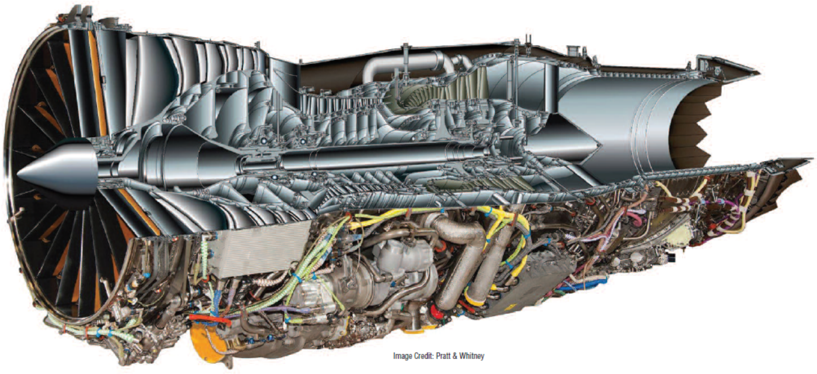

Figure 2.2: The F135-PW-100 engine from Pratt & Whitney. [6]

The high gas temperatures are expected to be possible by the use of optimal cooling techniques and superalloys protected by thermal-barrier coatings. This will be elaborated in the next sections.

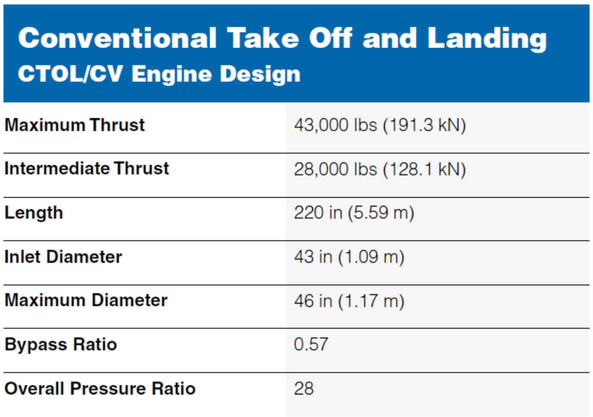

Conventional Take Off and Landing
CTOL/CV Engine Design

Maximum Thrust	43,000 lbs (191.3 kN)
Intermediate Thrust	28,000 lbs (128.1 kN)
Length	220 in (5.59 m)
Inlet Diameter	43 in (1.09 m)
Maximum Diameter	46 in (1.17 m)
Bypass Ratio	0.57
Overall Pressure Ratio	28

Figure 2.3: Performance characteristics of the F135 [6].

2.3. NOVEL COOLING TECHNIQUES

According to references the combustion process of the F135 can achieve record breaking temperatures exceeding $2450K$. [5] This can only be realised if advanced cooling techniques and novel materials are applied to the F135 engine. Several prognoses have been made in the past how new cooling techniques and materials will influence the performance of gas turbines, such as 2.4 and 2.5. [7]

In an interview with Jimmy Kenyon, Pratt & Whitney general manager of next generation fighter engines, it was mentioned that most part in advancing the rotor blades of the F135 lies in a proprietary new casting process for the nickel-alloy-based rotor blades. This casting process produces the passageways inside the blades in such a way, that the same amount of compressor bleed air can provide more cooling. The blades are also coated with a new thermal barrier material. [8]

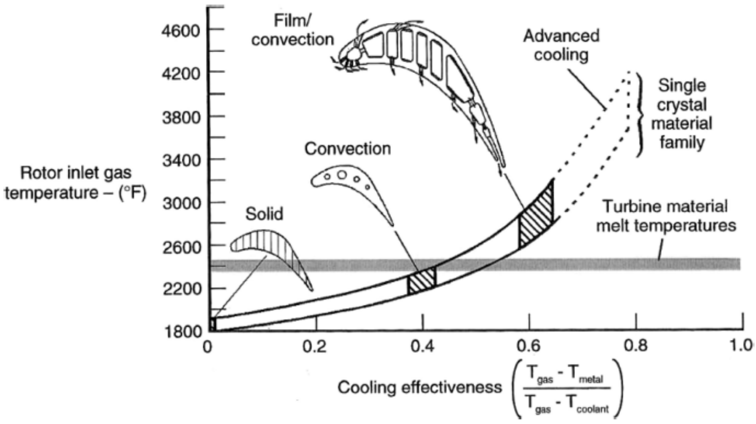

Figure 2.4: Turbine blade cooling technology: inlet gas temperature vs effectiveness. [7]

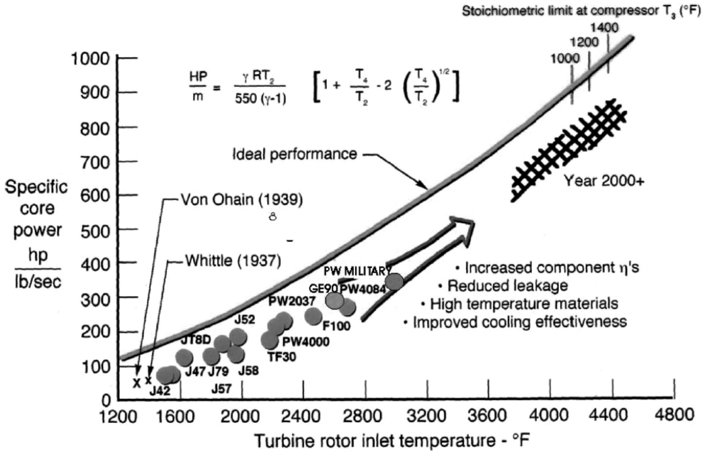

Figure 2.5: Core engine performance evolution. [7]

Based on this interview it can therefore be expected that no new cooling techniques are applied, but that the current advanced technologies are optimized. Current cooling techniques for turbines combines several cooling mechanisms. In figure 2.6 a schematic layout of these cooling mechanisms is shown. In figure 2.7 the internal structure of a high-pressure turbine blade is provided, showing the cooling distribution throughout the core of the blade airfoil and root. The cooling mechanisms can be divided into external and internal cooling mechanisms. The internal cooling mechanisms applied are impingement cooling at the blade leading edge and forced convection through the blade internal passages. To enhance the heat transfer through the internal passages, turbulence promoters and pin fins are included. The external cooling mechanism applied is mostly film cooling and trailing edge ejection.

Furthermore, according to [9], super cooling techniques are used. The proprietary concept 'super cooling' allows to more efficiently use cooling air diverted from the compressor for thermal control in turbine blades. Two sets of cooling tests have been conducted. One where super cooling's performance was examined in reducing high-pressure turbine blade and vane temperatures. And another where it was examined how well a second improved cooling process fared when used to enhance the uniformity of hot gasses exiting the combustor. Using computational fluid dynamics codes, engineers were able to improve the direction and shape of the cooling air entering the combustor and this helped flatten the temperature profile of the hot gas. This improved the combustor's pattern factor by as much as 30% in the impingement film floatwall combustor. P & W claims the engine ran at temperatures $810-920K$ hotter than the melting temperature of the metal used to make the turbine blades.

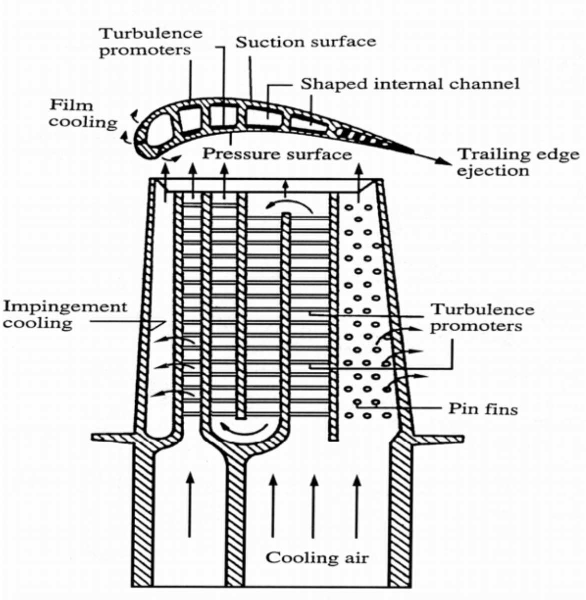

Figure 2.6: Cooling concepts of a modern multi-pass turbine blade. [10]

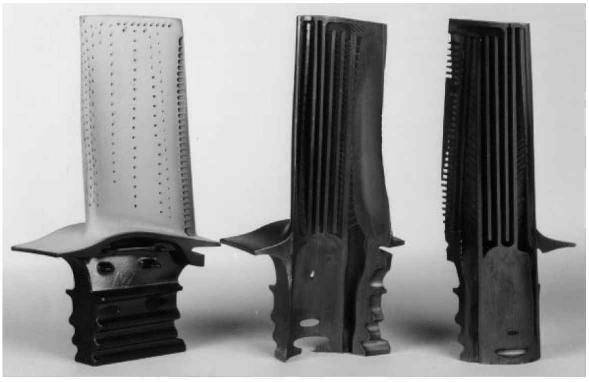

Figure 2.7: Courtesy Pratt & Whitney: Internal structure high-pressure turbine blade. [11]

Based on the literature available from Pratt & Whitney and the prognoses form literature it can be concluded that the state-of-the-art cooling techniques presented in figures 2.6 and 2.7 from references [10] and [11] have been optimized to so-called 'super-cooling' techniques, increasing the effectiveness of the passages, turbulators, pin fins, impingement cooling and film cooling. Next to this the combustor's pattern factor has been improved with 30%. According to Pratt & Whitney [9] this results in turbine temperatures $810-920K$ hotter than the melting temperature of the metal used to make the turbine blades. And according to [5] this results in an effective cooling flow that has been doubled with respect to its predecessors. For its predecessors rotor inlet temperatures exceeding $1920K$ were achieved and with the 'super cooling' technology even higher rotor inlet temperatures will be achieved [12].

In order to get a more exact approximation of the amount of cooling air used, figure 2.8 can be used. In this figure the amount of cooling air required for a certain pressure ratio and turbine inlet temperature is provided. It is assumed here that the blade metal temperature should not exceed $1200K$. Next to this it is also mentioned that air leakage between seals and bearings is unavoidable. [13] From reference [14] it can be estimated that the cooling mass flow of the F100 is between 15 and 25% of the core mass flow.

2.4. NOVEL MATERIALS AND COATINGS

As mentioned above, according to Pratt & Whitney the most part in advancing the rotor blades of the F135 lies in a proprietary new casting process for the nickel-alloy-based rotor blades. This casting process produces the passageways inside the blades in such a way, that the same amount of compressor bleed air will provide more cooling. The blades are also coated with a new thermal barrier material. [8] Pratt claims the engine runs at temperatures $810-920K$ hotter than the melting temperature of the metal used to make the turbine blades. [9] According to [5] the high-strength powder-metallurgy high-rotor blades are made of a second-generation single-crystal Ni-based alloy. This section will evaluate these statements based on theory from literature.

The introduction of single-crystal (SC) superalloys provides a significant increase in metal temperature capability. The single-crystal casting process eliminates all weaker grain boundaries and therefore improves resistance to creep, thermal fatigue and oxidation. Next to the single-crystal material capabilities, thermal barrier coatings have been developed for hot section airfoils to prevent oxidation [7] Considering that thermal barrier coatings can lower the temperature of a cooled blade by up to $443K$, while simultaneously reducing cyclic thermal strains, the importance of this technology cannot be underestimated. [15] High-temperature nickel-based superalloys together with coatings and cooling concepts have increased the temperature limits for turbine components, see figures 2.9 and 2.10. [16] [17] The abbreviations TBC and CMC in figure 2.9 stand

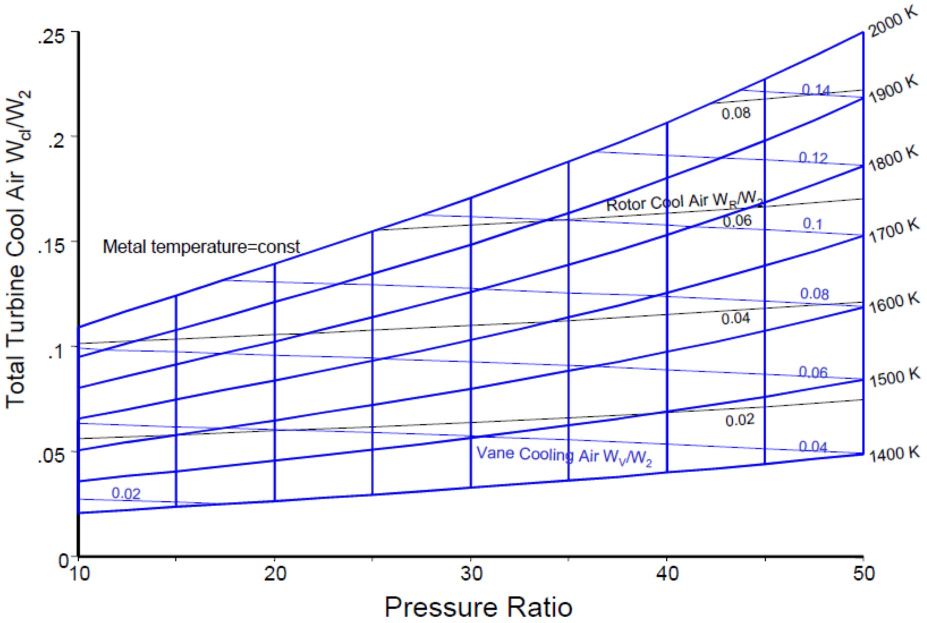

Figure 2.8: Total turbine cooling air required as function of pressure ratio and turbine inlet temperature for a metal temperature of 1200 K. [13]

for thermal barrier coating and ceramic-matrix composite, respectively. The abbreviations Eq, DS and MX in figure 2.10 stand for equiaxed, directional solidification and monocrystal, respectively. In figure 2.9 the blue horizontal line represents the expected rotor inlet temperature for the F135 engine. A schematic cross-section of a nickel-based superalloy including a thermal barrier coating is provided in figure 2.11.

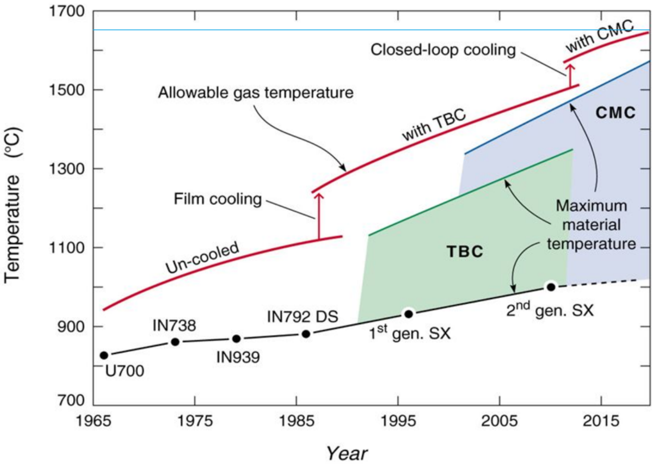

Figure 2.9: Evolution of propulsion materials, coatings and cooling concepts. [16]

Looking at the time line in figure 2.9, during the development of the F135, mostly second generation single-crystal superalloys are considered. In the case of P & W, the second generation single crystal superalloy is the $PWA1484$, which is also used in the $PW2000$ and $PW4000$ commercial engine family. A third generation single-crystal superalloy developed by P & W is used in the newest commercial engine models, the $PW1000G$ family. [5] For the F135 either an optimized second generation single-crystal superalloy or an early third generation single-crystal superalloy can be expected.

According to [18] low conductivity ceramic thermal barrier coatings are used in the F135 turbine, so no ceramic-matrix composite (CMC) is expected.

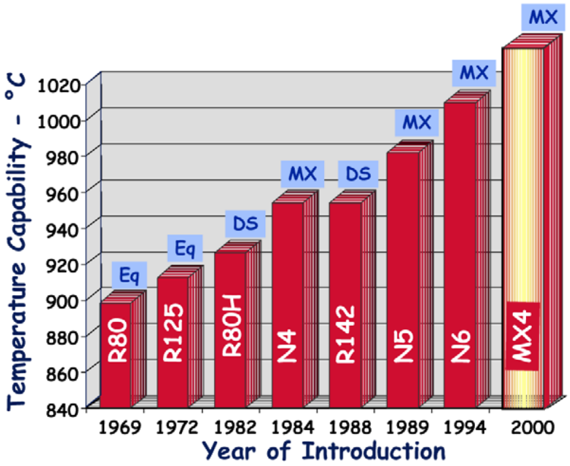

Figure 2.10: Temperature capability improvement for Nickel alloys over the years for constant rupture time at the same stress. [17]

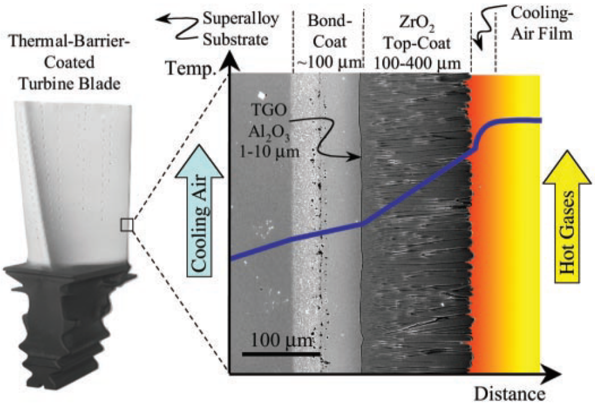

Figure 2.11: Cross-sectional scanning of temperature gradient throughout turbine blade. [19]

The advanced part of the single-crystal superalloys for the F135, lies in the casting process. A complete turbine airfoil, including cooling passages is casted by subjecting the part to heat and pressure, eliminating the internal porosity by compression. Modelling of the turbine airfoil castings was used in the development of the F135 engine to optimize the material properties. By predicting and controlling the casting microstructure and by eliminating the casting defects, enhanced capabilities are supported for service applications and cyclic missions where thermo-mechanical fatigue can significantly affect the component life. The tools used to achieve this are called integrated computational materials engineering (ICME). Modelling together with next generation turbine cooling schemes resulted in the F135 engine achieving the highest turbine inlet temperatures ever achieved in an operational gas turbine engine. [20] It is anticipated that the extensive research now in motion will yield incremental improvements which are required to take full advantage of saved cooling air. [15]

It can be expected that due to the proprietary new casting process, the layout of the internal cooling channel including turbulators and other heat transfer enhancing mechanisms, has been significantly optimized. This has led to an effective cooling flow that has been doubled with respect to its predecessor. It can be concluded from the prognoses in literature that the claimed combustion and turbine temperatures are plausible, be it for optimal conditions. Therefore the combustion temperature of approximately 2450K and rotor inlet temperature exceeding 1920K will be used to model the F135 engine.

3

ENGINE MODELLING

This chapter introduces the simulation program used for the analysis and provides the methodology and results for the reverse engineering of the F135-PW-100 engine based on data from open source literature and estimated values for the unknown data. A discussion on the validity of the simulation model will be elaborated. Next to this, the results for the design point simulation and off-design simulation will be provided. The chapter ends with an discussion of the accuracy of the GSP model.

3.1. GAS TURBINE SIMULATION PROGRAM (GSP)

For the simulation of the F135 engine, the gas turbine simulation program (GSP) will be used. The Gas turbine Simulation Program was developed at Delft University of Technology in 1986 based on NASA's DYNGEN program [21], as this program seemed to have problems with numerical stability and a poor user interface. Later at the NLR, the development of GSP continued in standard ANSI FORTRAN-5 and it was implemented on a powerful mainframe computer. Additional improvements, adjustments and extensions were applied. Currently GSP is a well-proven tool for detailed performance analysis of any kind of gas turbine. [22]

Basically, a gas turbine engine can be seen as a model of several components connected to each other in a mechanical or thermodynamic manner. In GSP, gas turbine models can be created by configuring several predefined components (like fans, compressors, combustors, turbines and nozzles) in a similar configuration as the gas turbine to be simulated. The inlet gas conditions of each component are formed by the exit gas conditions of the preceding component. Component maps and thermodynamic equations relate several parameters, such as air or gas properties, rotor speeds and efficiencies, in order to determine the processes in each component. From data specified by the user a predefined design point is determined. GSP calculates the deviation from the design point by solving a set of non-linear differential equations. These equations follow from the mass balance, the momentum balance and the energy balance for all components. Furthermore, the chemical gas processes in the combustor are implemented in a real gas model in GSP based on NASA's thermo-chemical gas model CEA (Chemical Equilibrium with Applications). [23] For more information about the modelling elements and numerical methods covering GSP, the reader is referred to Appendix A.

By connecting several components to each other in a mechanical or thermodynamic manner, the F135 is modelled in GSP. In figure 3.1 the layout of the GSP model is shown, as based on the information in section 2. The model consists of an inlet connected to a fan (LPC), which is consequently divided into a core side and a duct side. This division also takes into account the deviation in pressure ratio across the radius of the fan. The duct-side flow is transported via a duct and joined with the core flow again in the mixer. The core of the engine consists of a compressor (HPC), a combustion chamber, a high pressure turbine (HPT) and a low pressure turbine (LPT). After the core and duct flow are joined in the mixer, the model continues to the afterburner (AB) and the exhaust. The additional features in the model are the operational controllers. There are two bleed controllers, managing the bleed from the HPC used for cooling the turbines. There are two manual fuel controllers, managing the amount of fuel added to the main combustor and the afterburner. Lastly, there is a manual variable exhaust nozzle control, managing the exhaust nozzle area to prevent stalling of components upstream. Furthermore, each component and all the flows crossing the components are numbered.

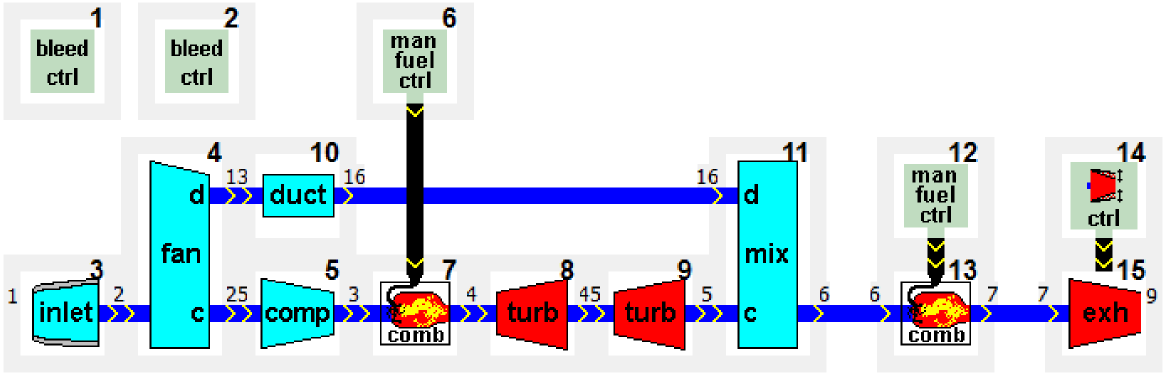

Figure 3.1: Layout of the F135 engine in GSP.

The state variables and error modes for the F135 GSP model are provided in table 3.1. As can be seen there are nine error equations. The state variables in table 3.1 count up to eleven, however the rotor speeds for the HPC and HPT are the same, which also holds for the rotor speeds of the fan and the LPT, giving also nine state-variables.

Table 3.1: State variables and error equations.

Component	**State variable**	**Error equation**
Inlet	$W_{2,corr}$	
Fan	N	$W - W_{c,map}$
	BPR_f	$W - W_{d,map}$
	$\beta_{c,map}$	
	$\beta_{d,map}$	
HPC	N	$W - W_{map}$
	β_{map}	
HPT	β_{map}	$W - W_{map}$
	N	$P_{shaft,req} - \Delta H_{del}$
LPT	β_{map}	$W - W_{map}$
	N	$P_{shaft,req} - \Delta H_{del}$
Mixer		$P_s ratio$
Exhaust nozzle		$W_{in} - W_{out}$

3.2. Reverse Engineering

Little data is known about the performance and characteristics of the F135 engine. In order to attain a simulation model of the F135 engine, reverse engineering will be applied. This part basically consists of the following three steps.

- Attaining and verifying engine data from open source literature.
- Approximating unknown engine parameters using theory.
- Applying analysis by synthesis to check with GSP if the estimated engine parameters lead to valid performance.

The first and second step of this part provide the inputs for the third step. Since the second step is an estimation, for some parameters this can result in a small range of values that can be used. In GSP a design series simulation can be applied to iterate for three different parameters within a provided range in a so-called loop case control. The estimated range found in the second step can thus be used as input for the iteration in the third step. The iteration in the third step can be converged to match a certain output parameter.

3.2.1. DATA FROM OPEN SOURCE LITERATURE

In chapter 2 background information on the F135 engine and its performance has been provided. The data found in Jane's [5] and from the OEM itself is basically the only reliable data that can be gathered for this research. These sources both provide the same data for most performance parameters, such as the engine bypass ratio (BPR), the dry thrust (neglecting a small conversion error in figure 2.3, where $28,000 lbs$ should equal $124.55 kN$ instead of $128.1 kN$) and the wet thrust. Therefore these performance parameters will be used for this research.

Both sources however provide a different value for the overall pressure ratio (Jane's provides a value of 35, whereas P & W provides a value of 28). It is expected that the OEM's data is more reliable. To support this expectation, a comparison is made with the engine's predecessors, the F100-PW-220 and the F119-PW-100 engines in table 3.2. Data for the F100 and F119 are based on information found in Jane's and a document on military engine acquisition by RAND [5] [12]. Comparing the overall pressure ratio for the F100 and F119 as stated in table 3.2 to the values provided by Jane's and P & W for the F135, a value of 28 would agree more to a development trend.

Table 3.2: Performance parameters of F100, F119 and F135 engine. [5] [12]

Parameter	F100	F119	F135	Unit
BPR	0.63	0.30	0.57	[−]
FN (dry)	64900	91190	124550	N
FN (wet)	105700	156000	191300	N
OPR	25	26	28	[−]
RIT	1700	1920	> 1920	K
W	102	123	$140 - 150$	$\frac{kg}{s}$
TSFC	0.074	0.082	> 0.085	$\frac{kg}{Nh}$
WF	1.3	2.1	> 3	$\frac{kg}{s}$

As explained in the previous section, due to the optimized casting which led to optimized cooling technology, a rotor inlet temperature exceeding $1920K$ is expected. As can be seen in table 3.2 this expectation is in line with the development trend.

The last columns in table 3.2 contain the inlet mass flow W, the thrust specific fuel consumption $TSFC$ and the fuel flow WF. The next subsection will elaborate on these parameters for the F135.

3.2.2. UNKNOWN DATA

For a quick and efficient design point iteration in GSP, it is preferred to have an initial estimate of the inlet mass flow, the turbine inlet temperature (and with that the fuel flow), the coolant air required and the efficiencies of the engine components.

An estimation of the inlet mass flow is attained using equation 3.1 for a range of Mach numbers and a range of inlet area. In equation 3.1 W is the mass flow, κ is the adiabatic exponent for air, R is the gas constant, M is the Mach number, A is the area, P_T is the total pressure and T_T is the total temperature. Based on a picture of the F35's inlet, the inlet area can be approximated. In a similar analysis for the F-16, the inlet Mach number was approximated to be 0.6. It is therefore assumed that the inlet Mach number of the F-35 will also be near this value. In figure 3.2 the inlet mass flow is plotted for a Mach number range of $0.4 - 0.7$ and an area range of $0.5 - 0.9 m^2$. The inlet mass flow of the F-16 and F-22 is also indicated in this figure. Based on this approximation an initial value of $140 \frac{kg}{s}$ is assumed for the inlet mass flow of the F-35.

$$W = \sqrt{\frac{\kappa}{R}} \frac{M}{(1 + \frac{\kappa - 1}{2} M^2)^{\frac{\kappa + 1}{2(\kappa - 1)}}} A \frac{P_T}{\sqrt{T_T}} \tag{3.1}$$

A further parameter analysis of the engine is performed by calculating the thrust as a function of inlet mass flow and turbine inlet temperature. A range of $140 - 160 \frac{kg}{s}$ is used for the inlet mass flow, based on the above advise. A range of $1900 - 2300K$ is used for the turbine inlet temperature, as based on the information found in open source literature. Also, the values for the OPR and BPR as found from open source literature are used for this analysis. The thrust is determined using equation 3.2, where $\dot{m}$ is the mass flow in $\frac{kg}{s}$, V_j and V_0 are the exit and inlet velocity in $\frac{m}{s}$, A_j is the exit area and P_j and P_0 are the exit and ambient pressure. Equation 3.2 is used for both the core as the bypass thrust. The mass flow can be determined using the BPR

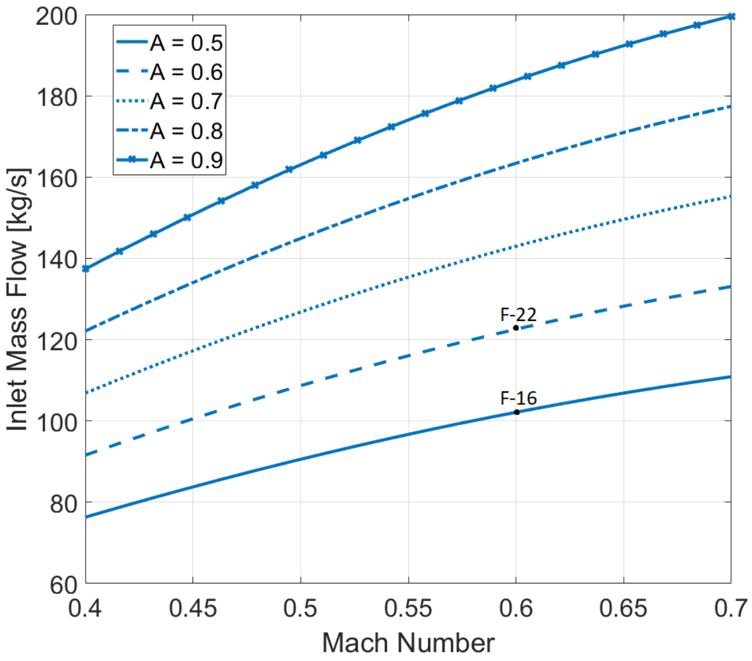

Figure 3.2: Inlet mass flow estimate related to inlet area and Mach number.

and adding the fuel flow to the core flow. In order to determine the exit velocity, area and pressure, stage calculations are performed.

$$F = \dot{m}(V_j - V_0) + A_j(P_j - P_0) \tag{3.2}$$

For the compression stage, the pressure is determined using equation 3.3 where OPR is the overall pressure ratio as found from literature and P_0 is taken as the ambient sea-level pressure. The total temperature can then be determined using isentropic relations, as shown in equation 3.4 where T_0 is taken as the ambient sea-level-static temperature, η_{compr} is the compression isentropic efficiency assumed as 0.85 and κ is the adiabatic exponent for air assumed as 1.4. The work performed in the compressor is expressed as in equation 3.5 where $C_{p,air}$ is the specific heat at constant pressure of air.

$$P_{03} = OPR \cdot P_0 \tag{3.3}$$

$$T_{03} = T_0(1 + \frac{1}{\eta_{compr}}((\frac{P_{03}}{P_0})^{\frac{\kappa-1}{\kappa}} - 1)) \tag{3.4}$$

$$W_{compr} = \dot{m_{core}} C_{P,air}(T_{03} - T_0) \tag{3.5}$$

$$WF = \frac{(TIT - T_{03})\dot{m_{core}} C_{P,gas}}{LHV \eta_{cc}} \tag{3.6}$$

In the combustion stage, the amount of added fuel flow is determined according to equation 3.6, where TIT is the turbine inlet temperature, $C_{P,gas}$ is the specific heat at constant pressure for the gas mixture, LHV is the lower heating value of the fuel assumed as $43 \cdot 10^6$ and η_{cc} is the combustion efficiency assumed as 0.995. The exit temperature and pressure of the turbine stage are determined using equations 3.7 and 3.8, where η_{mech} is the mechanical efficiency assumed as 0.995, PR_{cc} is the pressure ratio of the combustor assumed as 0.96, η_{turb} is the turbine isentropic efficiency assumed as 0.9 and for κ the adiabatic exponent for gas is assumed to be 1.33.

$$T_{05} = TIT - \frac{W_{compr}}{(\dot{m_{core}} + WF) C_{P,gas} \eta_{mech}} \tag{3.7}$$

$$P_{05} = P_{03} \cdot PR_{cc}(1 - (\frac{1}{\eta_{turb}}(1 - \frac{T_{05}}{TIT}))^{\frac{\kappa}{\kappa-1}}) \tag{3.8}$$

In the nozzle stage it is assumed that the nozzle is choked. The jet static pressure and temperature can then be determined using equations 3.9, 3.10 and 3.11, where the nozzle efficiency η_{nozzle} is assumed to be 0.99. Furthermore, the jet density, velocity and area are determined using equations 3.12, 3.13 and 3.14. These equations are also used to determine these parameters for the bypass. The thrust is estimated for a range of TIT from $1900-2300$ and a range of inlet mass flow of $140-160$ as shown in figure 3.3. From this figure it can be estimated that the inlet mass flow for the F135 lies in a range of $145-157\frac{kg}{s}$ and a turbine inlet temperature of $2000-2300K$.

$$P_j = \frac{P_{05}}{PR_{crit}} \tag{3.9}$$

$$PR_{crit} = \frac{1}{1 - \frac{1}{\eta_{nozzle}}(\frac{\kappa-1}{\kappa+1})^{\frac{\kappa}{\kappa-1}}} \tag{3.10}$$

$$T_j = T_{05}\frac{2}{\kappa+1} \tag{3.11}$$

$$\rho_j = \frac{P_j}{RT_j} \tag{3.12}$$

$$V_j = \sqrt{\kappa RT_j} \tag{3.13}$$

$$A_j = \frac{\dot{m_{core}} + WF}{\rho_j V_j} \tag{3.14}$$

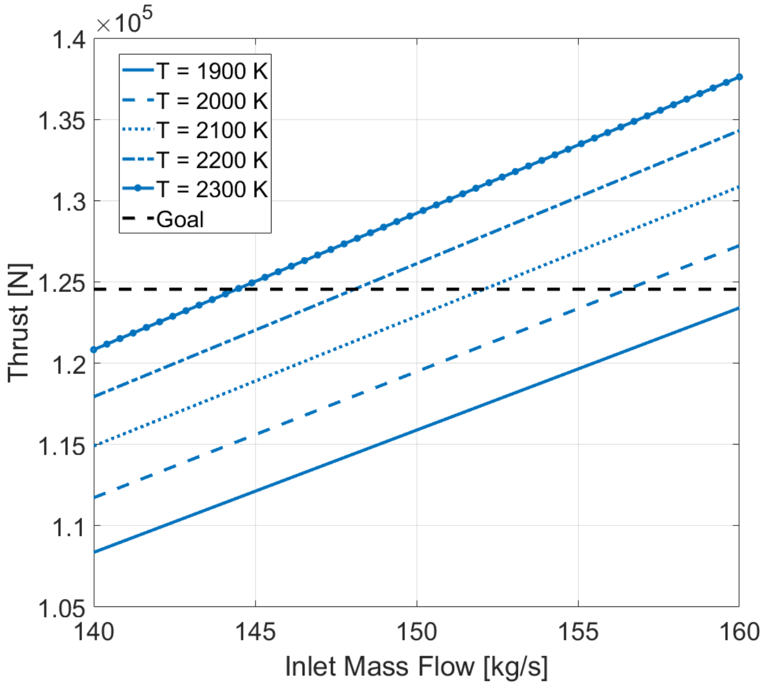

Figure 3.3: Thrust related to inlet mass flow and turbine inlet temperature.

The amount of cooling air required can be determined based on the methodology presented by Kurzke. [13] For this method the expansion process and cooling process are considered as separate processes. First the cooling of the vanes occurs, followed by the expansion, as depicted in figure 3.4. For a constant metal

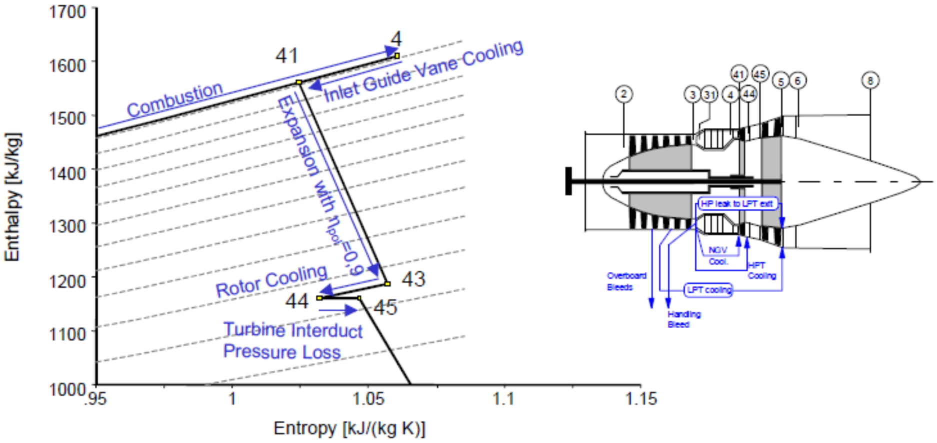

Figure 3.4: Enthalpy versus Entropy diagram for a cooled turbine. [13]

temperature the relative air mass flow is a function of the hot gas temperature and of the coolant temperature, which is a function of the cycle pressure ratio.

Kurzke empirically describes the cooling effectiveness of a row of blades or vanes by equation 3.15, where W_{cl} is the cooling mass flow, W_{ref} is the reference mass flow and C yields a constant which is valid for all sorts of cooling designs. For this kind of design studies, Kurzke advises to assume a value of 0.05 for this constant. Furthermore, the cooling effectiveness for a turbine nozzle guide vane (NGV) is provided in equation 3.16, where T_{t_4} is the turbine inlet temperature, T_{metal} is the metal temperature and T_{t_3} is the coolant temperature, which is assumed equal to the compressor exit temperature. For the rotor also equation 3.16 can be used, only then T_{t_4} is replaced by $0.9T_{t_{41}}$, where $T_{t_{41}}$ is the temperature entering the rotor stage and the factor 0.9 accounts for the translation from the static frame of reference to the rotating frame of reference in the rotor.

$$\eta_{cl} = \frac{\frac{W_{cl}}{W_{ref}}}{\frac{W_{cl}}{W_{ref}} + C} \tag{3.15}$$

$$\eta_V = \frac{T_{t_4} - T_{metal}}{T_{t_4} - T_{t_3}} \tag{3.16}$$

The above methodology is used to determine the required cooling for a range of pressure ratios and turbine inlet temperatures in order to keep a constant metal temperature of $1200K$. A temperature of $1200K$ is assumed based on the second generation single crystal material temperature as shown in figure 2.9 The turbine inlet temperature T_{t_4} is estimated at $2200K$, the coolant temperature is estimated at $800K$ and the rotor inlet temperature is estimated at $1900K$. The cooling air required is determined by setting equation 3.15 equal to 3.16. This resulted in the graph in figure 3.5, where the solid lines represent the total cooling air required, the dashed lines the NGV cooling required, and the dotted lines the rotor cooling required.

From figure 3.5 it can be seen that for the pressure ratio of the F135 of 28 and an expected TIT of $2200K$, approximately 12% cooling air is required for the NGVs and 6% for the rotor blades of the HPT. So a total amount of cooling air of 18% is required for the HPT. For the LPT, the coolant air is assumed to be taken halfway from the compressor, providing a pressure ratio of 15. The LPT inlet temperature is approximated to be $1670K$. Using figure 3.5, this means that approximately 4% cooling is required for the NGVs and 2% for the rotor blades. So a total amount of 6% cooling is required for the LPT.

3.2.3. ANALYSIS BY SYNTHESIS USING GSP

An analysis by synthesis method is applied in GSP using design series simulation with loop case controls. This means that a maximum of three parameters can be varied per design simulation. The goal of this step is to match the known performance parameters, as found from open source literature, within a 3% range. This means the BPR, OPR, and the wet and dry thrust will be used as matching parameters.

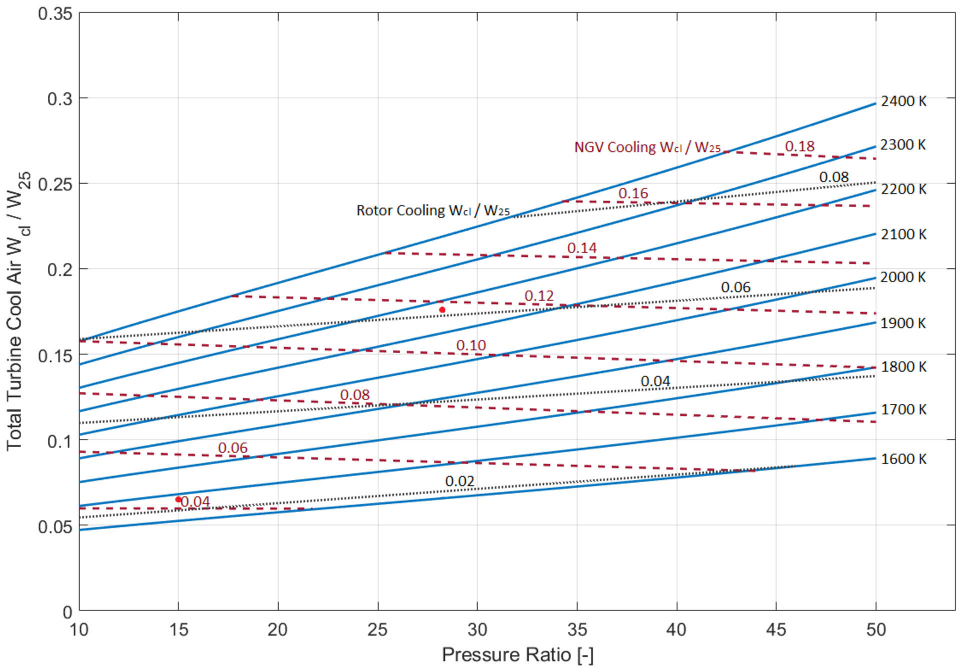

Figure 3.5: Total turbine cooling air required as function of pressure ratio and TIT for a metal temperature of 1200 K.

The pressure ratios where estimated first. This estimation was based on the OPR from literature, which is 28, and analysis by synthesis by varying the pressure ratios for the fan core and duct side, see figure 3.6. An inlet pressure ratio of 0.9 was found appropriate. The duct and core of the fan are modelled separately to account for the varying gas characteristics over the flow cross area between fan hub and tip, resulting in different compression processes for core and duct side of the fan. [23] The pressure ratios of the core of the engine respectively to the duct of the engine should be chosen carefully, as to prevent a pressure conflict further downstream in the engine, when the two flows are mixed again. A closest match with the provided OPR from literature without pressure conflicts in the mixer is shown in table 3.3. This results in a OPR of 28.2 for the simulation model, which is a 0.71% difference to the OPR as found from literature.

Table 3.3: Pressure ratios for fan core and duct and compressor.

Component	Pressure Ratio
Inlet	0.9
Fan core	4.7
Fan duct	5.1
Compressor	6
OPR	28.2

After a match for the pressure ratios is found, the next parameters to iterate for are the inlet mass flow, the turbine inlet temperature and the mixer area. The turbine inlet temperature instead of the fuel mass flow is chosen as parameter, since this will lead to more stable calculations in GSP. Using analysis by synthesis an iteration is performed for the inlet mass flow, turbine inlet temperature and mixer area for the ranges as shown in figure 3.7. The range for the inlet mass flow and turbine inlet temperatures are based on the estimations as explained in subsection 3.2.2. The mixer area is adapted to a range where no errors are found for the mixer pressure exceeding the duct pressure.

Furthermore, the bleed ratios and cooling ratios are matched to the preferred performance. From figure 3.5 it was found that approximately 18% of the core mass flow is required for HPT cooling, of which 67% for NGV cooling and 33% for rotor cooling, and 6% of the core mass flow for LPT cooling, of which also 67% for NGV cooling and 33% for rotor cooling. For the HPT cooling it is assumed that the bleed is tapped at the end

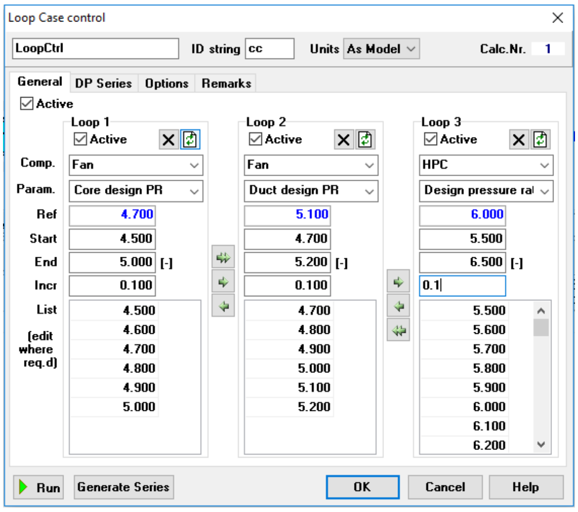

LoopCtrl
ID string cc
Units As Model
Calc.Nr. 1
☑ Active

	Loop 1	Loop 2	Loop 3
	☑ Active	☑ Active	☑ Active
Comp.	Fan	Fan	HPC
Param.	Core design PR	Duct design PR	Design pressure ral
Ref	4.700	5.100	6.000
Start	4.500	4.700	5.500
End	5.000 [-]	5.200 [-]	6.500 [-]
Incr	0.100	0.100	0.1
List (edit where req.d)	4.500 4.600 4.700 4.800 4.900 5.000	4.700 4.800 4.900 5.000 5.100 5.200	5.500 5.600 5.700 5.800 5.900 6.000 6.100 6.200

Figure 3.6: Loop case control input window for fan and compressor pressure ratio.

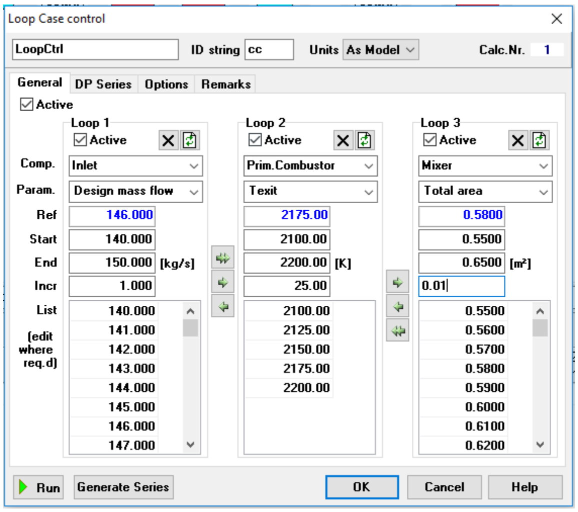

LoopCtrl
ID string cc
Units As Model
Calc.Nr. 1
☑ Active

	Loop 1	Loop 2	Loop 3
	☑ Active	☑ Active	☑ Active
Comp.	Inlet	Prim.Combustor	Mixer
Param.	Design mass flow	Texit	Total area
Ref	146.000	2175.00	0.5800
Start	140.000	2100.00	0.5500
End	150.000 [kg/s]	2200.00 [K]	0.6500 [m²]
Incr	1.000	25.00	0.01
List (edit where req.d)	140.000 141.000 142.000 143.000 144.000 145.000 146.000 147.000	2100.00 2125.00 2150.00 2175.00 2200.00	0.5500 0.5600 0.5700 0.5800 0.5900 0.6000 0.6100 0.6200

Figure 3.7: Loop case control input window for mass flow, temperature and area.

of the compressor. For the LPT it is assumed that the bleed is tapped in the middle of the compressor. This was set as initial input for the synthesis by analysis. After further iterations for the pressure ratios, inlet mass flow, turbine inlet temperature and mixer area, the cooling ratios were fine-tuned to the values as provided in table 3.4.

Table 3.4: Bleed flow and cooling ratios.

HPT	
Bleed 3	18% of W_{25}
NGV Cooling	67% of Bleed 3
Rotor Cooling	33% of Bleed 3
LPT	
Bleed 4	7% of W_{25}
NGV Cooling	64% of Bleed 4
Rotor Cooling	36% of Bleed 4

Also the efficiencies are matched. From literature it is found that for a state-of-the-art engine the compressor efficiency is approximately 85%, the HPT efficiency is approximately 89 – 91% and the LPT efficiency is approximately 87 – 89%. Taken into account that the turbine blades have been optimized for cooling, these efficiencies can even be higher. Furthermore, a fan efficiency of 90%, a combustion efficiency of 99.5% and a mechanical efficiency of 99.5% are found appropriate. [24] From literature it is found that the HPT shaft rotates at speeds exceeding $15000 RPM$ and the fan shaft rotates at speeds exceeding $10000 RPM$. [5] Lastly, the thrust can be scaled with the nozzle velocity coefficient C_V. This let to the design parameters as provided in table 3.5.

The most interesting differences compared to the F100-PW-220 engine which powers the F-16 are the increase in inlet mass flow, fuel flow and turbine inlet temperature. The inlet mass flow has been increased with 44%, the mass flow has been increased with 142% and the turbine inlet temperature has approximately been increased with 18%.

3.3. Validation

Since little is actually known about the engine, the validity of the model plays an important role. In this section the validity of the designed engine model will be discussed for the design point simulation, afterburner mode and for off-design simulation.

Table 3.5: Design parameters.

Parameter	Symbol	Value	Unit
Inlet mass flow	W	147	$\frac{kg}{s}$
Pressure ratio inlet	PR_i	0.9	$[-]$
Pressure ratio fan (core)	PR_{c_f}	4.7	$[-]$
Pressure ratio fan (duct)	PR_{d_f}	5.1	$[-]$
Fan efficiency	η_f	0.9	$[-]$
Shaft 1 rotational speed	N_1	10080	RPM
Bypass ratio	BPR	0.57	$[-]$
Engine core mass flow	W_{25}	93.63	$\frac{kg}{s}$
Pressure ratio compressor	PR_c	6	$[-]$
Compressor efficiency	η_c	0.85	$[-]$
Shaft 2 rotational speed	N_2	15200	$[-]$
Fuel flow	W_F	3.15	$\frac{kg}{s}$
Combustor efficiency	η_{comb}	0.995	$[-]$
Turbine inlet temperature	TIT	2175	K
Turbine efficiency (HPT)	$\eta_{turb,HPT}$	0.9	$[-]$
Turbine efficiency (LPT)	$\eta_{turb,LPT}$	0.91	$[-]$
Mechanical efficiency	η_{mech}	0.995	$[-]$
Mixer area	A_6	0.54	$[-]$
Thrust	FN	125903	N
Overall pressure ratio	OPR	28.2	$[-]$
Nozzle velocity coefficient	C_V	0.985	$[-]$
Thrust specific fuel consumption	$TSFC$	0.090	$\frac{kg}{Nh}$

3.3.1. DESIGN POINT SIMULATION

Using the methodology as described in the previous section, an engine simulation model is reverse engineered for the F135-PW-100 engine. The design point is taken as the maximum thrust without afterburner at sea level static (SLS) conditions. This led to the design point performance parameters as provided in table 3.6, including the intended value, as found from literature or theory and the accuracy to this value.

As can be seen in table 3.6 a maximum difference of 1.1% is found for the thrust. Based on the little information known, the design point is found valid for this research.

Table 3.6: Design point performance parameters.

Parameter	Value	Goal	Difference
BPR	0.57	0.57	0.0%
OPR	28.2	28	0.71%
FN	124550	125903	1.1%

3.3.2. AFTERBURNER MODE

From the literature study the thrust in afterburner (AB) mode is found to be $191.3kN$. The performance for maximum thrust in AB mode can be validated under the assumption that the engine core performance remains the same. This assumption can be processed in the GSP model by defining the engine pressure ratio (EPR) as the overall pressure ratio between inlet and LPT. The EPR has to be constant during AB mode. In order for the error equations and state variables to be solved, the nozzle area ratio is set as free state. The AB exit temperature can be used to scale the thrust in AB mode. The best result is found for an AB exit temperature, T_{T8}, of $2300K$. At this temperature all added fuel is burnt. Note that a high temperature in the afterburner is less significant as a high temperature in the turbine, as there are no rotating parts. The AB performance characteristics are provided in table 3.7. The AB thrust value and accuracy are shown and a comparison is made for the fuel flow and nozzle exit area for AB mode and dry mode.

As can be seen in table 3.7, the AB thrust is matched to an accuracy of 1.1%. Based on the little data known, this match is found to be valid for this research.

Table 3.7: AB mode performance parameters.

Parameter	**Value**	**Goal**	**Difference**
FN_{AB}	189211	191274	1.1%
Parameter	**AB mode**	**dry mode**	**ratio**
W_F A_8	$6.69\frac{kg}{s}$ $0.52m^2$	$3.15\frac{kg}{s}$ $0.32m^2$	2.12 1.62

3.3.3. OFF-DESIGN SIMULATION

Although the model can not truly be validated for off-design performance, since no actual recorded flight data is known for this part, the behaviour and stability of the off-design simulation can be analysed. For the off-design simulation the validation is divided into steady-state series behaviour and transient behaviour. A range for TIT from $2175K$ to $1200K$ is used as input.

In figures 3.8 up until 3.11 the results for the steady-state series analysis are provided. With the steady-state analysis the relation between engine performance and a specific parameter can be analysed, in this case the TIT. In figure 3.8 the thrust F_N, inlet mass flow W, fuel flow W_F and HPT shaft rotational speed N_2 are provided as a function of the turbine inlet temperature TIT. As expected, all parameters increase with increasing TIT.

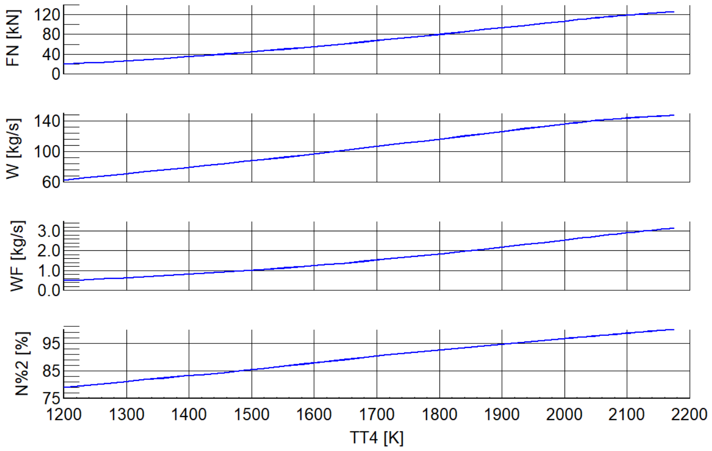

Figure 3.8: Off-design steady state series analysis.

In figure 3.9 the compressor map is provided for the steady-state series with TIT varying from $2175-1200K$ and vice-versa. In this figure the design point is indicated with a black square. It can be seen that for decreasing TIT the point in the compressor map decreases nearly linearly. This means that the engine performs more efficiently towards idle input with respect to the design point, which is as expected. The near linear decrease indicates the compressor has a stable performance.

In figures 3.10 and 3.11 the performance maps for the fan core and duct are shown, respectively. Also for these components a near linear decrease is found with decreasing TIT, meaning the components have a stable performance.

For future operability of the gas turbine simulation model transient simulations based on recorded flight data are preferred. In this manner the actual operations performed with the engine can be coupled to the lifing model. For this research no recorded flight data is available of the F-35, however as an illustration of the functionality and stability of the gas turbine simulation model, a transient analysis is performed. For this purpose, the TIT is changed over time as shown in table 3.8. As can be seen in table 3.8 the TIT is decreased from take-off to idle mode and back to take-off in a stepwise manner, for which idle-mode is set at $1200K$. A gradual change is imposed from $2175-2000K$ and vice-versa and a steep change is imposed from $2000-1200K$ and vice-versa.

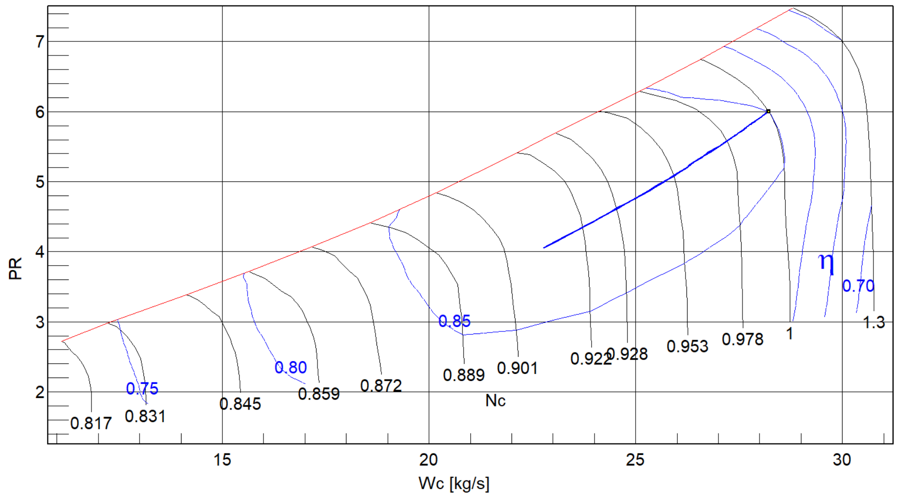

Figure 3.9: Off-design steady state series compressor map.

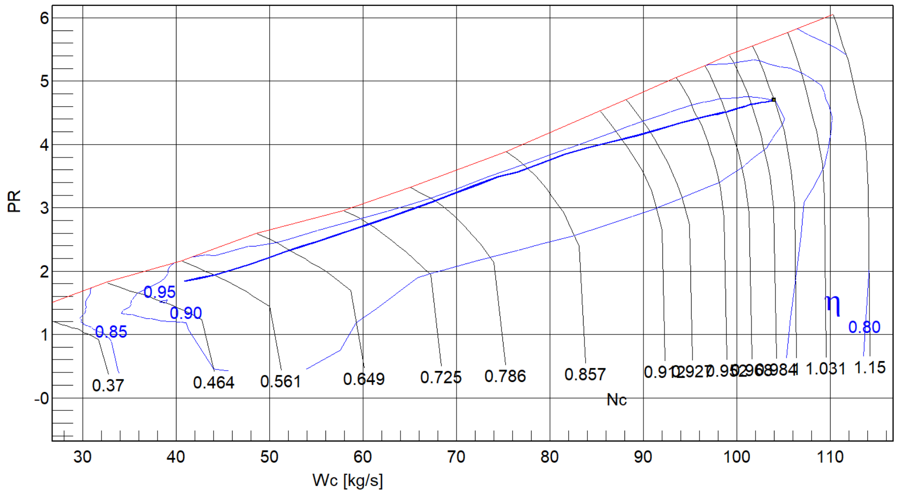

Figure 3.10: Off-design steady state series fan map (core).

Table 3.8: Transient input for turbine inlet temperature over time.

Time $[s]$	TIT $[K]$
$0-5$	2175
$5-10$	$2175-2000$
$10-15$	2000
$15-20$	$2000-1200$
$20-25$	1200
$25-30$	$1200-2000$
$30-35$	2000
$35-40$	$2000-2175$
$40-45$	2175

In figures 3.12 up until 3.15 the results for the transient analysis are provided. With the transient analysis the engine performance to input change over time can be analysed for TIT. In figure 3.12 the thrust F_N, inlet mass flow W, fuel flow W_F and HPT shaft rotational speed N_2 are provided as a function of the turbine inlet temperature TIT. As can be seen the engine model behaves stable over the input change.

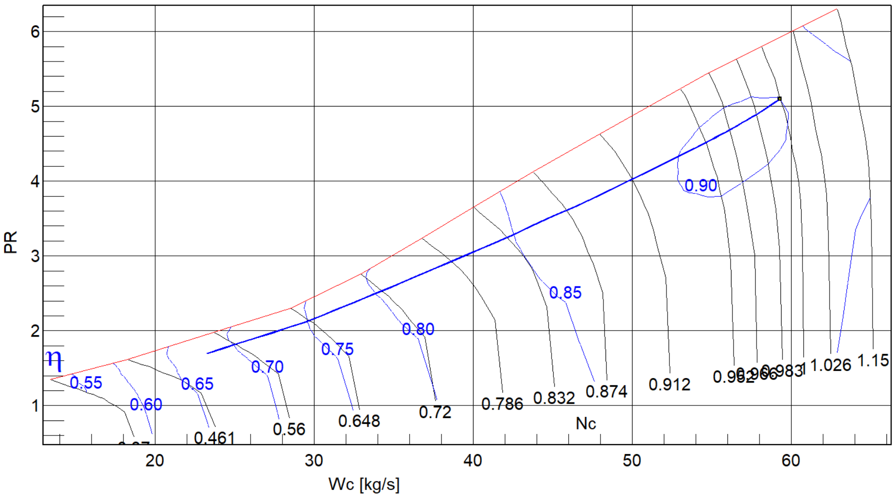

Figure 3.11: Off-design steady state series fan map (duct).

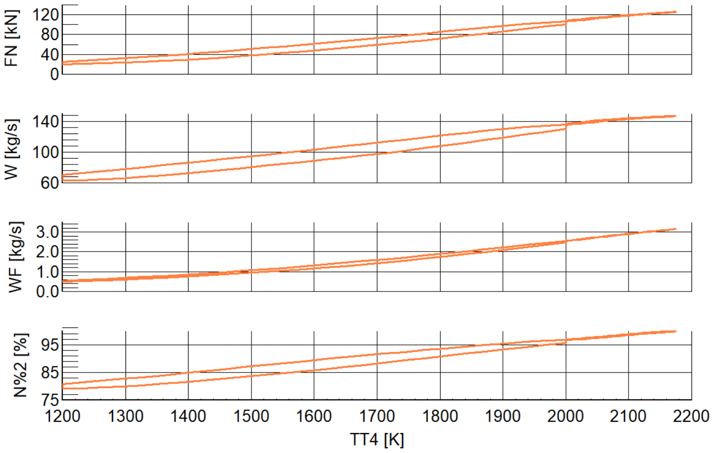

Figure 3.12: Transient analysis.

In figure 3.13 the compressor map is provided for the transient analysis with varying TIT from 2175 – 1200K and vice-versa. The design point is indicated with the black square. The orange line indicates the operating line of the compressor for the varying TIT. It can be seen that the corrected rotational speed decreases with increasing TIT and the compressor efficiency increases as the temperature input progresses towards idle input. The surge limit of the compressor is not exceeded. From this it can be concluded that the compressor shows a stable performance both for the gradual change in TIT as for a steep change in TIT.

In figures 3.14 and 3.15 the performance maps for the fan core and duct are provided, respectively. Also these components show a stable behaviour of the operating line and the surge limit is not exceeded, both for a gradual change and for a steep change in TIT.

3.4. DISCUSSION ON ENGINE MODELLING.

Because of the little data known and the lack of validation therefore possible, a critical reflection on the performed engine modelling is required. Although a reasonable engine model has been designed close to the performance parameters that are known, this does not mean that this is the only valid combination of design parameters leading to valid performance. For this research it is chosen to use the set of design parameters as provided in tables 3.5 and 3.4, based on the theory and assumptions as discussed above. The assumptions made in this part of the research will affect the results of the overall research. These are the pitfalls of this research. Therefore a critical reflection on these assumptions is provided in this section. The following assumptions have been made.

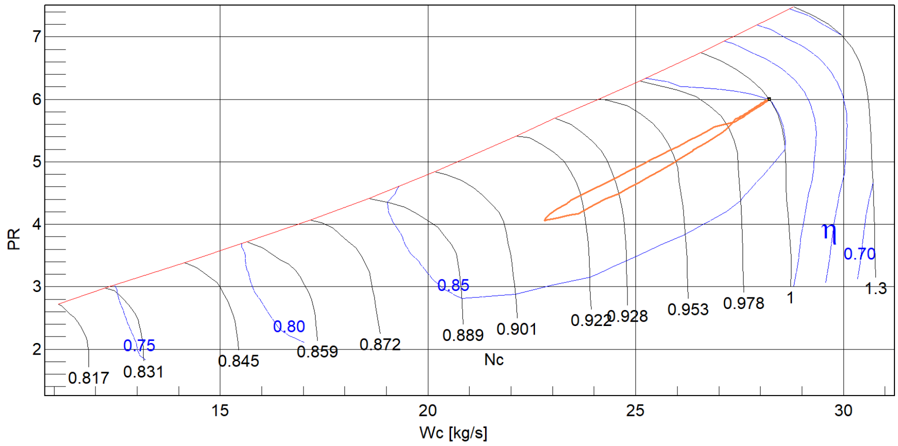

Figure 3.13: Transient analysis compressor map.

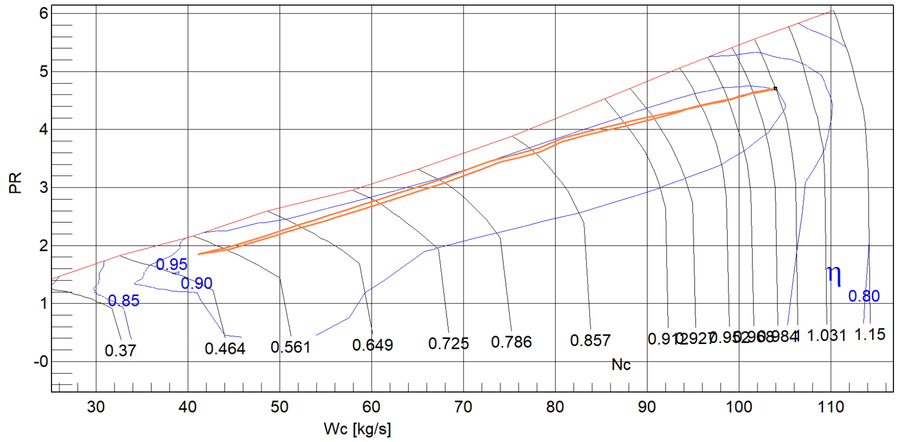

Figure 3.14: Transient analysis fan map (core).

- Performance data as provided in subsection 3.2.1 is assumed to be valid.
- A range for the inlet mass flow of $145-157\frac{kg}{s}$ is assumed.
- A range for the turbine inlet temperature of approximately $2000-2300K$ is assumed.
- A maximum metal temperature of $1200K$ is assumed.

3.4.1. DISCUSSION ON ASSUMPTIONS

The performance parameters as provided by the OEM and by Jane's are used for this research. Since this data is used to model the engine design point this assumption is significant for the performed research. A variation in the performance data will effect the results of the whole research. For a true validation engine test data is recommended.

The assumptions for the inlet mass flow and turbine inlet temperature are also regarded as critical assumptions, as these will effect the design point modelled for the engine and with this the results of the research under consideration. To mitigate these assumptions it is recommended to gather engine test data.

Lastly, the assumption on maximum metal temperature is again regarded as a critical assumption. Variation to this value will affect the cooling air required, the design point modelled and subsequently the results of the research under consideration. Mitigation of this assumption can be achieved when the material properties of the Nickel-alloy used for the turbine blades are known. On a further note, this assumption now leads to an approximation of the required cooling flow of 24% of the core mass flow. After iterations in the analysis by synthesis this is even increased to 25%. This is a significant amount of mass flow and although it validated by the theory from Kurzke and the analysis by synthesis, it is expected that this approximation is too high.

For a further implementation of the lifing model it is advised to gather flight performance data from the engine under consideration itself. In this manner transient analyses can be simulated.

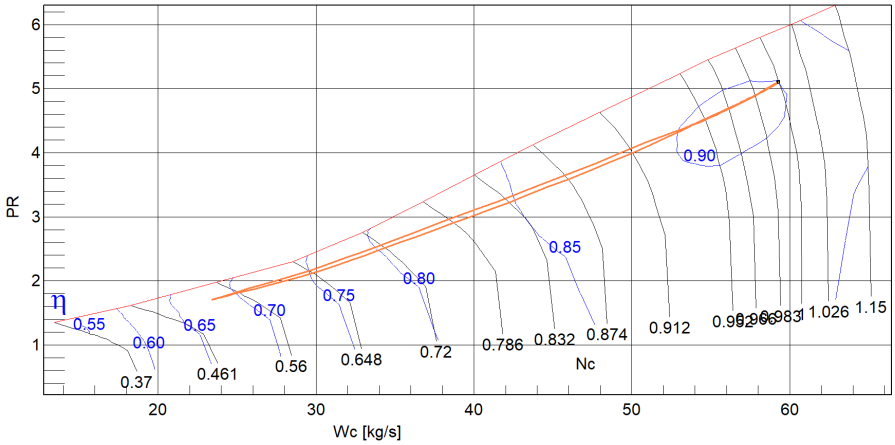

Figure 3.15: Transient analysis fan map (duct).

3.4.2. SENSITIVITY ANALYSIS

Next to the assumptions, also the choice of parameter value as determined through the analysis by synthesis can be discussed. Analysis by synthesis is an effective method to find a design point, but it is critical on validation. Therefore the sensitivity of the engine thrust to a 1% change to each of the design parameters as provided in table 3.5 is determined and the results are given in table 3.9. Parameters that do not affect the thrust are left out of the sensitivity analysis.

Table 3.9: Sensitivity of thrust when changing parameters by 1 percent

Parameter	**Effect on thrust**
Inlet mass flow	1.04%
Pressure ratio inlet	0.24%
Pressure ratio fan (core)	0.03%
Pressure ratio fan (duct)	0.13%
Fan efficiency	0.17%
Bypass ratio	0.18%
Pressure ratio compressor	0.03%
Compressor efficiency	0.18%
Combustor efficiency	0.07%
Turbine inlet temperature	0.91%
Turbine efficiency (HPT)	0.08%
Turbine efficiency (LPT)	0.07%
Mechanical efficiency	0.34%
Mixer area	0.02%
Nozzle velocity coefficient	0.35%

In table 3.9 it can be seen that the inlet mass flow and turbine inlet temperature have a significant influence on the engine thrust. This makes sense and highlights the importance of validation of these parameters. The other parameters have a relatively low effect on the thrust. Note that the rotational velocity is not of influence for this sensitivity analysis regarding engine modelling. However, for the lifing analysis the rotational velocity will be of significant importance. The effect of this parameter will be discussed later in this report.

3.4.3. GSP ACCURACY

A last consideration for the engine modelling is the accuracy of the simulations performed in GSP. This accuracy is dependent on the iteration settings for the convergence of the error variables. The inaccuracy of the GSP model is considered to be less than 2%.

3.5. CASE STUDIES

Four of the research questions consider the effect of the variation of a parameter on the component life of the first stage turbine rotor blade of the F135 engine. The questions considering the amount of cooling air used and the load case can be set up in GSP. The following variations are considered.

- Load case:
    1. Take-off
    2. Idle
- Amount of cooling air:
    1. 25% of core mass flow
    2. 20% of core mass flow

For the load cases, take-off is considered at a TIT of $2175K$, so at the design point. Idle load is considered at a TIT of $1200K$. As shown in the off-design analysis, the engine still has a stable performance at this temperature. However, at lower temperatures this stability degrades. Next to the temperature also the rotational speed of the HPT shaft will be lower for idle-mode with respect to take-off. This will effect the centrifugal load on the rotor blades and is therefore an interesting parameter to consider for the lifing analysis.

Combinations of the above variations leads to four case studies. The results from GSP for these case studies will subsequently be used for the thermal and mechanical analysis. The results from GSP for these four case studies can be found in Appendix B.

4

Heat Transfer Analysis

This chapter will elaborated on the heat transfer analysis of the first stage turbine rotor blade. No data is available regarding the geometry of the blade, therefore a blade will be designed using free-vortex theory that can be used for this research. The methodology will be provided for the external and internal heat transfer distributions and also for the film cooling calculations. Results for seven case studies will be provided. The chapter closes with a critical reflection.

4.1. Heat Transfer Basics

The heat transfer in the first stage turbine rotor blade of the F135 is a complex system with internal and external heat flow. The heat transfer for a turbine rotor blade in a cooled gas turbine depends on the following and is graphically shown in figure 4.1. [25].

- The heat flux from the gas flow to the surface of the component. This is formulated in equation 4.1, where h_{ce} is the external convective heat transfer coefficient, T_g is the hot gas temperature and T_{se} is the temperature of the external surface.
- The radiated heat flux, as formulation in equation 4.2, where ϵ is the emissivity of the surface and σ is the Stefan-Boltzmann constant.
- The heat flux to the cooling channel flow from the cooling channel surface of the component. This is formulated in equation 4.4, where h_{ci} is the internal convective heat transfer coefficient, T_{si} is the temperature of the internal surface and T_c is the coolant temperature.
- The heat flux in the structure of the gas turbine component, as formulated in equation 4.3, where k is the thermal conductivity of the material and L is the characteristic length of the material.

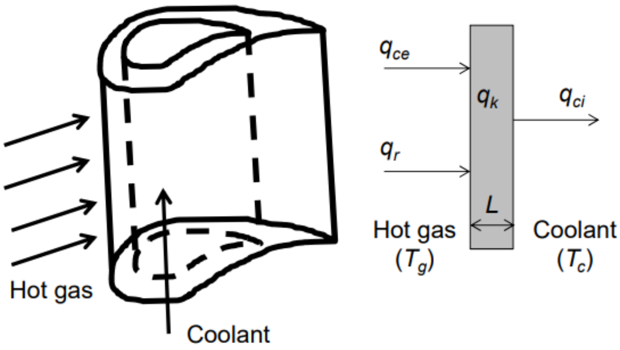

Figure 4.1: Schematic of simplified blade heat transfer system. [25].

$$q''_{ce} = h_{ce}(T_g - T_{se}) \tag{4.1}$$

$$q''_r = \epsilon\sigma(T_{se}^4 - T_g^4) \tag{4.2}$$

$$q_k^{"} = \frac{k}{L}(T_{se} - T_{si}) \tag{4.3}$$

$$q_{ci}^{"} = h_{ci}(T_{si} - T_c) \tag{4.4}$$

For this research the blade wall temperatures will be determined using the finite-elements program Abaqus CAE. For this purpose, the external and internal temperatures and heat transfer coefficients are required as input. The methodology to derive the external and internal temperatures and heat transfer coefficients will be elaborated in the following sections.

4.2. BLADE DESIGN

For this research no geometry of the F135 turbine blade will be available, therefore a blade will be designed. The design of this blade will follow the free-vortex design and the following assumptions.

- Free-vortex flow distribution
- Constant axial velocity
- Constant mean diameter
- Degree of reaction (R_D) of 0.4 is assumed
- No losses are considered.
- Take-off is considered as the design point.

A free-vortex flow distribution means that the velocity triangles vary from root to tip to take into account for the varying rotational speed U from root to tip. For constant stagnation enthalpy across the annulus and constant axial velocity, the whirl component of velocity C_θ is inversely proportional to the radius, as shown in equation 4.5, and radial equilibrium is satisfied. [26]

$$C_\theta r = constant \tag{4.5}$$

The inlet diameter is known, so based on figure 2.2, an estimate of the hub and tip radius of the first stage turbine could be measured and scaled. This resulted in a hub radius of $0.208m$ and a tip radius of $0.266m$, so the mean diameter of the HPT inlet is $0.237m$. With this an estimate could be made of the inlet area, which resulted to be $0.086m^2$. The chord length of the blade is estimated to be $40mm$. From GSP the turbine inlet mass flow and total density are known for the design point. Using the continuity equation as shown in equation 4.6, the inlet velocity can be determined. However, because the static density is unknown, an initial assumption is made for the value of the static density. With this initial assumption the inlet velocity is determined using equation 4.6. With this initial velocity the Mach number is determined and subsequently a new static density is calculated using equation 4.7. Here, κ is provided by GSP. This process is iterated until convergence. Furthermore, it is assumed that the turbine inlet velocity is completely axial.

$$\dot{m} = \rho V A \tag{4.6}$$

$$\rho_s = \rho_t \left(1 + \frac{\kappa - 1}{2} M^2\right)^{\frac{-1}{\kappa - 1}} \tag{4.7}$$

In order to define a blade geometry, the velocity triangles need to be defined. As mentioned above, the inlet velocity is assumed to be purely axial, and the axial velocity component is assumed to remain constant through the stage. With the rotational speed of the HPT at design point of $15200RPM$ the rotational velocity vector can be determined for hub, tip and mid-span. The blade relative and absolute velocity angles at mid-span are determined using equations 4.8, 4.9, 4.10 and 4.11. [26]

$$\tan\beta_3 = \frac{1}{2\phi}\left(\frac{1}{2}\lambda + 2R_D\right) \tag{4.8}$$

$$\tan\beta_2 = \frac{1}{2\phi}\left(\frac{1}{2}\lambda - 2R_D\right) \tag{4.9}$$

$$\tan\alpha_3 = \tan\beta_3 - \frac{1}{\phi} \tag{4.10}$$

$$\tan\alpha_2 = \tan\beta_2 + \frac{1}{\phi} \tag{4.11}$$

The flow coefficient ϕ and loading factor λ in equations 4.8 up until 4.11 are determined using equations 4.12 and 4.13, where C_1 is the axial inlet velocity, U is the rotational velocity, W_{HPT}, is the work provided by the HPT as given by GSP, N_{stages} is the number of stages of the HPT, which is 1 and $\dot{m}_4$ is the turbine inlet mass flow as given by GSP. [27]

$$\phi = \frac{C_1}{U} \tag{4.12}$$

$$\lambda = \frac{2W_{HPT}}{N_{stages}\dot{m}_4 U^2} \tag{4.13}$$

With the absolute and relative velocity angles and the axial velocity for mid-span location, the tangential velocity components at mid-span can be derived. With equation 4.5, the tangential velocity components at hub and tip location can be determined and subsequently the absolute and relative velocity angles for the tip and hub location can be derived. This led to the velocity angles and absolute and relative velocities as provided in table 4.1. The velocity vectors for the hub, mid-span and tip location are shown in figures 4.2, 4.3 and 4.4 respectively.

Table 4.1: Absolute and relative velocity angles and velocities at hub, mid-span and tip location.

	Hub	**Mid-Span**	**Tip**
α_2	69.1°	66.5°	64.0°
β_2	48.7°	31.4°	8.6°
α_3	19.4°	15.1°	12.1°
β_3	60.9°	63.0°	65.0°
C_2	626	559	508
C_3	236	231	228
W_2	338	261	225
W_3	458	491	527

An extra check was performed for the tip Mach numbers, which should not be to high to avoid shock-waves, separation and pressure losses. For the relative tip Mach number a value of 1.03 was found for a $RTDF$ of 15% and a value of 0.988 was found for a $RTDF$ of 10%, meaning that the tip Mach numbers are in a critical range.

A 2D sketch of the blade is designed by implementing the derived velocity angles into a program named OptiBlade. OptiBlade uses a curve fitting algorithm for which the blade velocity inlet and outlet angles are used to interpolate the 2D blade profile, see figure 4.5. [28] Three sketches are made for the hub, mid-span and tip location, respectively. These 2D sketches are subsequently imported into Abaqus CAE, where a 3D blade contour is made by lofting the three 2D sketches to each other. This resulted in the 3D blade as shown in figure 4.6.

4.3. EXTERNAL TEMPERATURE DISTRIBUTION

As stated in chapter 1, one of the research sub-questions is about the effect of improvement in the combustor pattern factor. In chapter 2 it was stated that P & W claims that the combustor pattern factor has been improved with 30%. To asses this effect two combustor pattern factors, or radial temperature distribution factors (RTDF), are used for the analysis. The RTDF values of 15% and 10% are used to determine the maximum radial temperature, as shown in equations 4.14. Here T_{mean} equals T_{t4} and $\Delta T_{combustor}$ equals $T_{t4} - T_{t3}$. Note that only the radial temperature distribution is considered here, thus the overall, circumferential temperature distribution is not considered. [29] [30]

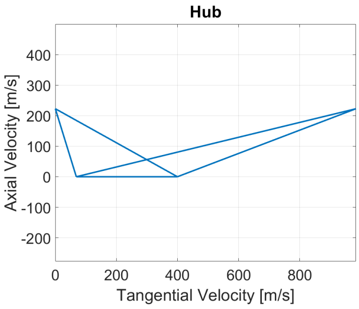

Figure 4.2: Velocity vectors at hub

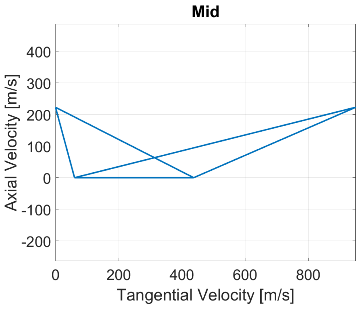

Figure 4.3: Velocity vectors at mid-span

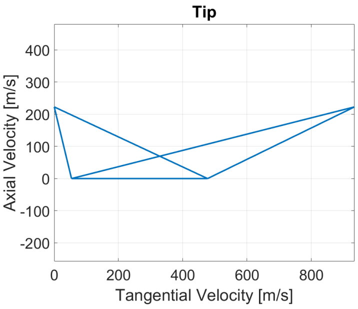

Figure 4.4: Velocity vectors at tip

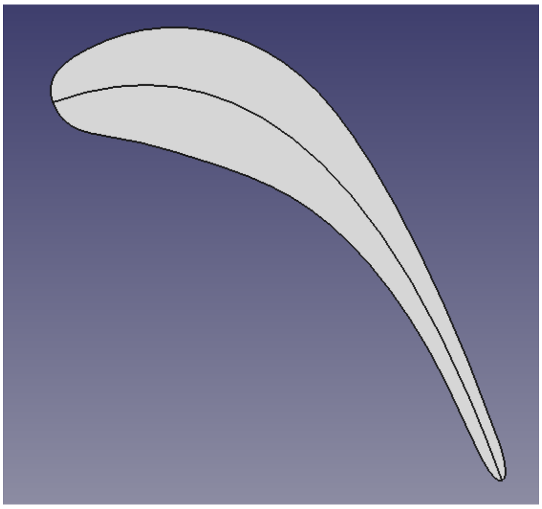

Figure 4.5: 2D blade configuration as provided by OptiBlade.

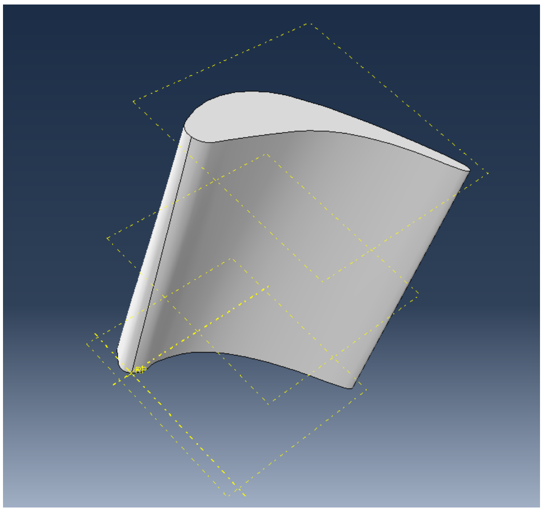

Figure 4.6: 3D blade configuration as provided by Abaqus.

$$RTDF = \frac{T_{max} - T_{mean}}{\Delta T_{combustor}} \tag{4.14}$$

From literature it is known that the temperature profile follows a somewhat parabolic profile and has the objective to provide a lower temperature at the root, where mechanical stress is highest, and at the tip, which is most difficult to cool. [30] [29] For this purpose a symmetrical parabolic profile is assumed. In order to acquire a symmetrical, parabolic radial temperature distribution for the F135, the quadratic equation as shown in equation 4.15 will have to be solved using the calculated T_{max} and T_{t4} as determined by GSP. This leads to the constants a, b and c, as shown in equations 4.16, 4.17 and 4.18. For the radial distances of these temperatures only the tip radius for minimum temperature and mid-span for maximum temperature are known. Therefore iteration is required to solve for the location of the mean temperature radial position. Converting the radial temperature for the NGV to the rotor is done by multiplying with $\frac{T_{t_{41}}}{T_{t_4}}$.

$$T(r) = ar^2 + br + c \tag{4.15}$$

$$a = -4(T_{max} - T_{min}) \tag{4.16}$$

$$b = 4(T_{max} - T_{min}) \tag{4.17}$$

$$c = T_{min} \tag{4.18}$$

In the static frame of reference for a NGV the total absolute temperature remains constant along the blade, however in the static frame of reference of the rotor blade, the total relative temperature remains constant along the blade. This means that the total temperature at the rotor inlet has to be converted to total relative temperature. For this the mollier diagram as shown in figure 4.7 is used. From this figure the total relative temperature is derived as provided in equation 4.19. This results in the radial total relative temperature distributions for various $RTDF$ as shown in figure 4.8.

$$T_{t,rel_{41}} = T_{t_{41}} - \frac{C_2^2}{2C_P} + \frac{W_2^2}{2C_P} \tag{4.19}$$

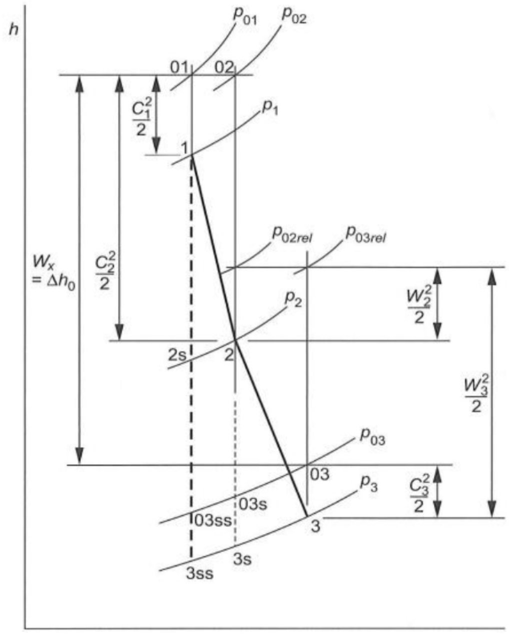

Figure 4.7: Mollier enthalpy-entropy diagram. [31]

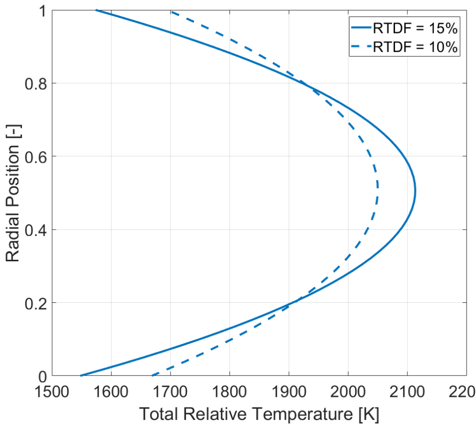

Figure 4.8: Radial total relative temperature distribution for variant RTDF.

4.4. EXTERNAL HEAT TRANSFER COEFFICIENT

On the exterior of the blade, heat transfer in the form of convection and radiation occurs from the hot gas to the blade surface. Several correlations exist for the convection type of heat transfer, mostly considering the leading edge of the blade as a cylinder in cross-flow and the other part of the blade as a flat plate. For the heat transfer over a cylinder, the correlation from Mehendale et al. [32] is used, as shown in equation 4.20. For flat plate heat transfer, the correlation from the book Turbine Design and Application [33] is used, as shown in equation 4.21.

$$\frac{Nu}{\sqrt{Re}} = 0.902 + 2.14\left(\frac{Tu\sqrt{Re}}{100}\right) - 2.89\left(\frac{Tu\sqrt{Re}}{100}\right) \tag{4.20}$$

$$Nu_x = 0.0296 Re_x^{0.8} Pr^{0.3} \tag{4.21}$$

For the provided correlations the Reynolds number and the Prandtl number of the fluid and the turbulence intensity are required. These parameters can be approximated for the turbine blade airfoil. The Reynolds number can be determined using equation 4.22, where ρ is the density, V the velocity, c the characteristic length of the component under consideration, so in this case the chord length, and μ is the dynamic viscosity of the gas as provided by GSP. The velocity varies over the blade surface due to its curvature, this will affect the Reynolds number, and subsequently the heat transfer.

$$Re = \frac{\rho V c}{\mu} \tag{4.22}$$

4.4.1. VELOCITY PROFILE

The velocity distribution along the blade surface is determined using the velocity distributions on a conventional turbine blade as shown in figure 4.9. [34] Note that figure 4.9 is valid for the relative velocity. This resulted in the relative velocity distribution over the pressure and suction side of the blade at mid span as shown in figure 4.10. The radial velocity distribution is found by interpolating between the hub, mid-span and tip location values for the relative velocity at each meridional location respectively.

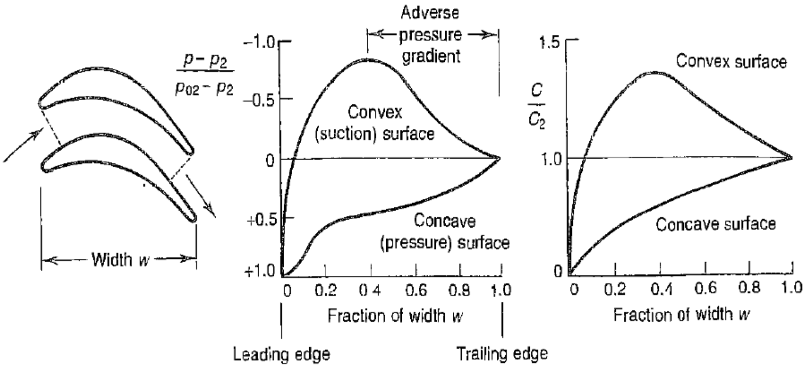
Width w
p − p2
p02 − p2
−1.0
−0.5
0
+0.5
+1.0
Adverse
pressure
gradient
Convex
(suction) surface
Concave
(pressure) surface
0
0.2
0.4
0.6
0.8
1.0
Fraction of width w
Leading edge
Trailing edge
C
C2
1.5
1.0
0
Convex surface
Concave surface
0
0.2
0.4
0.6
0.8
1.0
Fraction of width w

Figure 4.9: Pressure and velocity distributions on a conventional turbine blade. [34]

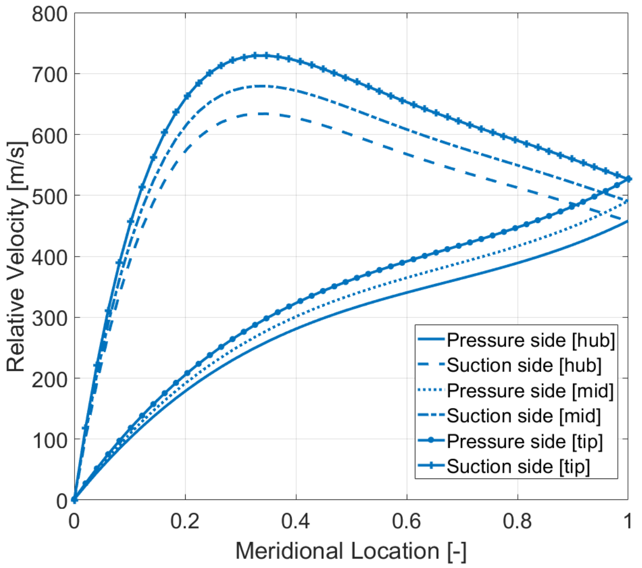

Figure 4.10: Velocity distribution at hub, mid-span and tip locations.

4.4.2. CONVECTION

With the velocity profile as determined through the previous subsection, the convective heat transfer coefficient is determined. The convective heat transfer over the exterior of the blade can be regarded as a cylinder in cross-flow for the leading edge of the blade and as a flat plate for the remaining part of the blade. For the leading edge a diameter of $0.006m$ is approximated, based on figure 4.5. A chordlength of the blade of $0.04m$ is assumed.

For the leading edge heat transfer, the Nusselt number correlation for a cylinder in cross-flow from Mehendale is considered. [32] The Nusselt number is the ratio of convective heat transfer over conductive heat transfer, and related to the heat transfer coefficient as shown in equation 4.23. Here h is the heat transfer coefficient, D is the characteristic length of the component under consideration and k is the conductivity of the fluid. The conductivity of air as a function of the temperature is provided in equation 4.24. [35]

The correlations for leading edge heat transfer provide the heat transfer at the stagnation point. In order to attain a heat transfer distribution over the leading edge region, equation 4.25 is used. The angle ϕ is illustrated in figure 4.11. Equation 4.25 is valid for angles between −80° and 80°.

$$Nu = \frac{hD}{k} \tag{4.23}$$

$$k_{air} = 1.99 \cdot 10^{-3} \frac{T^{1.5}}{T+112} \tag{4.24}$$

$$h = h_{stag}(1-(\frac{\phi}{90})^3) \tag{4.25}$$

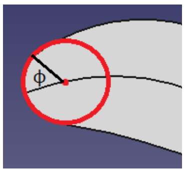

Figure 4.11: Illustration of the angle ϕ.

For the remaining part of the blade the external heat transfer is determined using the flat plate correlations and the velocity distribution as determined in subsection 4.4.1. In order to assure for a smooth transition between the leading edge heat transfer distribution and the remaining part of the blade, the calculated heat transfer coefficients for leading edge and flat plate are interpolated using an 8th degree polynomial. This results in the convective heat transfer coefficient distribution at hub, mid-span and tip location as shown in figure 4.12.

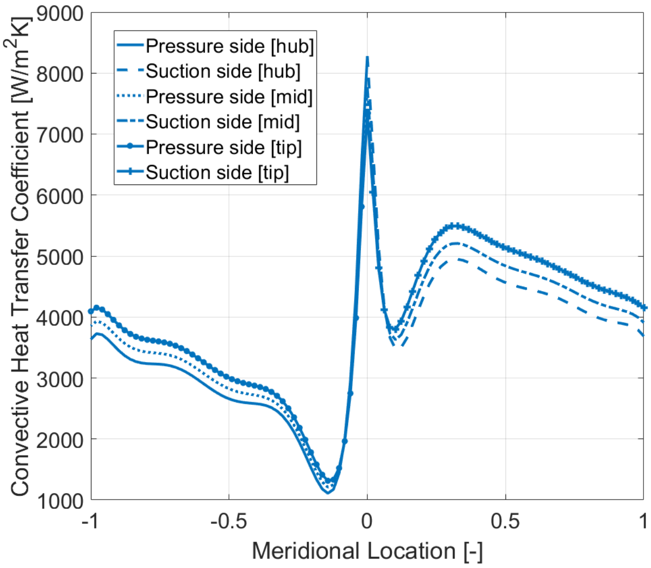

Figure 4.12: Convective heat transfer coefficient distribution at hub, mid-span and tip locations.

4.4.3. RADIATION

The heat transfer coefficient for heat transfer in the form of radiation can be derived from the radiative heat flux for a non-luminous flame, as shown in equation 4.26. Here, σ_c is the Stefan-Boltzmann constant with a value of $5.67 \cdot 10^{-8}[\frac{W}{m^2K}]$, ϵ_w and ϵ_g are the emissivity for wall and gas, respectively, T_g is the gas temperature and T_w is the wall temperature. The gas emissivity ϵ_g can be determined using equation 4.27, where P is the gas pressure in kPa, q is the fuel to air ratio by mass and l_b is the characteristic length. The characteristic length can be found using equation 4.28, where V is the hot gas volume and A is the surface area of the hot gas. [29]

$$q''_{rad} = 0.5\sigma_c(1+\epsilon_w)\epsilon_g T_g^{1.5}(T_g^{2.5} - T_w^{2.5}) \tag{4.26}$$

$$\epsilon_g = 1 - e^{-290P(ql_b)^{0.5}T_g^{-1.5}} \tag{4.27}$$

$$l_b = 3.4\frac{V}{A} \tag{4.28}$$

If it is assumed that the external heat flux from the hot gas to the blade surface is of the form $q'' = h(T_g - T_w)$, than the radiative heat transfer coefficient can be derived as in equation 4.29, where ϵ substitutes $0.5(1+\epsilon_w)\epsilon_g$. Note that the wall temperature is required for the calculation of the radiation heat transfer coefficient, therefore a value of $1200K$ is estimated for the wall temperature. The results for the radiative heat transfer coefficient distribution are provided in figure 4.13.

$$h_r = \epsilon\sigma_c T_g^{1.5}(T_g^{2.5} - T_w^{2.5})\frac{1}{T_g - T_w} \tag{4.29}$$

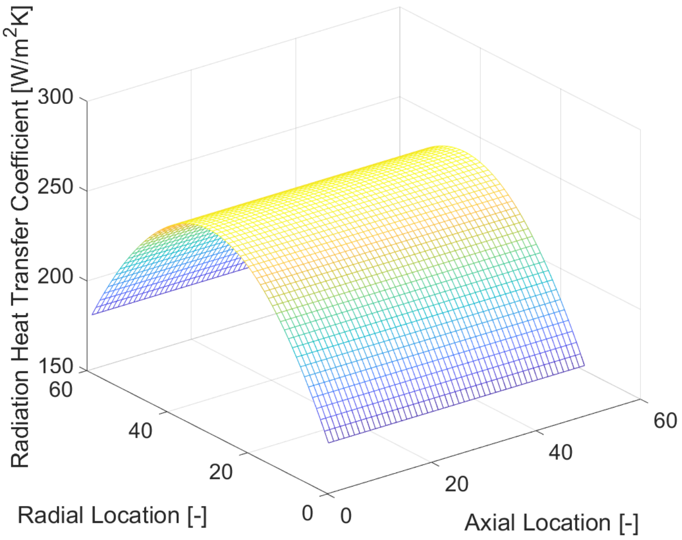

Figure 4.13: Radiative heat transfer coefficient distribution.

4.4.4. HEAT TRANSFER COEFFICIENT COMBINED WITH TBC PROPERTIES

For the analysis the material properties of the superalloy CMSX-4 will be used. This is a second generation Nickel-based superalloy. As was mentioned in section 2.4, a second generation superalloy can be expected for the F135 rotor blades. The material properties for CMSX-4 and for the TBC are provided in appendix C. The effect of the TBC will be incorporated in the heat transfer coefficient as shown in equation 4.30. [36] This results in the heat transfer coefficient distribution for hub, mid-span and tip locations as shown in figure 4.14. [37]

$$h_{tot} = \frac{1}{\frac{1}{h_{conv}+h_{rad}} + \frac{t_{TBC}}{k_{TBC}}} \tag{4.30}$$

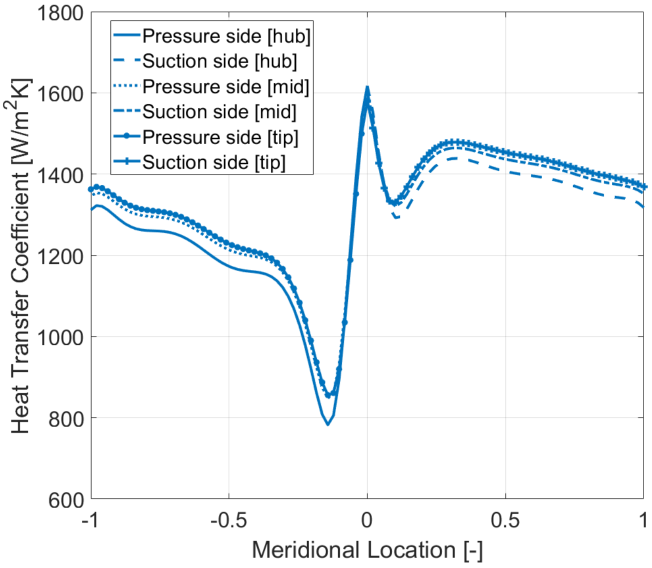

Figure 4.14: Total heat transfer coefficient distribution at hub, mid-span and tip locations.

4.5. INTERNAL HEAT TRANSFER COEFFICIENT

The blade is divided into three segments. The front section at the leading edge is cooled by means of impingement cooling, the middle section is cooled by means of channels with turbulators and the trailing edge section is cooled by means of pin fins, as similarly shown in figure 2.6. The heat transfer coefficients for each of these cooling methods is determined using Nusselt number correlations. The exact internal geometry of the turbine rotor blade is unknown, therefore approximations are made based on figures 2.6, 4.15 and 4.16. The following assumptions and approximations are made.

- The air used for cooling is bleed air from the compressor. It is assumed that the bleed air is tapped at the end of the compressor, so the gas properties of the compressor exit can be used for the cooling air analysis.
- The inlet diameter of each section can be determined from 2.6.
- The number of blades is determined by approximating the available circumferential blade space. Based on figure 2.2, the blade spacing p_{blades} is approximated to be $0.002m$. Using equation 4.31 the number of blades is found to be approximately 60.
- The cooling air per blade is equally divided over the impingement, turbulator and pin fin section. The total HPT cooling air is $5.6\frac{kg}{s}$, so per blade this is found to be $0.09\frac{kg}{s}$ and per section $0.03\frac{kg}{s}$.
- The internal heat transfer coefficient is assumed to remain constant throughout the cooling channels.

$$N_{blades} = \frac{2\pi r_{hub}}{p_{blades}} \tag{4.31}$$

4.5.1. JET IMPINGEMENT COOLING

The impingement channel inlet diameter is approximated be means of figure 2.6 and found to be $0.004m$. Since the mass flow is also known, the velocity of the flow entering the impingement channels can be determined using the continuity equation, as provided in equation 4.6. The only unknown is the static density. In order to determine the static density an iteration is performed for which an initial assumption of the static density is used as input. In this manner, an initial velocity is determined with which an initial Mach number can be determined. Subsequently, the actual static density is determined using equation 4.7. This process is iterated until convergence.

In order to determine the heat transfer coefficient for impingement cooling the Reynolds number of the impingement jet is required. This can be determined with the effective velocity and effective area of impingement holes. For this purpose the patented turbine blade with multi-pass cooling as shown in figure 4.15 is used as example to determine the jet impingement hole diameter. [38] In the example of figure 4.15 there are 21 impingement holes and an approximate diameter of $0.0006m$ is found. The effective velocity per impingement hole is found by dividing the impingement cooling air over approximately 21 impingement holes and using the continuity equation 4.6 the impingement channel area can be related to the impingement hole area. Using the effective velocity and effective diameter, the Reynolds number per impingement hole can be determined using equation 4.22. This leads to a Reynolds number of 299950. Next to the Reynolds number, also the Prandtl number is required for the correlations. The Prandtl number for the compressor exit temperature is used of 0.69.

The correlation from Huber and Viskanta [39] in equation 4.32 was found to be the best to implement without knowing much about the exact geometry. For $\frac{H}{D}$ and $\frac{X_n}{D}$ values of 0.25 and 8 can be assumed, respectively. This leads to heat transfer coefficients for the impingement area of approximately $9963 \frac{W}{m^2K}$.

$$Nu = 0.285 Re_D^{0.710} Pr^{0.33} (\frac{H}{D})^{-0.123} (\frac{X_n}{D})^{-0.725} \tag{4.32}$$

4.5.2. CHANNELS WITH TURBULATORS

The channel with turbulators inlet diameter is approximated be means of figure 2.6 and found to be $0.007m$. For the channels with turbulators it is assumed that there are two turns in the channel, similar as to figure 2.6. The same methodology is used for the channels with turbulators to determine the channel velocity as explained above for the impingement section. The continuity equation is used with an iteration for the static density.

In order to determine the heat transfer coefficient for the channels with turbulators, the Reynolds number and Prandtl number are required. The Reynolds number is determined with equation 4.22 using the channel velocity and diameter and found to be 165200. The Prandtl number for the compressor exit temperature is used of 0.69.

The correlations from Dittus-Boelter, as shown in equation 4.33 was found to be most suitable to use. [40] The Dittus-Boelter correlation provides the heat transfer for a smooth duct, so an additional factor needs to be added to account for the effect of turbulator ribs within the internal cooling channels. Based on literature a factor of 3.5 was found to be suitable to convert the smooth duct heat transfer to the heat transfer within a turbulated channel. [41] This leads to heat transfer coefficients for the internal cooling channels of approximately $7928 \frac{W}{m^2K}$.

$$Nu = 0.023 Re^{0.8} Pr^{0.3} \tag{4.33}$$

4.5.3. PIN FIN COOLING

In order to determine the heat transfer coefficient for pin fin cooling, again the Reynolds number and Prandtl number are required. The diameter for the pin fin section is approximated to be $0.008m$. The velocity through the pin fin cooling channel is determined in the same manner as for the impingement section and channel with turbulator section. The Reynolds number is determined using the effective diameter of a pin fin. For this purpose, figure 4.16 is used to make an approximation of the diameter of a pin fin. Based on figure 4.16 an effective pin fin diameter of $0.0003m$ is found. This leads to a Reynolds number of 5135. Again, the Prandtl nummer of 0.69 is used.

The correlation as provided by Metzger was found most suitable to use. Metzger's correlation is shown in equation 4.34. For $\frac{x}{D_p}$ a value of 1.5 can be asumed. [42] This results in heat transfer coefficient for the pin fin cooling section of approximately $9331 \frac{W}{m^2K}$.

$$Nu = 0.135 Re_D^{0.69} (\frac{x}{D_p})^{0.34} \tag{4.34}$$

4.6. INTERNAL TEMPERATURE DISTRIBUTION

The cooling air flowing through the cooling channels is heated by the blade wall. This effect will have to be taken into account while performing the steady-state analysis. The temperature increase over a distance Δx through the cooling channel is determined by relating the heat capacity of the cooling volume to the heat

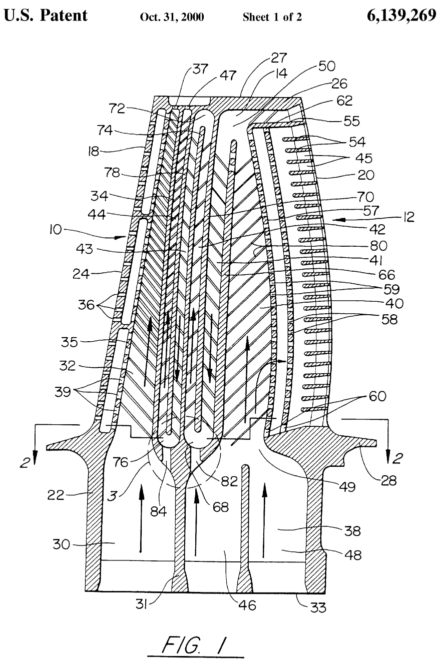

Figure 4.15: Schematic of internal cooling geometry. [38]

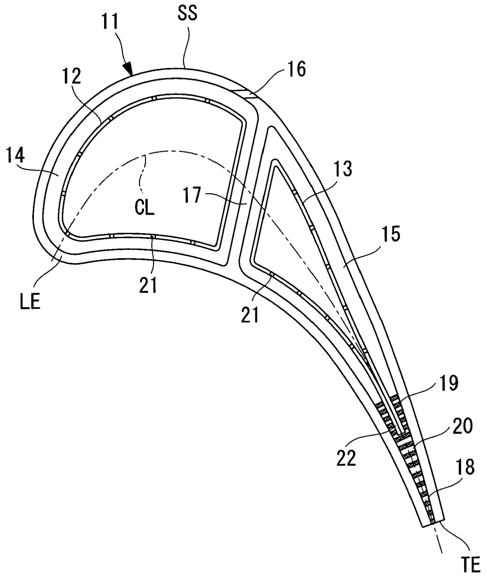

Figure 4.16: US patent 20100247290 used to determine effective pin fin diameter. [43]

convection at the blade wall. This is shown in equation 4.35, where h is the heat transfer coefficient, ρ is the density, C_P is the specific heat at constant pressure, V is the velocity of the flow, D is the diameter of the cooling channel, T_w is the wall temperature which is assumed to be constant and $T_{c,0}$ is the initial cooling temperature. This equation represents an exponential behaviour for the temperature increase, however since the cooling channel covers a relatively small distance, the temperature increase is assumed to be linear.

For the impingement, channel with turbulators and pin fin cooling sections this results in the temperature increase as shown in figure 4.17. Note that for the channels with turbulators the covered distance is three times as much as for the impingement and pin fin channels, as the turbulated channel is assumed to have two turns.

$$\frac{\Delta T_c}{\Delta x} = \frac{4h}{\rho C_P V D}(T_w - T_{c,0}) \tag{4.35}$$

4.7. FILM COOLING

Next to the internal cooling of the blade, the blade is also expected to be cooled by means of film cooling. With film cooling internal coolant air is exhausted through small holes on the airfoil surface which covers the blade in a protecting coolant layer, reducing the local fluid temperature next to the airfoil surface. The effect of the film cooling can be measured by means of the film cooling effectiveness, as provided in equation 4.36. Here T_g is the hot gas temperature, T_c is the coolant temperature exiting the film cooling holes and T_{film} is the actual temperature of the fluid covering the blade surface, also named the adiabatic wall temperature.

$$\eta = \frac{T_g - T_{film}}{T_g - T_c} \tag{4.36}$$

In order to determine the adiabatic wall temperature, an estimation of the film cooling effectiveness distribution over the blade surface is assumed, based on the trend provided in figure 4.18. [10] A second-order polynomial is interpolated for the film cooling effectiveness as provided in figure 4.18 with a maximum of 0.8 at the leading edge and a minimum of 0.4 at the trailing edge. For the coolant temperature, the internal

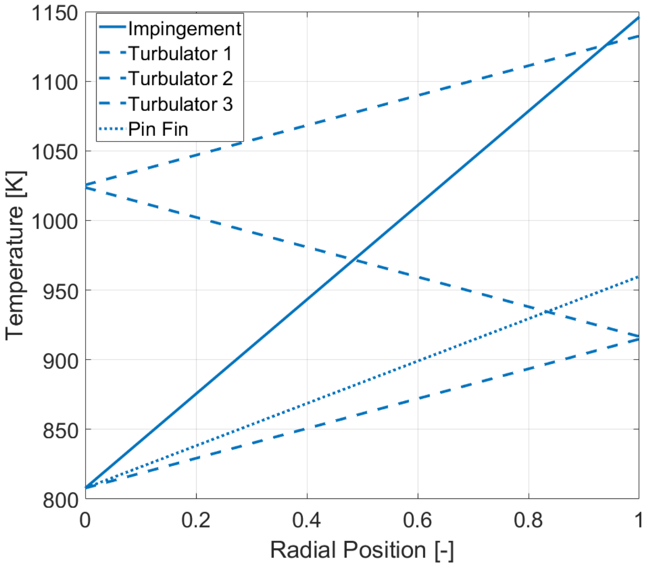

Figure 4.17: Temperature increase along cooling channels.

temperature distribution as provided in figure 4.17 is used. Similar as shown in figure 2.6 the channels with turbulators are assumed to start closer to the trailing edge of the blade and via two turns it moves forward towards the leading edge of the blade. Due to this, the film cooling air exited from the turbulated channel closest to the leading edge will have a higher temperature compared to the film cooling air exited from the turbulated channels closer to the trailing edge. The effect of the internal temperature distribution on the film temperature, or adiabatic wall temperature, is shown in figure 4.19. The effect of the turbulator channel configuration can be seen in figure 4.19 by the steep temperature increase at approximately 15% meridional location.

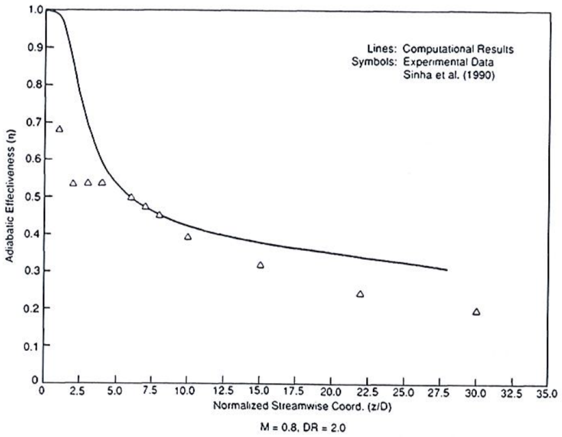

Figure 4.18: Prediction of adiabatic effectiveness of film cooling.[10]

4.8. RESULTS

Seven case studies have been performed to answer the research questions considering the effect of the amount of cooling air, the thickness of the TBC, the pattern factor and the power setting on component life. Results are gathered from Abaqus using a 1 quadratic tetrahedral mesh of type DC3D10. The internal geometry is incorporated in the model by generating three channels through the model. One for each method of internal cooling. This is shown in figure 4.20. The results for these case studies are shown below.

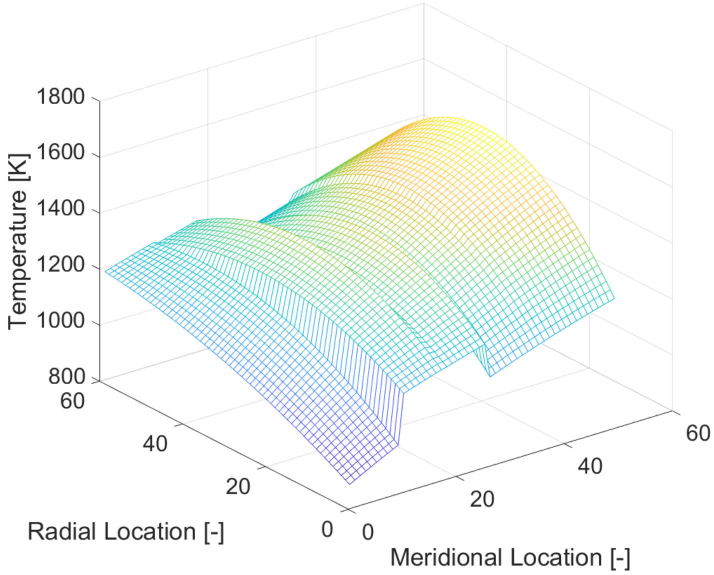

Figure 4.19: Film temperature.

4.8.1. CASE STUDIES

Seven case studies have been performed, covering the effect of the power setting, the amount of cooling air, the pattern factor and the TBC thickness. The following options are considered to asses the effect of each parameter.

- Power setting:
  1. Take-off
  2. Idle
- Amount of cooling air:
  1. 25% of core mass flow
  2. 20% of core mass flow
- Radial temperature distribution factor:
  1. 0.15
  2. 0.10
- Thermal barrier coating thickness:
  1. $400\mu m$
  2. $600\mu m$

Combination of the above parameter options leads to seven configurations to be tested as case study. These seven case studies are provided in table 4.2. The results for the temperature (without film cooling) and heat transfer coefficient for each case are provided in table 4.3.

Table 4.2: Case study configurations.

Parameter	**Case 1**	**Case 2**	**Case 3**	**Case 4**	**Case 5**	**Case 6**	**Case 7**
Power setting	Take-off	Take-off	Idle	Idle	Take-off	Take-off	Take-off
Cooling air	25%	20%	25%	20%	25%	25%	25%
$RTDF$	15%	15%	15%	15%	10%	15%	10%
t_{TBC}	$400\mu m$	$400\mu m$	$400\mu m$	$400\mu m$	$400\mu m$	$600\mu m$	$600\mu m$

Comparing the results for the case studies as provided in table 4.3, the following can be noted. Take-off and idle mode can be compared using cases 1 versus 3 and 2 versus 4. First looking at cases 1 versus 3 it can be noted that for all parameters provided in table 4.3 a significant difference is found. Also for case 2 versus 4 a significant difference can be noted for all parameters. This is as expected, as the mass flow and TIT are

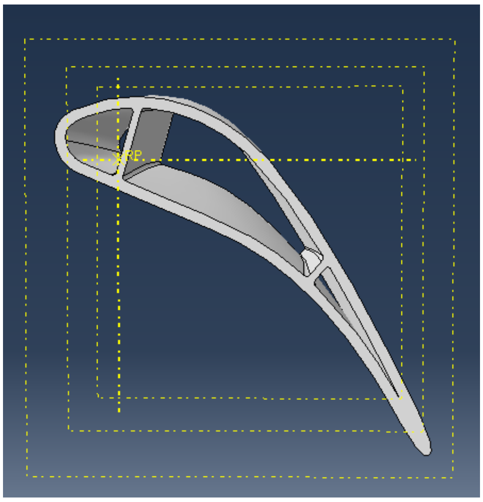

Figure 4.20: 3D model with cooling.

significantly lower for idle mode.

The effect of the cooling air can be found by comparing case 1 versus 2 and case 3 versus 4. It can be seen that a slight increase is found for the exterior parameters. This is as expected since the core mass flow is increased. The maximum internal temperatures have increased and the internal heat transfer coefficients have decreased. This is as expected since there is less cooling mass flow and therefore the velocity through the cooling channels decreases.

The effect of the $RTDF$ can be assessed by comparing case 1 versus 5. It can be noted that for the exterior parameters, only the maximum temperature has decreased, the heat transfer coefficients remain unchanged except for a 1 unit change in maximum heat transfer coefficient and 6 unit change in minimum heat transfer coefficient. The interior parameters all remain unchanged. This is as expected as the $RTDF$ only affects the exterior of the blade.

The effect of the TBC thickness can be found by comparing case 1 and 6. Changing the TBC thickness only affects the exterior of the blade. On the exterior of the blade it only affects the heat transfer coefficients. It can be seen that the maximum, mean and minimum external heat transfer coefficients are decreased significantly for the thicker TBC of case 6.

Case 7 combines a decreased $RTDF$ and a thicker TBC. It can be seen that this decreases the external maximum temperature similar as for case 5 and the maximum, mean and minimum external heat transfer coefficients similar as for case 6.

Table 4.3: Temperature and heat transfer coefficient results per case.

Parameter	**Case 1**	**Case 2**	**Case 3**	**Case 4**	**Case 5**	**Case 6**	**Case 7**	**Unit**
$T_{ext,max}$	2113	2126	1151	1156	2050	2113	2050	K
$h_{ext,max}$	1617	1629	1366	1384	1618	1152	1152	$\frac{W}{m^2K}$
$h_{ext,mean}$	1312	1334	924	952	1312	985	985	$\frac{W}{m^2K}$
$h_{ext,min}$	783	808	408	429	789	654	659	$\frac{W}{m^2K}$
$T_{imp,max}$	1146	1160	1264	1295	1146	1146	1146	K
h_{imp}	9963	9009	4934	4446	9963	9963	9963	$\frac{W}{m^2K}$
$T_{turb,max}$	1133	1140	1201	1216	1133	1133	1133	K
h_{turb}	7928	7203	3615	3298	7928	7928	7928	$\frac{W}{m^2K}$
$T_{pf,max}$	960	966	875	887	960	960	960	K
h_{pf}	9331	8597	4572	4229	9331	9331	9331	$\frac{W}{m^2K}$

Next to the temperature and heat transfer coefficients as provided in table 4.3 graphical visualisations of the results for the blade temperature are provided in figures 4.21 up until 4.27. Where figure 4.21 represents the baseline case. Note that in the figures the orientation of the blades from left to right is from tip to root and then from root to tip. In the figures it can be seen that for take-off the highest maximum blade temperature of 1440K is found for case 2 and the lowest maximum blade temperature of 1351K is found for case 7. Figures 4.21 up until 4.27 will be discussed in detail in the next subsections.

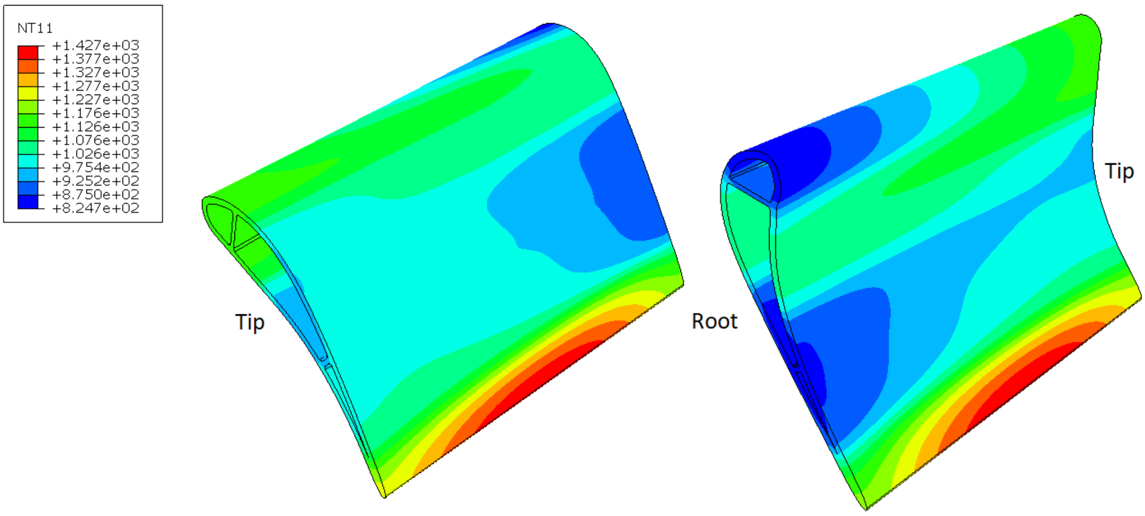

Figure 4.21: Case 1 results.

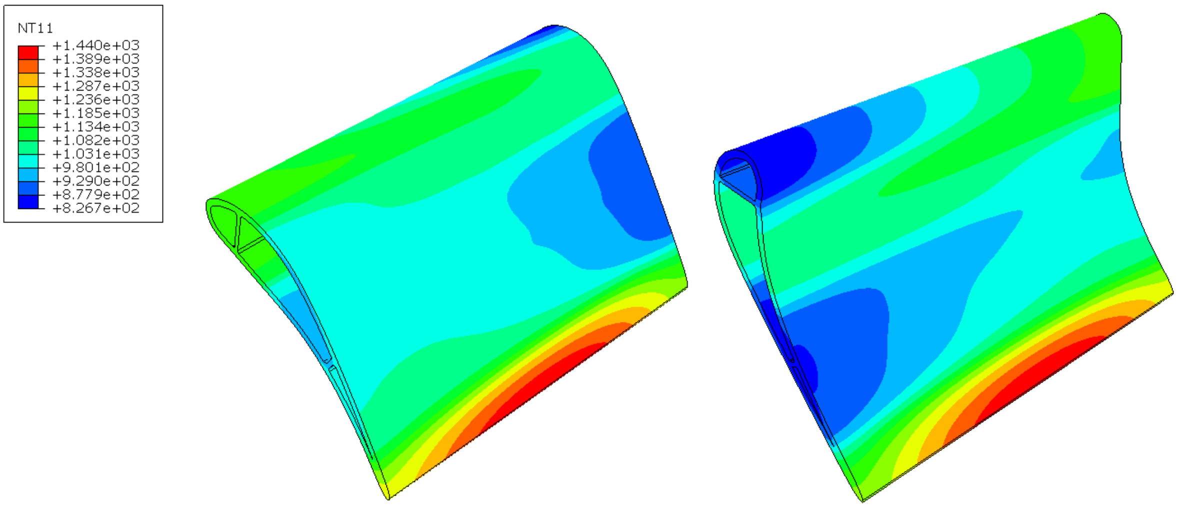

Figure 4.22: Case 2 results.

4.8.2. EFFECT OF POWER SETTING

The effect of the power setting, can be assessed by comparing case 1 with cases 3 and 4, for which the results are provided in figures 4.21, 4.23 and 4.24. For case 1 a maximum temperature of 1427K is found, compared to 924K for case 3 and 939K for case 4. This is a difference of 35% and 34%, respectively. For both power settings maximum temperatures are found at the trailing edge of the blade. However for the idle cases, also a maximum is found at the tip of the leading edge of the blade. This is expected to be caused due to an assumption made in the internal temperature distribution. For the internal temperature distribution it is assumed that the wall temperature for the take-off cases is constant at 1200K and for the idle cases is constant at 900K. It is expected that the 900K is a too high assumption and combined with the fact that for the impingement channels the highest heat transfer coefficients are found, the temperature will increase the most in the

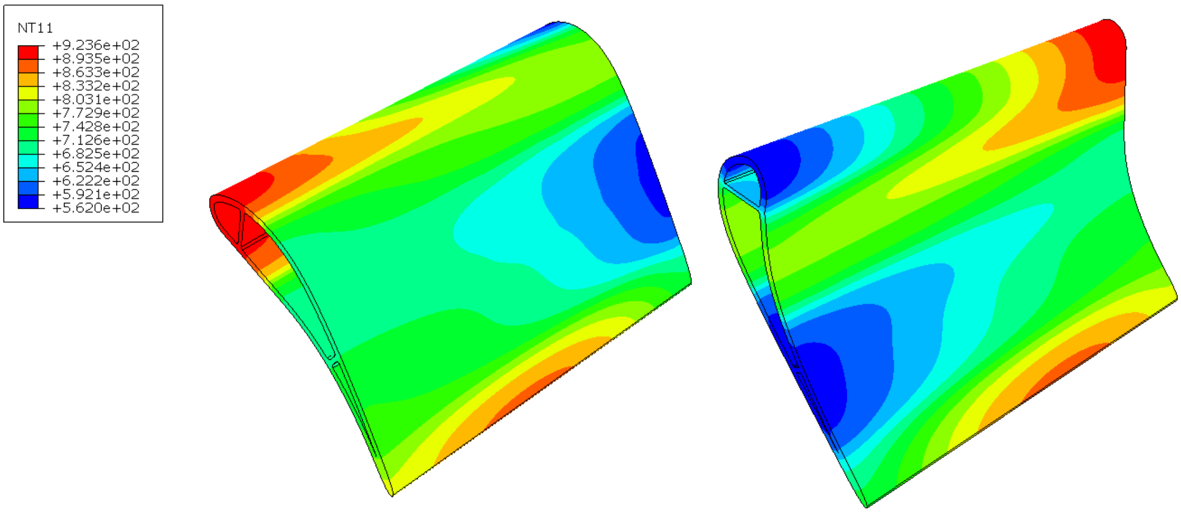

Figure 4.23: Case 3 results.

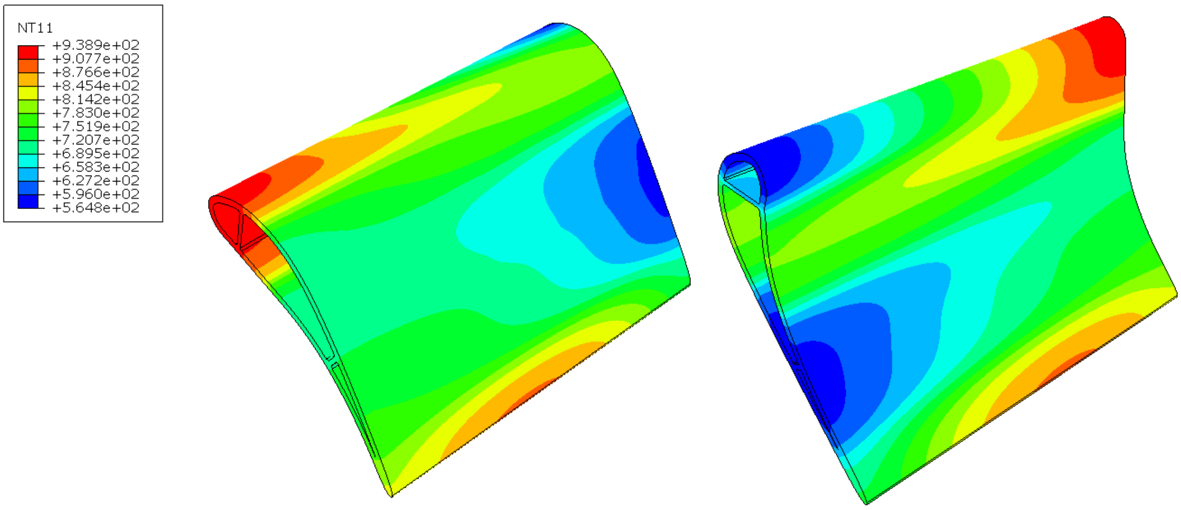

Figure 4.24: Case 4 results.

impingement channels. This makes it more difficult to cool the tip of the leading edge. The minimum temperature for the baseline case is found to be 824.7K, where for case 3 this is 562K and for case 4 this is 565K. The location of the minimum temperature is on the interior at the hub at the LE for all three cases. Which is as expected since this is the location where the cooling air enters the blade. Furthermore, considering the assumption that the maximum blade temperature for the superalloy is 1200K, this limit is largely achieved for the take-off case, except for the trailing edge of the blade. For the idle cases this limit is completely achieved.

4.8.3. EFFECT OF COOLING AIR

The effect of the amount of cooling air used, can be assessed by comparing case 1 with case 2 for take-off and case 3 with case 4 for idle mode, for which the results are provided in figures 4.21, 4.22, 4.23 and 4.24. For the take-off cases 1 and 2, it can be seen that decreasing the cooling air mass flow from 25% for case 1 to 20% for case 2, the maximum temperature increases from 1427K to 1440K, respectively. This is an increase of 1% with respect to the baseline case. The location of the maximum temperature is the same for both cases, at the trailing edge of the blade. For the cases in idle mode, case 3 and 4, it can be seen that decreasing the cooling air mass flow from 25% for case 3 to 20% for case 4 results in an increase in maximum temperature from 924K to 939K, respectively. This is an increase of almost 2%. The location for the maximum temperature is the same for both cases, at the trailing edge and at the tip on the leading edge. For both take-off and idle mode

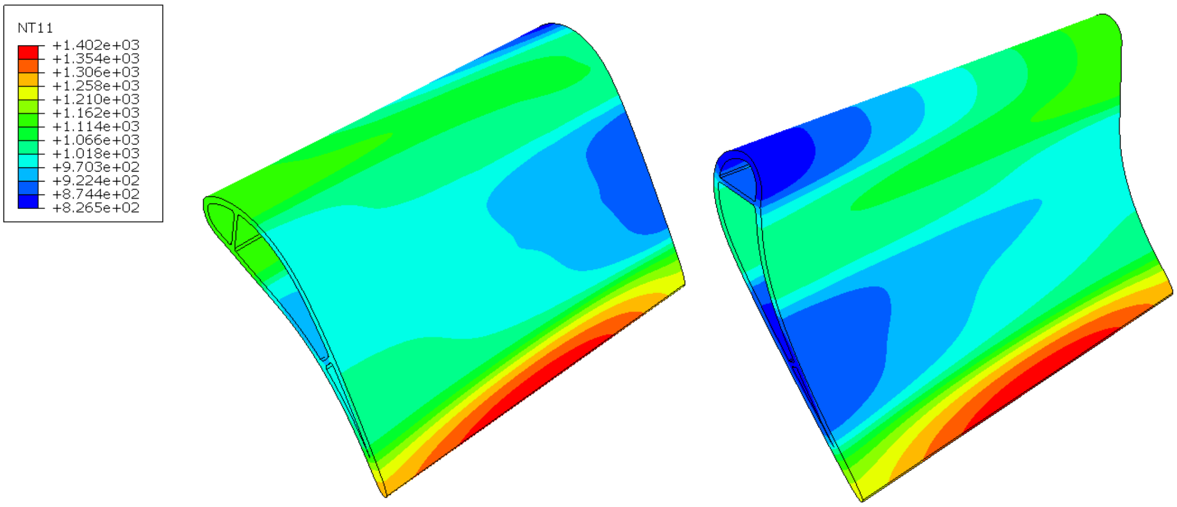
NT11
+1.402e+03
+1.354e+03
+1.306e+03
+1.258e+03
+1.210e+03
+1.162e+03
+1.114e+03
+1.066e+03
+1.018e+03
+9.703e+02
+9.224e+02
+8.744e+02
+8.265e+02

Figure 4.25: Case 5 results.

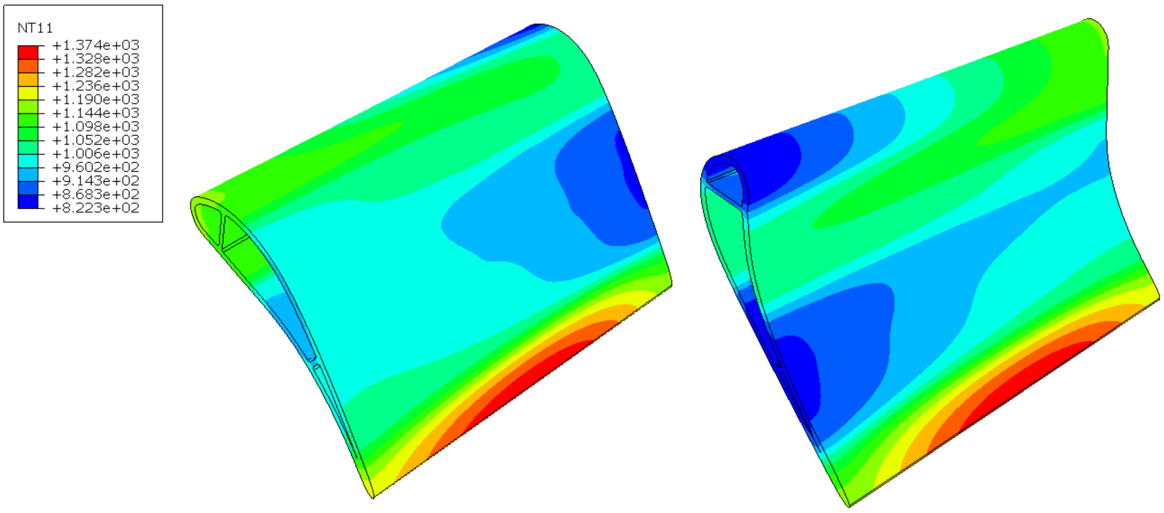
NT11
+1.374e+03
+1.328e+03
+1.282e+03
+1.236e+03
+1.190e+03
+1.144e+03
+1.098e+03
+1.052e+03
+1.006e+03
+9.602e+02
+9.143e+02
+8.683e+02
+8.223e+02

Figure 4.26: Case 6 results.

the temperature contours for different amounts of cooling air remain similar. The minimum temperature for case 1 compared to case 2 shows nearly no difference with 824.7K to 826.7K, respectively. Also for case 3 compared to case 4 there is nearly no difference with 562.0K to 564.8K, respectively. The location for the minimum temperature for both cases is on the interior at the hub at the LE. The assumed maximum blade temperature of 1200K is largely achieved at most parts of the blade for cases 1 and 2, except for the trailing edge of the blade. For cases 3 and 4 this limit is completely achieved.

4.8.4. EFFECT OF PATTERN FACTOR

The effect of the pattern factor, or radial temperature distribution factor, can be assessed by comparing case 1 with case 5, for which the results are provided in figures 4.21 and 4.25. It can be seen that for decreasing the $RTDF$ from 15% for case 1 to 10% for case 5 the maximum temperature is decreased from 1427K to 1402K, respectively. This is a decrease of almost 2%. The location for the maximum temperature is similar for both cases at the trailing edge of the blade. It can however be seen that for the decreased $RTDF$ of case 5 in figure 4.25, the temperature contour is spread out more in radial direction, which is as expected. This means that the temperatures at the root and tip of the blades for case 5 have been increased with respect to case 1. The minimum temperature for both cases is similar at 824.7K for case 1 and 826.5K for case 5. The location for the minimum temperature for both cases is on the interior at the hub at the LE. Regarding the assumed

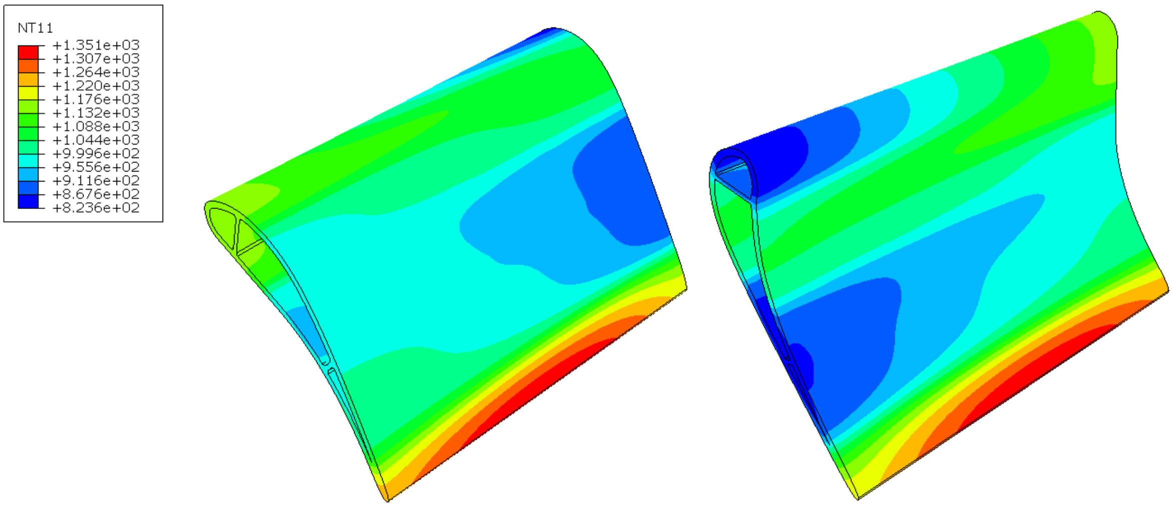

Figure 4.27: Case 7 results.

maximum blade temperature of $1200K$ case 5 performs slightly better in achieving this limit compared to case 1 and both cases mostly achieve this limit. For both cases, the trailing edge does not achieve this limit.

4.8.5. EFFECT OF TBC THICKNESS

The effect of the TBC thickness, can be assessed by comparing case 1 with case 6 and 7, for which the results are provided in figures 4.21, 4.26 and 4.27. The TBC thickness for case 1 is $400\mu m$ and for case 6 and 7 the thickness is $600\mu m$. This results in a decrease of the total external heat transfer coefficient of nearly 25%. It can be seen that for increasing the TBC thickness from $400\mu m$ for case 1 to $600\mu m$ for case 6, the maximum temperature decreases from $1427K$ to $1374K$. This is a difference of almost 4%. The temperature contour remains similar. The minimum temperature also remains similar at $824.7K$ for case 1 and $822.3K$ for case 6. In case 7 the TBC thickness is also increased to $600\mu m$ and also the $RTDF$ is decreased to 10%. The maximum temperature in case 7 is $1351K$. This is a decrease of 5% with respect to case 1 and a difference of nearly 4% with respect to case 5, for which the $RTDF$ also was 10%. So the effect of increasing the TBC thickness is significant. Regarding the assumed maximum blade temperature of $1200K$, all three cases mostly achieve this limit. Except at the trailing edge of the blade. Although cases 6 and 7 also come close to this limit at the trailing edge.

4.9. DISCUSSION ON HEAT TRANSFER ANALYSIS

The methodology used to acquire the results contains a significant amount of assumptions and estimations, especially due to the lack of information regarding the F135 rotor blades geometry and material properties. In order to assess the impact of these assumptions and estimations on the performance of the tool, a critical reflection is provided here, consisting of a discussion of the assumptions and estimations made and a sensitivity analysis on the performance of the tool. A summary of all estimations and assumptions is provided in this section, in the next subsection the impact will be assessed. The following assumptions and estimations have been made regarding the blade design.

- Constant axial velocity is considered through the stage.
- Constant mean diameter is considered.
- A degree of reaction of 0.4 is assumed.
- No losses are considered in the free-vortex design.
- Turbine inlet velocity is assumed to be completely axial.
- Blade angles are determined for the design point.
- Blade dimensions are estimated from a picture.
- 3D surface is generated by lofting three 2D airfoils.
- Tip Mach numbers are estimated around 1.03.

The following assumptions and estimations have been made for the external heat transfer distribution.

- Two RTDF's are assumed of 0.15 and 0.10.
- A symmetrical, parabolic distribution of the radial temperature is assumed.
- Only radial temperature distribution is considered, circumferential distribution is not considered.
- External convection heat transfer coefficient estimated through correlations.
- External velocity profile based on graph from theory.
- Wall temperature of $1200K$ assumed for radiation heat transfer calculations.
- TBC thickness assumed between $400-600\mu m$.
- CMSX-4 material properties assumed for the F135.

The following assumptions and estimations have been made regarding the internal heat transfer distribution and film cooling.

- Internal dimensions are estimated based on graphical examples.
- Cooling air per blade equally divided over impingement, turbulator and pin fin sections.
- Internal heat transfer coefficient is assumed to remain constant.
- Heat transfer coefficients estimated through correlations.
- Constant wall temperature of $1200K$ assumed for internal temperature distribution calculations.
- Film cooling effectiveness distribution estimated based on graph from theory.
- Film cooling temperature is based on internal temperature distribution.

4.9.1. DISCUSSION ON ASSUMPTIONS

Most of the assumptions regarding the blade design are assumptions that directly follow up on the free-vortex design as provided in theory. These are the constant axial velocity through the stage, constant mean diameter, a degree of reaction of 0.4, no losses and completely axial turbine inlet velocity. The velocity triangles as provided in figures 4.2, 4.3 and 4.4 behave as expected from hub to tip. Next to this, also the tip Mach numbers estimated of 1.03 are in coherence with theory. Therefore it is stated that these assumptions are valid and not of significant influence to the results and the performance of the tool.

In addition, the assumption regarding the 3D surface being generated by lofting three 2D airfoils is not expected to have a significant impact on the results nor the performance of the tool. Basically, the 3D blade model in Abaqus is used more as a visualisation tool for the results. If for example CFD would have been applied on the 3D model to determine the velocity profile along the blade surface, then the effect of the lofting would probably be noticeable. Due to the lofting the transitions over the blade surface are not smooth and this would have an effect on the boundary layer behaviour in CFD calculations.

The assumptions considering the blade angles to be determined for the design point and the blade dimensions that are estimated based on a picture are expected to be of an essential influence on the results, but not on the performance of the tool. If the blade angles would not be designed for take-off, this would affect the absolute and relative velocities and subsequently also the temperature distribution, which is analytically shown in equation 4.19. The blade dimensions are based on figure 2.2. The HPT rotor stage is visible on this picture, however on this scale a measurement error is easily made. Moreover, the scaling of the picture itself could be invalid. The performance of the tool is not expected to be affected, as the tool will be able to process the new data and generate different results.

For the external heat transfer distribution three assumptions consider the $RTDF$. The two $RTDF$ values that are assumed are based on literature, but cannot be validated for the F135. It is expected that these values are of a conservative, but still realistic magnitude. The impact of this assumption is significant for the results. However, as this parameter is used to assess the effect of variations, it can be stated as a plausible assumption.

Next to the values, also a symmetric, parabolic distribution is assumed for the radial temperature distribution. The influence of this assumption is expected to be mostly of impact for the location of the maximum temperature, as the value of the maximum temperature is determined before generating the distribution. So although this assumption is common practise at the NLR, the influence is expected to be significant.

Only the radial temperature distribution is considered, while also circumferentially a temperature profile exists, due to the burners that are divided over the circumferential area. For NGVs this assumptions would be more significant, as the location of the NGVs are fixed. For the rotor blades this assumption however is expected to be of medium influence, as they rotate through the temperature field. The maximum possible temperature difference is now considered for the rotor blade.

The external convective heat transfer coefficient is estimated through correlations. From literature it is found that these correlations itself are quite accurate, both the LE and flat plate correlations. In order to assure a smooth transition between the LE and the rest of the blade, the heat transfer coefficients on this transition have been interpolated. Although the results for the heat transfer coefficient are comparable to theory, it is advised to perform CFD analysis in the future to determine the heat transfer coefficients. For CFD however a detailed geometry is necessary.

Another assumption regarding the external convective heat transfer coefficient is that the external velocity profile is based on a graph from literature. The example velocity profile in the graph is expected to be valid for a general rotor blade, however it can not be stated as valid for the F135 rotor blade. Also for this it is recommended to perform CFD analysis in the future.

For the radiation heat transfer calculations a wall temperature of $1200K$ is assumed. This assumption is conservative for most of the case studies performed. Therefore the radiative heat transfer coefficient is also tested with a wall temperature of $1300K$ and an increase of $11.3\frac{W}{m^2K}$ is found. This is approximately a 0.3% increase in the total external heat transfer coefficient and can therefore be neglected.

The last two assumptions regarding the external heat transfer calculations consider the assumed TBC thickness of $400-600\mu m$ and the material properties of CMSX-4 that are assumed for the F135. A TBC thickness of $400\mu m$ is the thickest value found in literature for an EB-PVD TBC. [37] And the value of $600\mu m$ is solely added to assess the effect of an increased TBC. This assumption is therefore stated to be plausible. The assumption to use CMSX-4 is only made due to the lack of material properties regarding the F135 rotor blades. So, in essence, this assumption is of significant importance, however as CMSX-4 is a second generation superalloy, which is also expected for the F135 rotor blades, the results will be realistic.

The internal dimensions of the cooling channels are estimated based on graphical examples. Without information about the F135 rotor blade geometry, these estimations will have to be made, however this has a significant impact on the results. The values of the internal heat transfer coefficients and temperatures are still realistic however, but not valid for the F135.

For the internal heat transfer it was assumed that the cooling air per blade is equally divided over the impingement, turbulator and pin fin section. This is a safe assumption, as for the NASA Energy Efficient Engine the division in leading edge and trailing edge cooling air is also approximately equal. [10] So realistic results can still be expected, however not valid for the F135.

Furthermore, the internal heat transfer coefficients are assumed to remain constant throughout the cooling channels. This is a safe assumption without information about the internal channel geometry. When detailed internal geometry of the F135 is available, it is advised to perform CFD analysis to simulate the flow characteristics inside of the cooling channels.

The correlations that are now used for the internal heat transfer coefficients provide realistic values and can be implemented without knowing much about the exact geometry. For the development of the tool these correlations are therefore quite essential, however for future research, when exact life predictions are required, it is recommended to acquire the exact geometry and details of the internal cooling channels and perform CFD simulations to determine the heat transfer coefficients.

For the internal temperature distribution a constant wall temperature of $1200K$ is assumed for the take-off cases and a constant wall temperature of $900K$ is assumed for the idle cases. For the idle case studies performed this is a conservative assumptions. Therefore it is investigated how much the maximum temperatures are affected if a wall temperature of $800K$ is assumed. It is found that the impingement channel maximum temperature is decreased with 7.8%, the channels with turbulators maximum temperature is decreased with 7.5% and the pin fin channel maximum temperature is decreased with 4.2%. So this assumption will have impact on the results.

The last two assumption consider the film cooling effectiveness and the film cooling temperature. The film cooling effectiveness distribution is based on a graph found in literature. Although on a general basis, this will lead to realistic results, without the exact locations of the film cooling holes and without knowing the amount of film cooling holes, the results can not be stated as valid for the F135. This also holds for the film cooling temperature. It is however realistic to base the film cooling temperatures on the internal temperature distribution. As provided in figure 4.19, these assumptions now lead to a film cooling temperature distribution where temperature jumps can be found between the different cooling channels. This can be improved significantly if more information is known about the film cooling hole locations.

Generally concluding on the assumptions made. Most of the assumptions have a significant influence on the results. However, because the purpose of the research is focused on the development of the lifing analysis tool, for now the effects of the assumptions can be accepted. When in the future the tool will be used to perform actual lifing analysis for the F135 rotor blades, these assumptions will definitely have to be improved.

4.9.2. SENSITIVITY ANALYSIS

In order to assess the stability and accuracy of the model a sensitivity analysis is performed. For this sensitivity analysis parameters are changed by 1% and the resulting temperatures and heat transfer coefficients are compared with the baseline case. The results for the blade exterior parameters, the blade interior parameters and the film cooling parameters can be found in tables 4.4, 4.5 and 4.6, respectively.

For the blade exterior parameters, as provided in table 4.4 it can be seen that the parameters that have the largest influence on the maximum external temperature, are the $RTDF$ and T_{t_4}. Next to the $RTDF$ and T_{t_4}, the radius r and mass flow W_4 also have a slight influence on the maximum temperature. The influence of the other parameters is negligible for the maximum temperature. For the maximum, mean and minimum external heat transfer coefficient, the TBC thickness t_{TBC} and TBC conductivity k_{TBC} show the highest influence. For the maximum and minimum external heat transfer coefficient also the turbulence intensity Tu has a significant influence. This is only for the maximum and minimum heat transfer coefficient because the maximum is found at the LE and the equation used to determine the LE heat transfer coefficient uses Tu. The minimum heat transfer coefficient is found on the transition between LE and the remaining part of the blade. Since the heat transfer coefficient for this transition is interpolated between the heat transfer coefficients found for the LE and remaining part of the blade, also the minimum heat transfer coefficient is affected by Tu. Other parameters that have a slight influence on the maximum, mean and minimum heat transfer coefficients are the radius r, mass flow W_4, TIT. For the maximum heat transfer coefficient the leading edge diameter D_{LE} also has a slight influence.

Table 4.4: Sensitivity Analysis External Heat Transfer For 1 Percent Change Of Parameters In Left Column.

Parameter	T_{max}	**Diff**	h_{max}	**Diff**	h_{mean}	**Diff**	h_{min}	**Diff**
Baseline	2113		1617		1312		783	
r	2115	0.1%	1615	0.1%	1308	0.3%	778	0.6%
RPM	2113	0.0%	1617	0.0%	1312	0.0%	783	0.0%
W_4	2111	0.1%	1619	0.1%	1315	0.2%	786	0.4%
T_{t_4}	2136	1.1%	1619	0.1%	1314	0.2%	785	0.3%
$R_{reaction}$	2113	0.0%	1617	0.0%	1312	0.0%	783	0.0%
$RTDF$	2126	0.6%	1617	0.0%	1312	0.0%	781	0.3%
Tu	2113	0.0%	1625	0.5%	1312	0.0%	779	0.5%
D_{LE}	2113	0.0%	1616	0.1%	1312	0.0%	783	0.0%
t_{TBC}	2113	0.0%	1604	0.8%	1303	0.7%	779	0.5%
k_{TBC}	2113	0.0%	1630	0.8%	1320	0.6%	786	0.4%

For the blade interior parameters, as provided in table 4.5, it can be seen that the maximum temperatures are only slightly influenced by all interior parameters. The largest influence is found for the maximum temperature in the pin fin channels by changing the bleed temperature T_{t_3}. For the internal heat transfer coefficient the number of blades N_{blades} and the cooling mass flow W_{cool} show a significant influence. The radius also has a significant influence on the impingement heat transfer coefficient. This is because the effective impingement area is determined as a percentage of the radius. Variation of the diameters and effective diameters for impingement, turbulators and pin fins all show a significant impact. This is as expected since the Reynolds numbers used to calculate the Nusselt numbers are a function of these diameters.

For the sensitivity analysis for film cooling only one parameter is analysed, as can be seen in table 4.6. The film cooling effectiveness shows an intermediate to significant impact on the maximum, minimum and mean film temperature.

Table 4.5: Sensitivity Analysis Internal Heat Transfer For 1 Percent Change Of Parameters In Left Column.

	T_{imp}	**Diff**	h_{imp}	**Diff**	$T_{turb,}$	**Diff**	h_{turb}	**Diff**	T_{pf}	**Diff**	h_{pf}	**Diff**
Baseline	1146		9963		1133		7928		960		9331	
N_{blades}	1148	0.2%	9820	1.4%	1134	0.1%	7822	1.3%	961	0.1%	9224	1.1%
T_{t_3}	1148	0.1%	9990	0.3%	1134	0.2%	7939	0.1%	965	0.5%	9349	0.2%
r	1147	0.1%	9789	1.7%	1136	0.3%	7928	0.0%	961	0.2%	9331	0.0%
W_{cool}	1145	0.1%	10051	0.9%	1132	0.1%	7993	0.8%	959	0.0%	9396	0.7%
D_{imp}	1147	0.0%	9930	0.3%								
$D_{eff,imp}$	1144	0.2%	9795	1.7%								
D_{turb}					1130	0.2%	7785	1.8%				
D_{pf}									959	0.1%	9203	1.4%
$D_{eff,pf}$									959	0.0%	9303	0.3%

Table 4.6: Sensitivity Analysis Film Cooling For 1 Percent Change In Film Cooling Effectiveness.

Parameter	T_{max}	**Diff**	T_{min}	**Diff**	T_{mean}	**Diff**
Baseline	1624		876		1318	
η_{film}	1619	0.3%	869	0.8%	1312	0.5%

Concluding, it can be stated that for the exterior blade parameters, the $RTDF$, the turbulence intensity Tu, the TBC thickness t_{TBC} and the TBC conductivity k_{TBC} show such a significant impact, that assumptions for these parameters will lead to a critical influence on the results. For the internal blade parameters the same can be said for all parameters. Also for the film cooling effectiveness this statement holds. For improvement of the lifing analysis tool it is therefore important that the exact value of these parameters are determined.

4.9.3. FUTURE RESEARCH

As stated repetitively, for future research it is recommended to acquire the actual geometry and material properties of the F135 rotor blades. Also CFD results of the combustor outlet temperatures would be a great addition to determine the actual radial and circumferential temperature pattern. When this is available it is recommended to perform CFD analyses on the blade to determine the internal and external heat transfer characteristics. Currently an assumption for the blade wall temperature is used to determine the radiation heat transfer coefficient and the internal temperature distribution. For future research it is recommended to either implement an iteration between the blade temperature calculations and the external and internal heat transfer characteristics or use a conjugate heat transfer methodology. For computation efficiency a conjugate heat transfer analysis could be implemented in the CFD model in which the calculations of the external and internal flow and heat transfer are coupled together with the blade conduction.

5

LIFING ANALYSIS

The last part of the tool to be developed is the lifing model. This part consists of a thermo-mechanical part that determines the stresses induced by thermal differences and by mechanical loading. The last part is the lifing analysis itself, for which the failure modes low cycle fatigue and creep are considered. Since no material properties are known for the F135 rotor blades, there is no possibility to produce accurate results within this part of the tool for the F135 engine. However, in order to show that the lifing analysis tool is working accordingly, material data of the superalloys CMSX-4 and Inconel 718 are used, as provided by the NLR. This chapter will provide the methodology and results for the thermo-mechanical model and the lifing model for creep and low cycle fatigue.

5.1. THERMO-MECHANICAL MODEL

Basically three types of mechanical loading are acting on the rotor blade, namely pressure loading, thermal loading and centrifugal loading. The centrifugal loading is induced by the rotation of the blade. The thermal loading is induced by thermal differences within the blade surface. The pressure loading is induced by the pressure differences acting on the blade. Since the pressure loading is only of a small order compared to the other two, this is neglected in the thermal-mechanical model. [44]

The thermal boundary conditions have been determined in the previous chapter, chapter 4, and will subsequently be used as input for the thermal loading. The mechanical boundary condition consists of an encastre at the root of the blade, where the blade would be attached to the disk. In reality, a rotor blade is attached to the disk using a dovetail configuration. However, for simulation simplicity this is left out of the configuration here. This will however have an effect on the results at the root of the blade. The centrifugal loading is determined with the centrifugal force, for which the rotational velocity is the input. In figure 5.1 the boundary condition and centrifugal force acting on the blade are shown. In order to conduct the calculations, a mesh containing 218328 quadratic tetrahedral elements of type C3D10 is generated. The mesh is shown in figure 5.2.

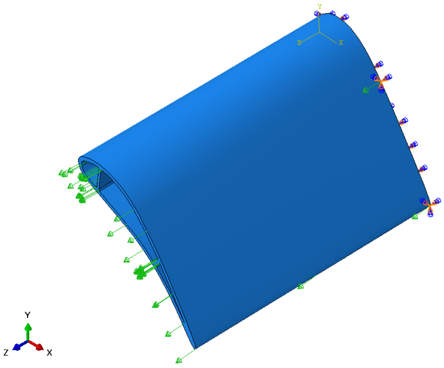

Figure 5.1: Boundary conditions used in Abaqus model.

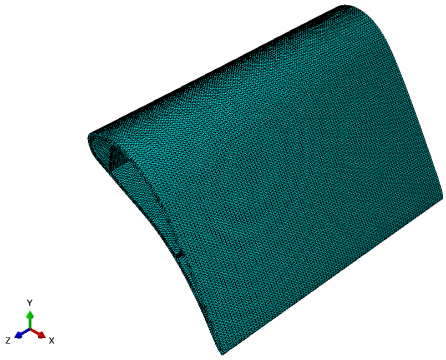

Figure 5.2: C3D10 mesh used in Abaqus model.

5.2. RESULTS THERMO-MECHANICAL MODEL

In figures 5.3 up until 5.13 the Von Mises stresses acting on the blade for each of the case studies are provided. The Von Mises stress is preferred since this can be related to the yield strength of the material. The yield strength of CMSX-4 is provided in appendix C. In figures 5.3 and 5.4 the Von Mises stress induced by centrifugal loads only are provided for take-off at 15200RPM and idle mode at 12020RPM are provided, respectively. Note that in the figures the orientation of the blades from left to right is from tip to root and then from root to tip. As expected, higher stresses are found for take-off with respect to idle mode. For take-off the maximum stress induced by centrifugal load only is in the order of 400MPa and for idle mode this is in the order of 300MPa. The stresses due to centrifual loading only increase from tip to root, which is also as expected as the blade is encastred at the root.

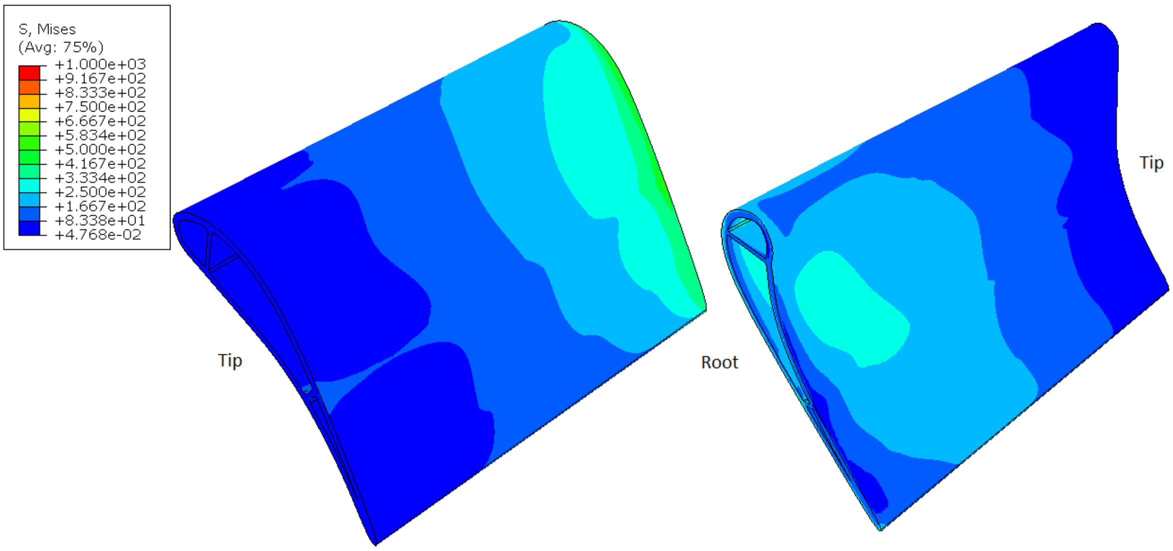
S, Mises
(Avg: 75%)
+1.000e+03
+9.167e+02
+8.333e+02
+7.500e+02
+6.667e+02
+5.834e+02
+5.000e+02
+4.167e+02
+3.334e+02
+2.500e+02
+1.667e+02
+8.338e+01
+4.768e-02
Tip
Root
Tip

Figure 5.3: Case 1 stress results rotation only at 15200 RPM.

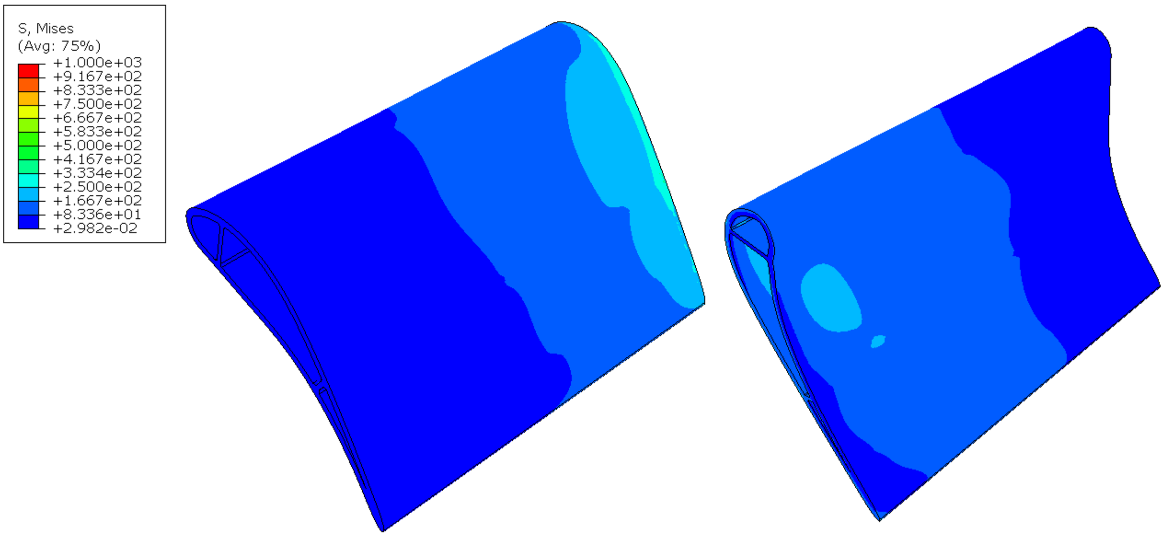
S, Mises
(Avg: 75%)
+1.000e+03
+9.167e+02
+8.333e+02
+7.500e+02
+6.667e+02
+5.833e+02
+5.000e+02
+4.167e+02
+3.334e+02
+2.500e+02
+1.667e+02
+8.336e+01
+2.982e-02

Figure 5.4: Case 3 stress results rotation only at 12020 RPM.

In figures 5.5 and 5.6 the stresses due to thermal loading only are provided for take-off and idle mode, respectively. As expected, higher thermal stresses are found for take-off. The maximum stress due to thermal loading at take-off is in the order of 450MPa and for idle mode this is in the order of 180MPa. This is notably lower compared to the stresses due to centrifugal loading only.

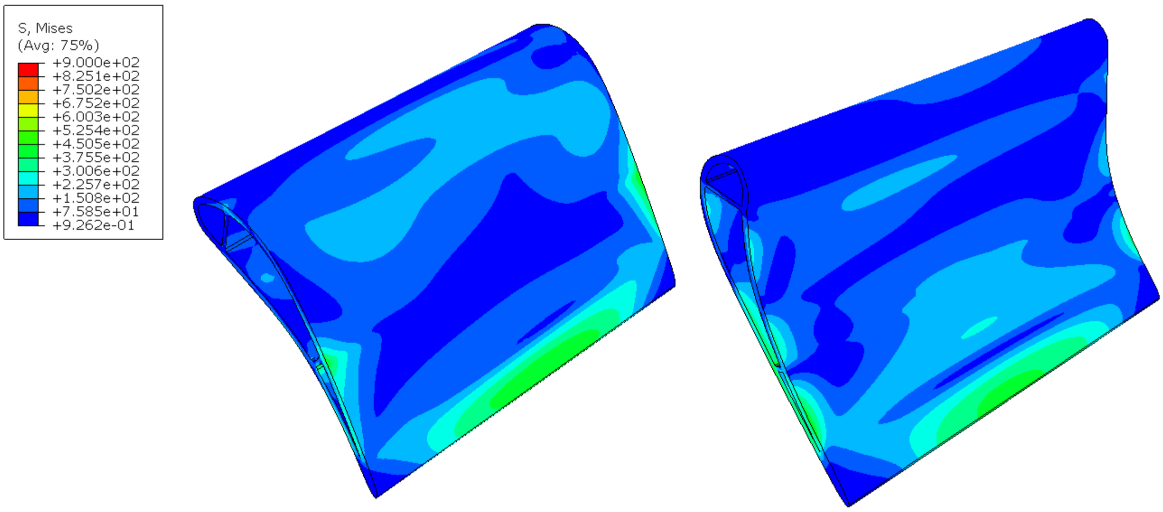

Figure 5.5: Case 1 thermal stress results.

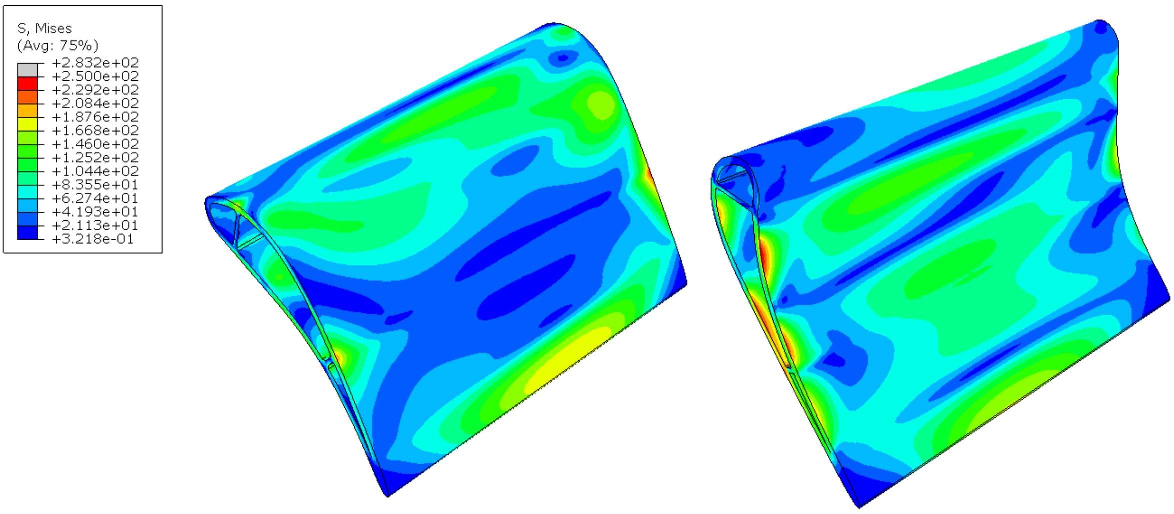

Figure 5.6: Case 3 thermal stress results.

In figures 5.7 up until 5.13 the Von Mises stresses with all loads applied, so combining centrifugal and thermal loads, are provided for each of the seven case studies. Due to the assumed encastre boundary condition located at the blade root extreme high stresses where found at the root. In order to keep these high stresses out of the scaling, the stresses have been cut off at $900MPa$. In the following subsections the research questions regarding the effect of the power setting, the amount of cooling air used, the pattern factor and the TBC thickness will be assessed. Note that without the exact material properties of the F135 rotor blades, the results are not accurate, however the effects of variations in these before mentioned parameters can be analysed.

5.2.1. EFFECT OF POWER SETTING

The effect of the power setting can be assessed by comparing case 1 with cases 3 and 4, for which the results are provided in figures 5.7, 5.9 and 5.10. The maximum total stress for case 1 is in the order of $550MPa$ and for cases 3 and 4 this is in the order of $300MPa$. For case 4 the stresses are slightly lower compared to case 3. Next to this, it can also be seen that the overall stresses are notably lower for the idle mode cases compared to take-off. This is as expected, since the TIT at idle mode at $1200K$ is significantly lower than the $2200K$ at take-off and also because the rotational speed at idle mode of $12020RPM$ is lower compared to take-off at $15200RPM$. So both the stresses due to thermal loading as well as centrifugal loading are lower for idle-mode, hence the lower Von Mises results.

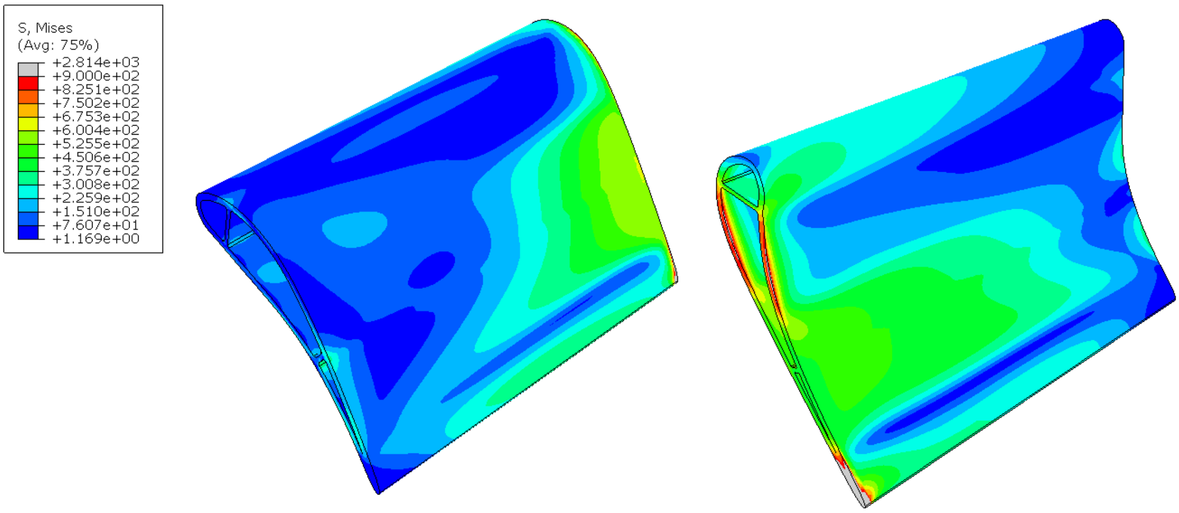
S, Mises
(Avg: 75%)
+2.814e+03
+9.000e+02
+8.251e+02
+7.502e+02
+6.753e+02
+6.004e+02
+5.255e+02
+4.506e+02
+3.757e+02
+3.008e+02
+2.259e+02
+1.510e+02
+7.607e+01
+1.169e+00

Figure 5.7: Case 1 total stress results.

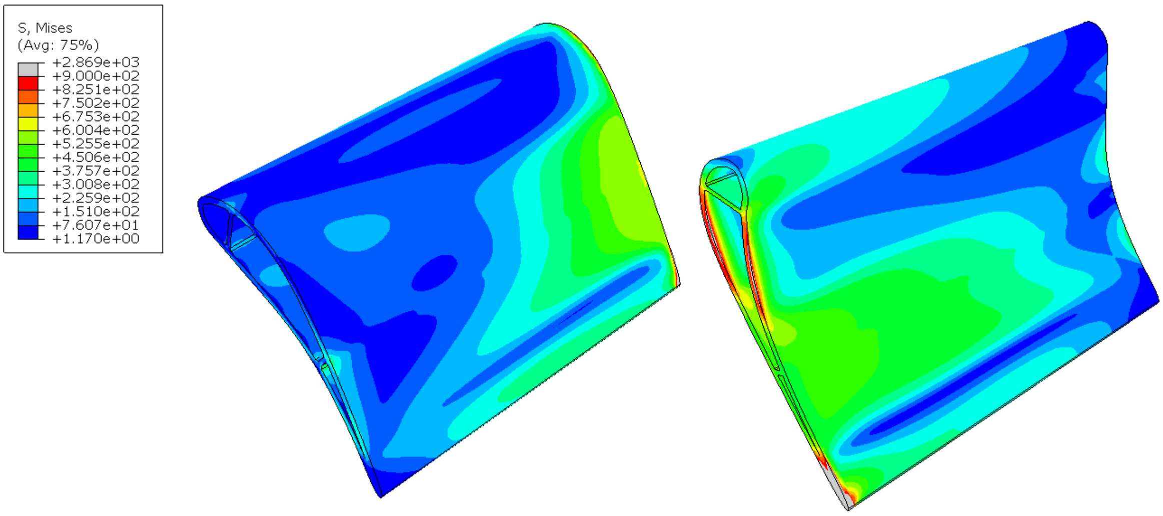
S, Mises
(Avg: 75%)
+2.869e+03
+9.000e+02
+8.251e+02
+7.502e+02
+6.753e+02
+6.004e+02
+5.255e+02
+4.506e+02
+3.757e+02
+3.008e+02
+2.259e+02
+1.510e+02
+7.607e+01
+1.170e+00

Figure 5.8: Case 2 total stress results.

The location of the maximum stress for take-off as well as idle mode is at the root where the turbulator and pin fin cooling channels begin. It is expected that the stresses at the root are highest, due to the encastre boundary condition.

5.2.2. EFFECT OF COOLING AIR

The effect of the amount of cooling air used can be assessed by comparing case 1 with case 2 for take-off and case 3 with case 4 for idle mode, for which the results are provided in figures 5.7, 5.8, 5.9 and 5.10. Where 25% of the compressor mass flow is used for cooling in cases 1 and 3, and 20% compressor mass flow is used for cooling in cases 2 and 4.

For both the cases in take-off and in idle mode, no significant difference can be found. The contour and the values of the Von Mises stress are the same. Therefore, the effect of changing the cooling air with 5% can be stated to have no effect on the Von Mises stress. This is not as expected. However, the difference of 5% cooling air is with respect to the total amount of cooling air used. The amount of cooling air used for the rotor blades is only decreased by 0.5%. So the effect of 5% in the total amount of cooling air is probably more evident on the nozzle guide vanes.

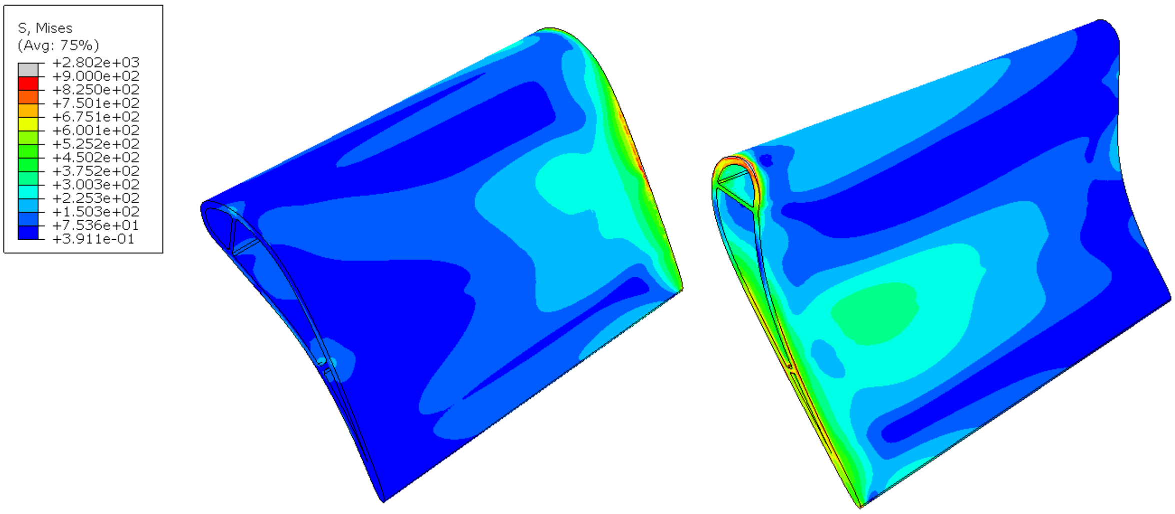

Figure 5.9: Case 3 total stress results.

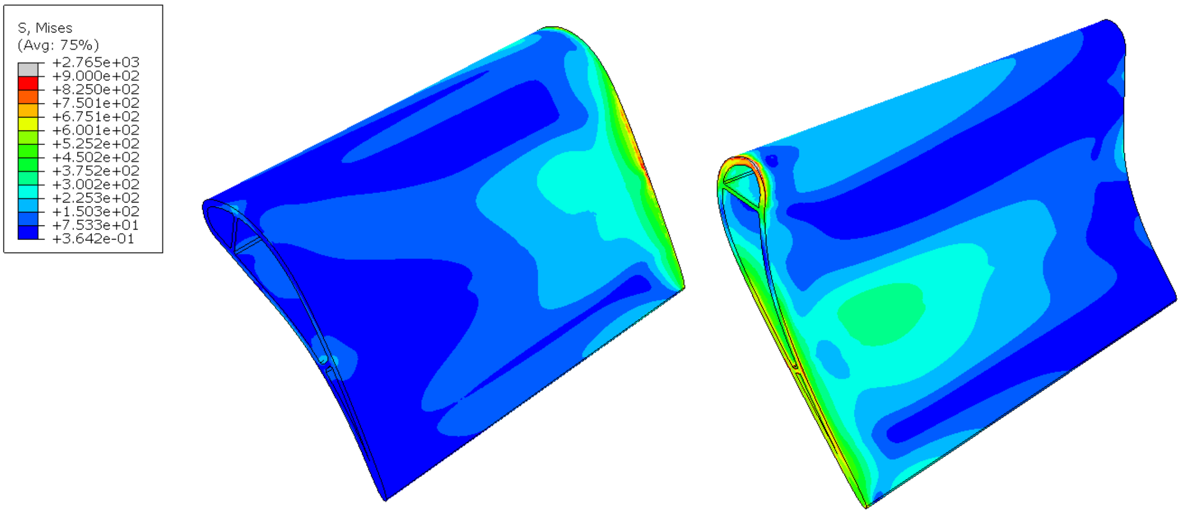

Figure 5.10: Case 4 total stress results.

5.2.3. EFFECT OF PATTERN FACTOR

The effect of the pattern factor can be assessed by comparing case 1 with case 5, for which the results are provided in figures 5.7 and 5.11. For case 1 a $RTDF$ of 15% is used and for case 5 a $RTDF$ of 10% is used. The maximum stresses for both cases are in the order of $550MPa$ and are located on the root where the turbulator and pin fin cooling channels begin. Overall, the Von Mises stress is of the same magnitude and pattern for both cases.

5.2.4. EFFECT OF TBC THICKNESS

The effect of the TBC thickness can be assessed by comparing case 1 with cases 6 and 7, for which the results are provided in figures 5.7, 5.12 and 5.13. For case 1 a TBC thickness of $400\mu m$ is used and for cases 6 and 7 a TBC thickness of $600\mu m$ is used. For case 7 also a lowered $RTDF$ of 10% is used.

When first comparing case 1 with case 6 it can be seen that the location and magnitude of the Von Mises stress is the same. Next to this, also the pattern of the stress is the same. When comparing case 6 and 7, also no difference is found for the values or pattern of the Von Mises stress.

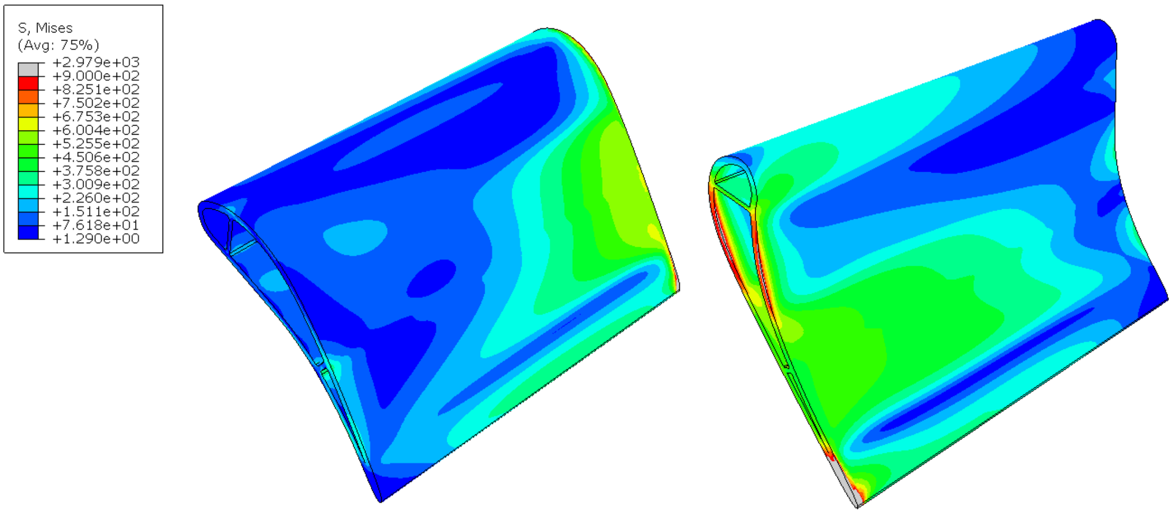

Figure 5.11: Case 5 total stress results.

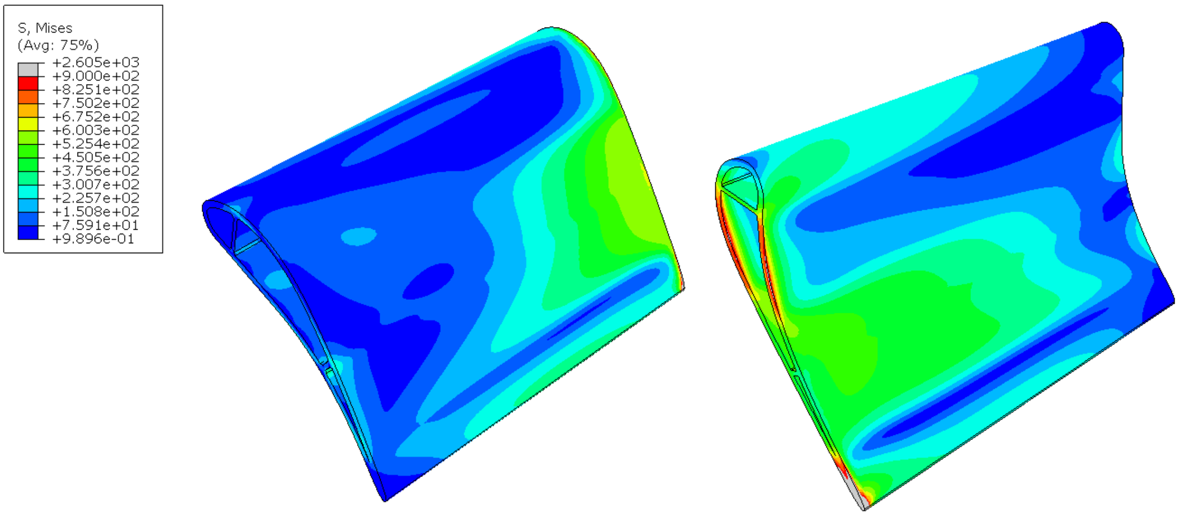

Figure 5.12: Case 6 total stress results.

5.3. LIFING MODEL

The last step of the tool is the analyse the effect of the mechanical loading on the life of the blade. For this purpose the thermo-mechanical model will be coupled to a lifing model. For each failure mechanism that is considered, a separate lifing model is required. For the F135 rotor blade the failure modes of creep and low cycle fatigue (LCF) are considered. Creep is the tendency of the material to deform permanently under the influence of mechanical stresses. LCF is the behaviour of plastic deformation for a low number of cycles to failure. It is assumed that there is no interaction between the creep and low cycle fatigue damage accumulation.

In order to describe the creep behaviour of the rotor blades the Norton-Bailey creep law is used. The Norton-Bailey creep law is provided in equation 5.1, where $\dot{\epsilon}$ is the creep strain rate, B and n are material parameters, σ is the stress, Q_a is the activation energy, R is the universal gas constant of $8.3145\frac{kJ}{kmolK}$ and T is the material temperature. From equation 5.1 it is clear that detailed material knowledge is required in order to perform a valid lifing analysis for creep. However, since the material properties are proprietary and no open source data is available for this, for now the material properties of Inconel 718 material will be used and are provided in table 5.1. The values for these parameters have empirically been determined for Inconel 718 and are expected to be different for the actual F-35 rotor blade material. [44]

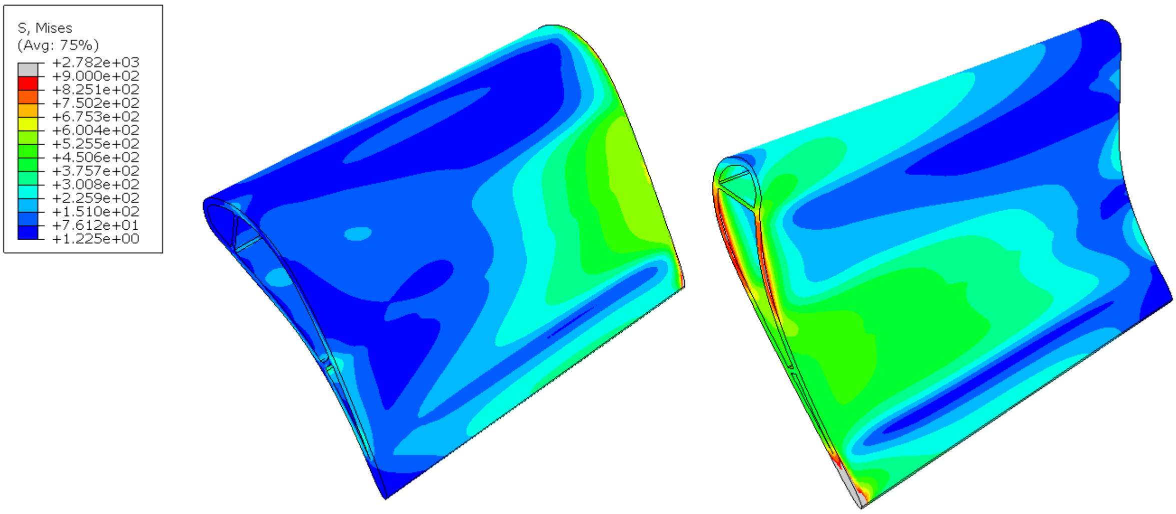

Figure 5.13: Case 7 total stress results.

$$\dot{\epsilon} = B\sigma^n e^{\frac{-Q_a}{RT}} \tag{5.1}$$

Table 5.1: Creep material properties for Inconel 718.

Parameter	**Value**	**Unit**
Q_a	443851	$\frac{J}{mol}$
B	$7.132 \cdot 10^{-32}$	–
n	16.96	–

In order to describe the LCF behaviour of the rotor blades equations 5.2 and 5.3 are used, where N_f is the number of cycles to failure, σ_{eq} is the equivalent stress, σ_a is the stress amplitude and σ_m is the mean stress. The constants in the equations are empirically derived material properties for Inconel 718 and will be different for the actual F-35 rotor blade material. As can be seen in the equations, the fatigue properties normally do not strongly depend on temperature. As stress spectrum it is assumed that from zero stress to the stress at a certain condition, for example take-off or idle mode, can be considered as one cycle. The largest in absolute value of the principal stresses is used to obtain the number of cycles to failure. [44]

$$log(N_f) = 8.18 - 2.07log(\sigma_{eq} - 63) \tag{5.2}$$

$$\sigma_{eq} = \sigma_a + 0.40\sigma_m \tag{5.3}$$

5.4. RESULTS LIFING MODEL

As described above, the material properties of Inconel 718 are assumed for the creep and LCF behaviour. This has a significant effect on the validity of the results of the lifing analysis. It is expected that the magnitude of the results are not accurate. However, the overall pattern along the blade for the creep strain rate and LCF is expected to be reliable. The results will therefore be used to describe the effects of variation in power setting, amount of cooling air, pattern factor and TBC thickness on a preliminary basis. And mostly the results are used as a proof-of-concept of the tool to be operational.

In figures 5.14 up until 5.20 the results for the creep strain rate are provided for each of the seven case studies. In figures 5.21 up until 5.27 the results for the LCF behaviour are provided, also for each of the seven case studies. It should be noted that a logarithmic scale is used for the results of both creep strain rate and LCF behaviour. The effect of the power setting, amount of cooling air used, pattern factor and TBC thickness will be described in the following subsections.

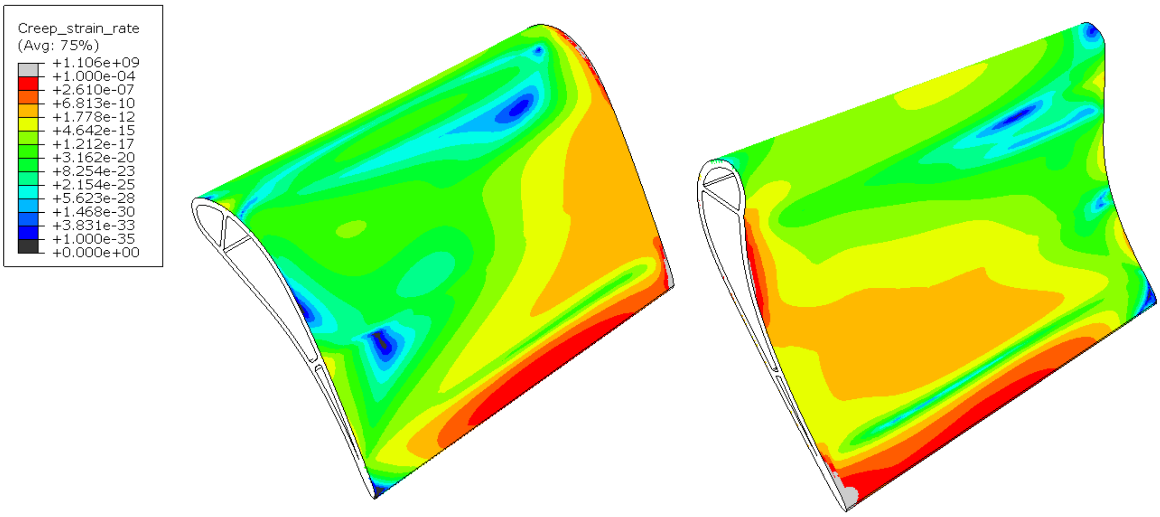
Creep_strain_rate
(Avg: 75%)
+1.106e+09
+1.000e-04
+2.610e-07
+6.813e-10
+1.778e-12
+4.642e-15
+1.212e-17
+3.162e-20
+8.254e-23
+2.154e-25
+5.623e-28
+1.468e-30
+3.831e-33
+1.000e-35
+0.000e+00

Figure 5.14: Case 1 creep strain rate results.

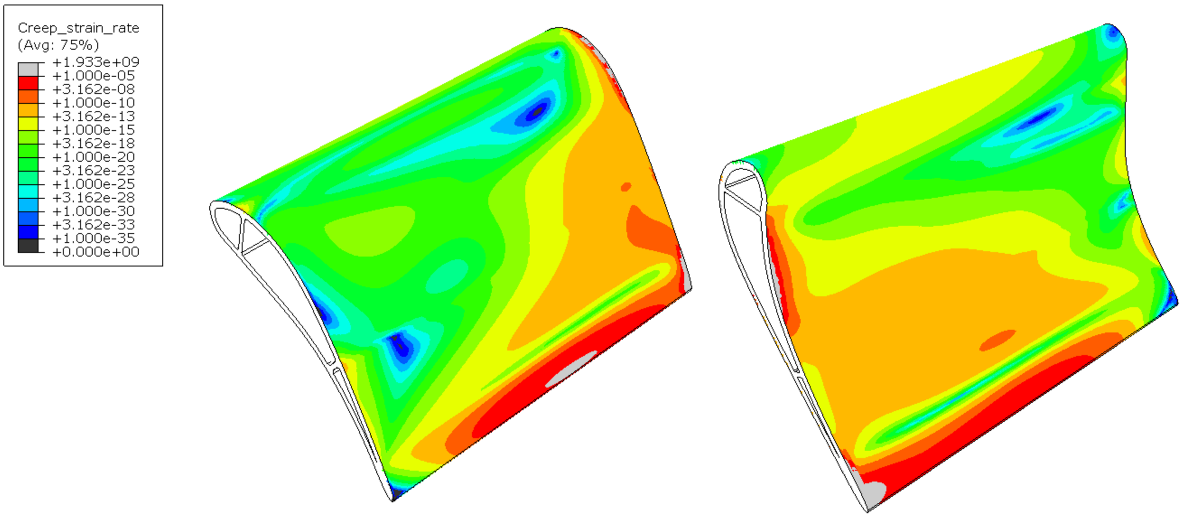
Creep_strain_rate
(Avg: 75%)
+1.933e+09
+1.000e-05
+3.162e-08
+1.000e-10
+3.162e-13
+1.000e-15
+3.162e-18
+1.000e-20
+3.162e-23
+1.000e-25
+3.162e-28
+1.000e-30
+3.162e-33
+1.000e-35
+0.000e+00

Figure 5.15: Case 2 creep strain rate results.

5.4.1. EFFECT OF POWER SETTING

The effect of the power setting can be assessed by comparing case 1 with cases 3 and 4, for which the results are provided in figures 5.14, 5.16 and 5.17 for the creep strain rate and in figures 5.21, 5.23 and 5.24 for the LCF behaviour. For case 1 take-off is considered as power setting and for cases 3 and 4 idle mode is considered as power setting.

The magnitude of the maximum creep strain rate should be disregarded, because the material properties of Inconel 718 are assumed and this material does not possess good creep resistance. The maximum creep strain position for each of the three cases is similar as for the maximum Von Mises stress and located on the trailing edge of the blade. This makes sense as the creep strain is a function of the Von Mises stress to the power n. The creep strain rate for cases 3 and 4 is more realistic compared to case 1, as the TIT of $1200K$ lies close to the operational range of Inconel 718. Because the Von Mises stress is a leading factor for the creep strain rate, the effect of the power setting on the creep strain rate is similar as for the Von Mises stress. For idle-mode the creep strain rate is much lower compared to take-off.

Regarding the LCF behaviour, the results are more realistic than the creep strain rate results, as the behaviour of Inconel 718 is better for fatigue. The results for take-off in case 1 show that most part of the blade will be able to sustain 73 cycles. This low amount of cycles to failure is partly caused due to the material choice, but also because a loading from zero to maximum stress is assumed, while in reality for engine start-

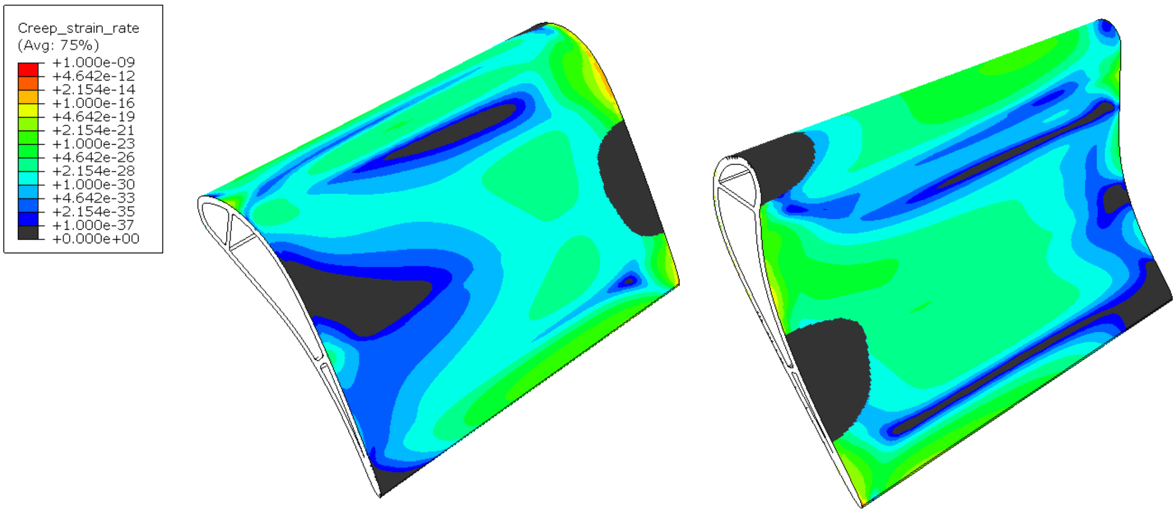
Creep_strain_rate
(Avg: 75%)
+1.000e-09
+4.642e-12
+2.154e-14
+1.000e-16
+4.642e-19
+2.154e-21
+1.000e-23
+4.642e-26
+2.154e-28
+1.000e-30
+4.642e-33
+2.154e-35
+1.000e-37
+0.000e+00

Figure 5.16: Case 3 creep strain rate results.

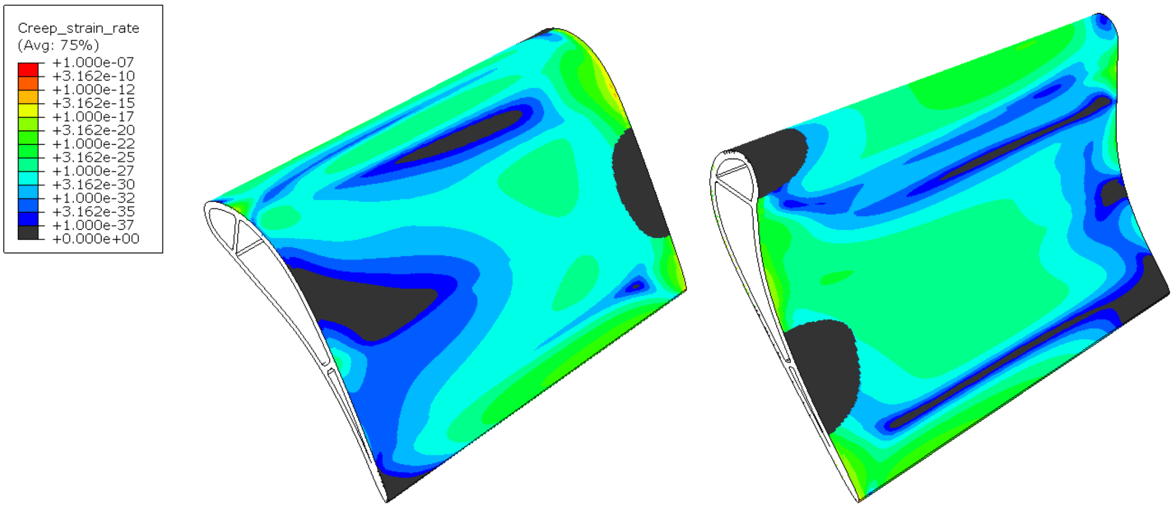
Creep_strain_rate
(Avg: 75%)
+1.000e-07
+3.162e-10
+1.000e-12
+3.162e-15
+1.000e-17
+3.162e-20
+1.000e-22
+3.162e-25
+1.000e-27
+3.162e-30
+1.000e-32
+3.162e-35
+1.000e-37
+0.000e+00

Figure 5.17: Case 4 creep strain rate results.

up for example, this will occur gradually. The results for idle-mode in cases 3 and 4 show that most part of the blade is able to sustain 973 and 545 cycles, respectively. The minimum values of 30 and 31 for cases 3 and 4 are neglected as they occur on the root of the blade due to the encastre boundary condition. For case 1 the trailing edge of the blade is the critical location for LCF. For cases 3 and 4 the trailing edge as well as the root of the blade are the critical locations for LCF.

5.4.2. EFFECT OF COOLING AIR

The effect of the amount of cooling air used can be assessed by comparing case 1 with case 2 for take-off and case 3 with case 4 for idle mode, for which the results are provided in figures 5.14, 5.15, 5.16 and 5.17 for the creep strain rate and in figures 5.21, 5.22, 5.23 and 5.24 for the LCF behaviour. Where 25% of the compressor mass flow is used for cooling in cases 1 and 3, and 20% compressor mass flow is used for cooling in cases 2 and 4.

Again the results for creep strain rate are similar to the Von Mises stress results. The results for cases 1 and 2 show a similar creep strain rate pattern. The location for maximum creep strain rate for both cases is located at the trailing edge. The results for cases 3 and 4 show a similar creep strain rate pattern. The location for maximum creep strain rate for both cases is located at the trailing edge and on the leading edge near the tip of the blade.

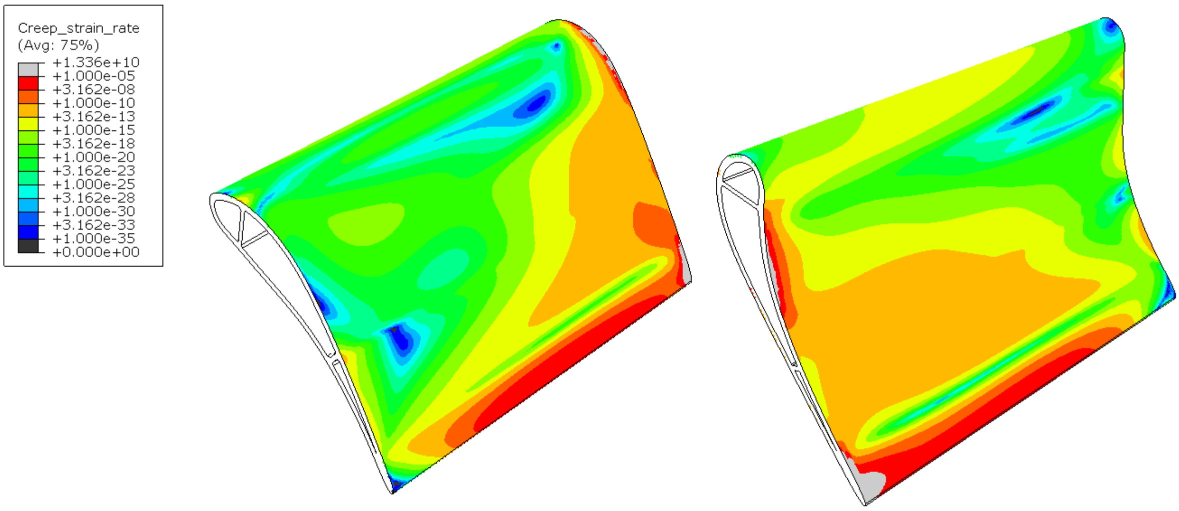
Creep_strain_rate
(Avg: 75%)
+1.336e+10
+1.000e-05
+3.162e-08
+1.000e-10
+3.162e-13
+1.000e-15
+3.162e-18
+1.000e-20
+3.162e-23
+1.000e-25
+3.162e-28
+1.000e-30
+3.162e-33
+1.000e-35
+0.000e+00

Figure 5.18: Case 5 creep strain rate results.

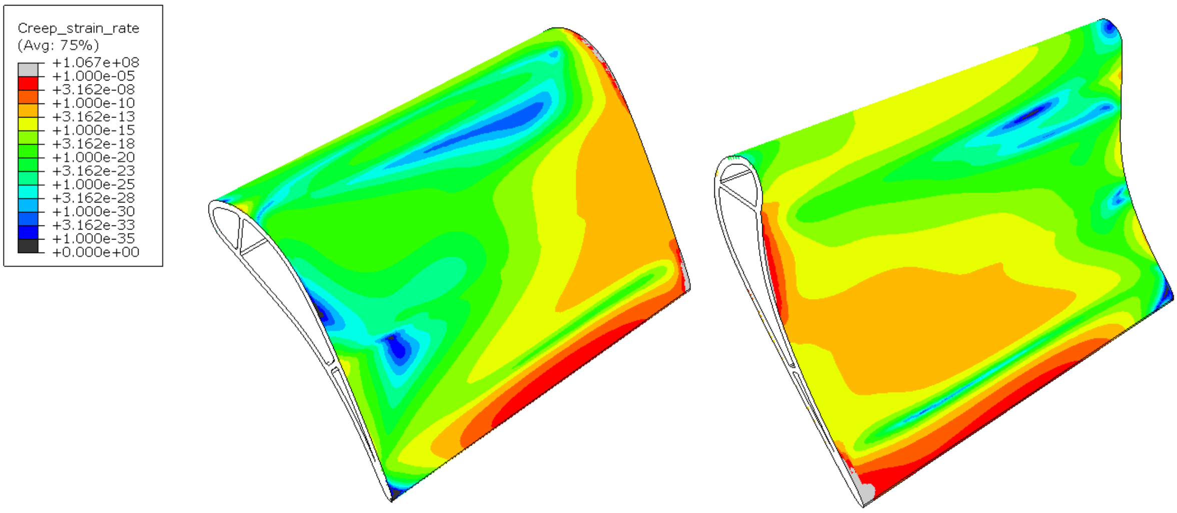
Creep_strain_rate
(Avg: 75%)
+1.067e+08
+1.000e-05
+3.162e-08
+1.000e-10
+3.162e-13
+1.000e-15
+3.162e-18
+1.000e-20
+3.162e-23
+1.000e-25
+3.162e-28
+1.000e-30
+3.162e-33
+1.000e-35
+0.000e+00

Figure 5.19: Case 6 creep strain rate results.

The results for LCF for take-off in cases 1 and 2 show that most part of the blade in case 1 is able to sustain 73 cycles, while most part of the blade in case 2 is able to sustain 70 cycles. This is a decrease of 4%. Overall, the LCF results for case 1 and 2 show a similar pattern. The results for LCF in idle-mode for cases 3 and 4 show that most part of the blade in case 3 is able to sustain 973 cycles and most part of the blade in case 4 is able to sustain 545 cycles, neglecting the minimum found at the root of the blade, because this is caused by the encastre boundary condition. The overall LCF results for cases 3 and 4 show a similar pattern.

5.4.3. EFFECT OF PATTERN FACTOR

The effect of the pattern factor can be assessed by comparing case 1 with case 5, for which the results are provided in figures 5.14 and 5.18 for the creep strain rate and in figures 5.21 and 5.25 for the LCF behaviour. For case 1 a $RTDF$ of 15% is used and for case 5 a $RTDF$ of 10% is used.

The results for the creep strain rate shown that for case 5 the maximum creep strain rate is lower compared to case 1. For both cases the maximum creep strain rate is located at the trailing edge of the blade. The overall creep strain rate however is spread out more over the radial direction, so towards the hub and tip of the blade the creep strain rate for case 5 is higher compared to case 1. Even so, because the maximum creep strain rate is lower for a lower $RTDF$ it can be stated that decreasing the $RTDF$ positively effects the creep strain rate.

The results for LCF show that for case 1 most part of the blade is able to sustain 73 cycles, while for case 5

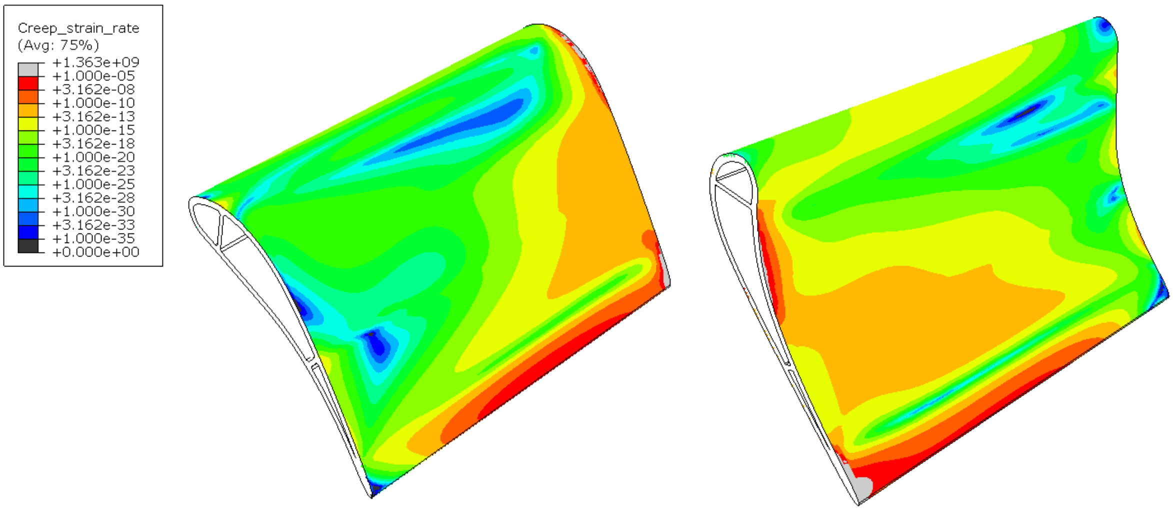
Creep_strain_rate
(Avg: 75%)
+1.363e+09
+1.000e-05
+3.162e-08
+1.000e-10
+3.162e-13
+1.000e-15
+3.162e-18
+1.000e-20
+3.162e-23
+1.000e-25
+3.162e-28
+1.000e-30
+3.162e-33
+1.000e-35
+0.000e+00

Figure 5.20: Case 7 creep strain rate results.

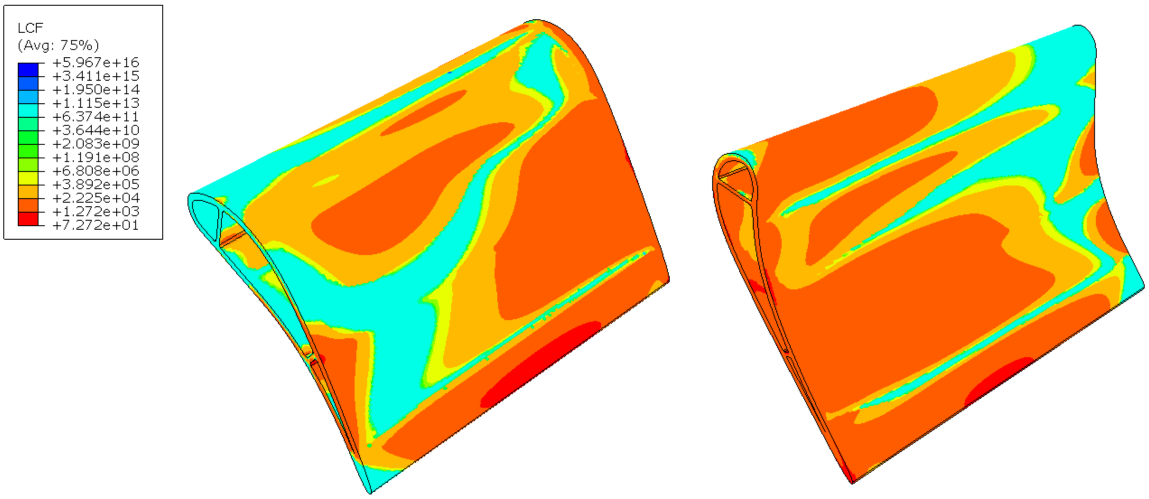
LCF
(Avg: 75%)
+5.967e+16
+3.411e+15
+1.950e+14
+1.115e+13
+6.374e+11
+3.644e+10
+2.083e+09
+1.191e+08
+6.808e+06
+3.892e+05
+2.225e+04
+1.272e+03
+7.272e+01

Figure 5.21: Case 1 low cycle fatigue results.

most part of the blade is able to sustain 64 cycles. This is a decrease of 12%. For both cases the critical location for LCF is found at the trailing edge of the blade. So the decrease in $RTDF$ negatively effects the LCF life.

5.4.4. EFFECT OF TBC THICKNESS

The effect of the TBC thickness can be assessed by comparing case 1 with cases 6 and 7, for which the results are provided in figures 5.14, 5.19 and 5.20 for the creep strain rate and in figures 5.21, 5.26 and 5.27 for the LCF behaviour. For case 1 a TBC thickness of $400\mu m$ is used and for cases 6 and 7 a TBC thickness of $600\mu m$ is used. For case 7 also a lowered $RTDF$ of 10% is used.

Regarding the creep strain rate results for case 1 and case 6 it can be seen that the overall results are slightly lower for the thicker TBC of $600\mu m$ in case 6 compared to case 1 with a TBC thickness of $400\mu m$. The pattern and also the maximum creep strain rate remains the same for both cases. The same can be concluded when comparing case 1 with case 7.

The LCF results for case 1 and case 6 show that the minimum amount of cycles to failure for case 6 is 86 and 73 for case 1. This is an increase of 18%. The location of the maximum creep strain rate is at the trailing edge of the blade and for case 6 also on the root of the blade where the turbulator and pin fin channels start. The overall pattern for both cases is similar. When looking at case 7 and case 1 it can be noted that the minimum amount of cycles to failure for case 7 is 75 cycles compared to 73 cycles for case 1. So the negative

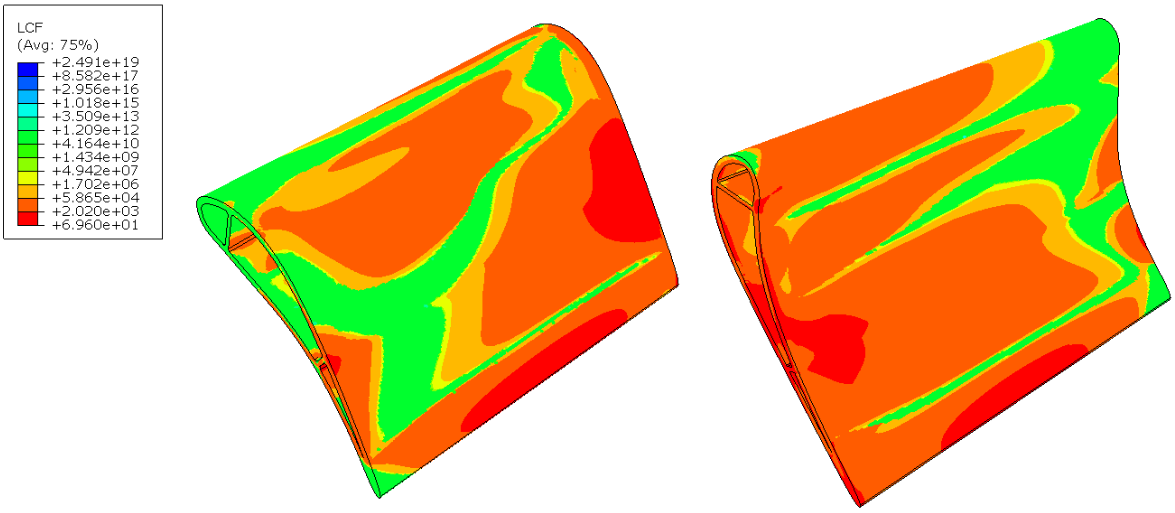

Figure 5.22: Case 2 low cycle fatigue results.

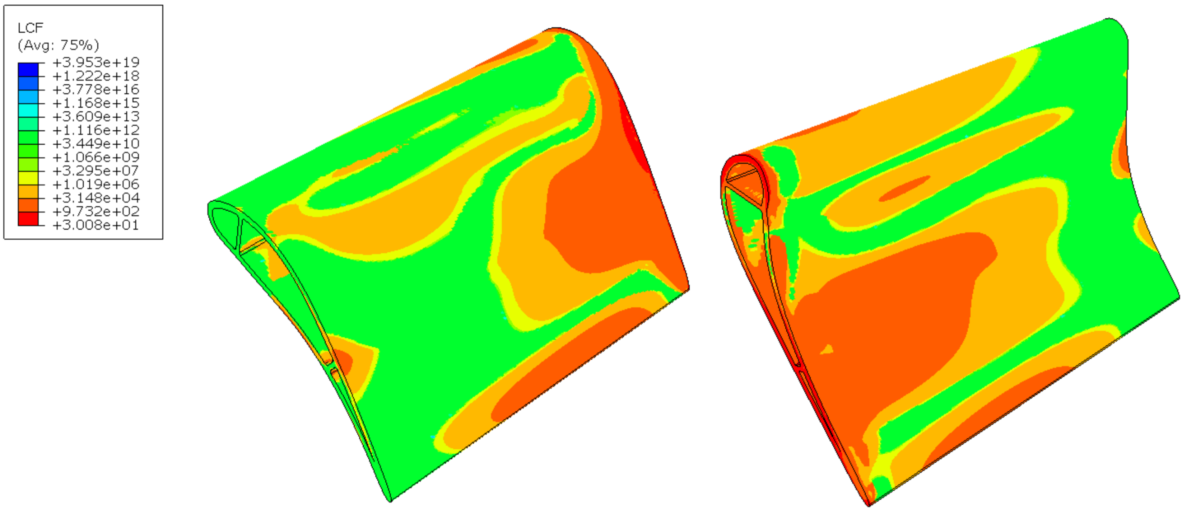

Figure 5.23: Case 3 low cycle fatigue results.

effect on LCF life by a decrease in $RTDF$ is compensated by a positive effect on LCF life by the increase in TBC thickness.

5.5. DISCUSSION ON LIFING ANALYSIS

The methodology used to acquire the results of the thermo-mechanical and lifing analysis consists of assumptions and estimations, especially due to the lack of information regarding the F135 rotor blades geometry and material properties. In order to assess the impact of these assumptions and estimations on the performance of the tool, a critical reflection is provided here, consisting of a discussion of the assumptions and estimations made.

The following assumptions and estimations have been made regarding the thermo-mechanical model and the lifing model.

- Pressure loading is neglected.
- An encastre is placed at the root of the blade as boundary condition.
- CMSX-4 material properties are used for the thermo-mechanical model.
- Inconel 718 material properties are used for the lifing model.

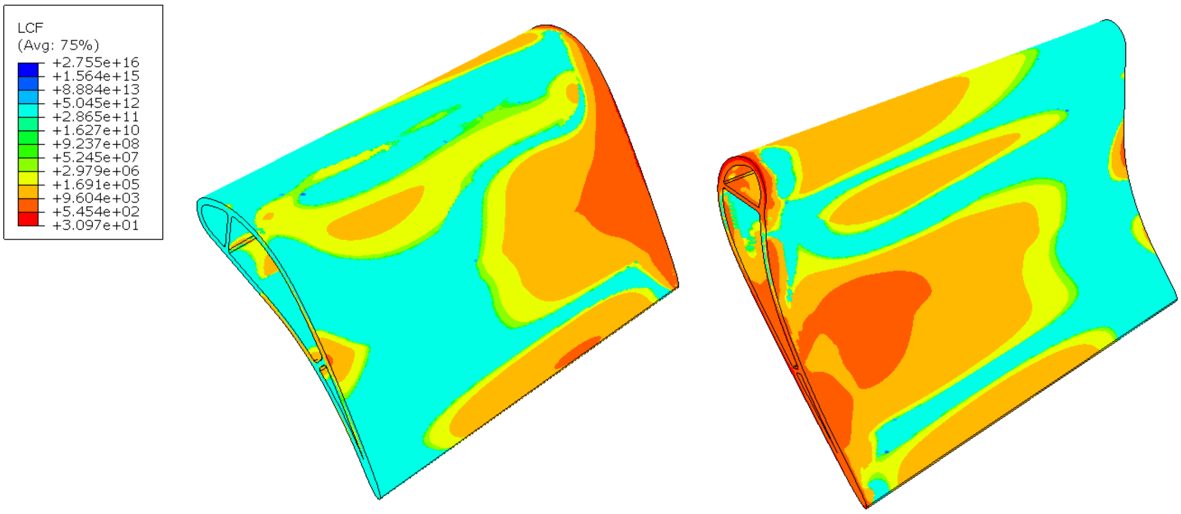

Figure 5.24: Case 4 low cycle fatigue results.

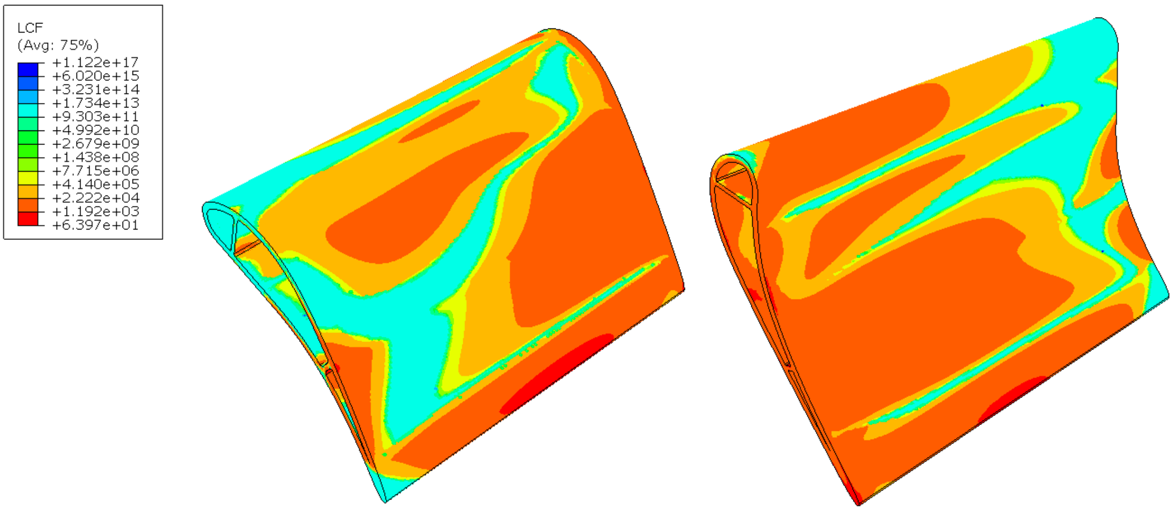

Figure 5.25: Case 5 low cycle fatigue results.

- No interaction between the creep and LCF damage accumulation is considered.
- For the LCF a stress spectrum from zero stress to maximum stress is assumed as one cycle.

From literature it is found that the pressure loading provides about 5% of the total loading on the blade. Considering that the thermal loading for this research are larger compared to the thermal loading as found in literature, this percentage can be expected to be even smaller. Therefore it is a safe assumption to disregard the pressure loading. For future research it is recommended though to include CFD simulations of the flow characteristics around the blade from which the pressure loading can be defined.

As can be seen in the results, the effect of the encastre as boundary condition at the root of the blade is noticeable. Because the purpose of this research focusses on the development of the lifing analysis tool, this effect is acceptable and can be neglected in the results. However, when in the future the tool will be used to perform actual lifing analysis on the F135 rotor blades, it is recommended to include the dovetail.

Although the actual material properties of the F135 rotor blades are expected to be improved with respect to CMSX-4, it is a reasonable assumption to use CMSX-4 because it is also a second generation superalloy, which is also expected for the F135 rotor blades. The actual F135 rotor blade material will most likely perform

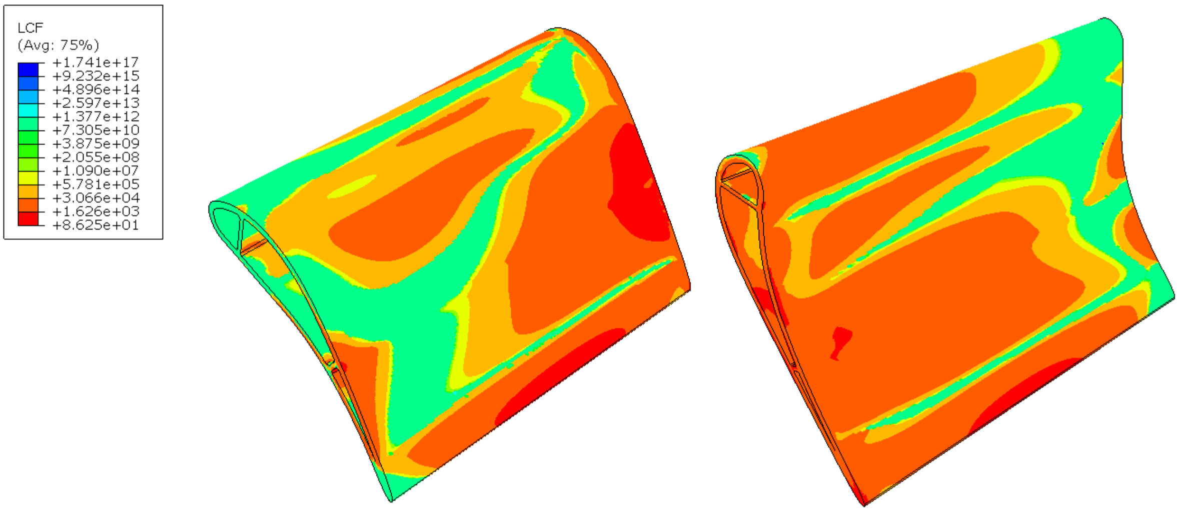
LCF
(Avg: 75%)
+1.741e+17
+9.232e+15
+4.896e+14
+2.597e+13
+1.377e+12
+7.305e+10
+3.875e+09
+2.055e+08
+1.090e+07
+5.781e+05
+3.066e+04
+1.626e+03
+8.625e+01

Figure 5.26: Case 6 low cycle fatigue results.

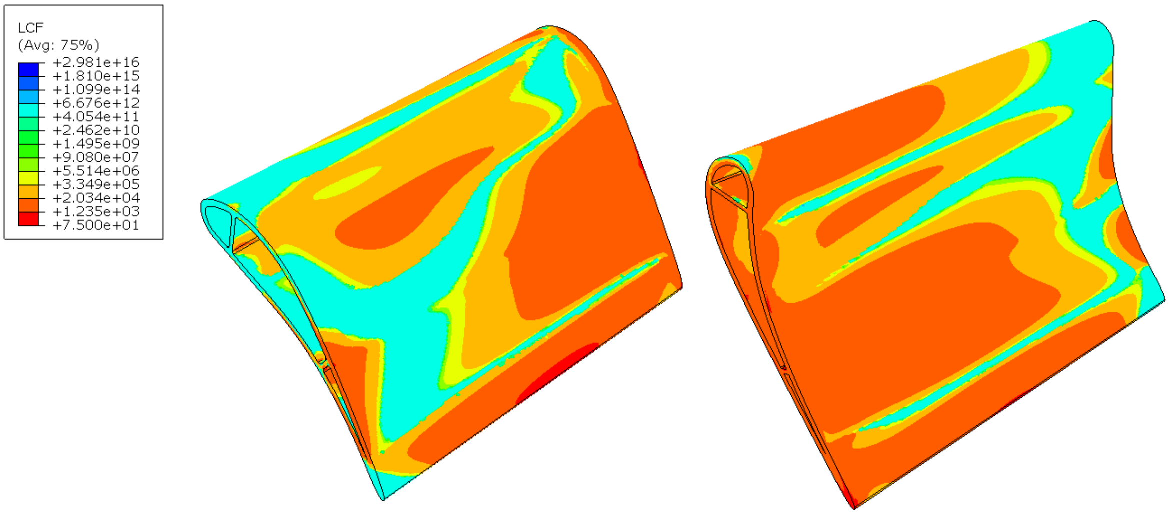
LCF
(Avg: 75%)
+2.981e+16
+1.810e+15
+1.099e+14
+6.676e+12
+4.054e+11
+2.462e+10
+1.495e+09
+9.080e+07
+5.514e+06
+3.349e+05
+2.034e+04
+1.235e+03
+7.500e+01

Figure 5.27: Case 7 low cycle fatigue results.

better in the high-temperature environment compared to CMSX-4, so lower Von Mises stress results are expected for the actual F135 blades.

For the lifing model the material properties of Inconel 718 are used. This material is assumed because this is the only material for which the properties are available for this research. Inconel 718 actually does not posses good creep strain resistance. This can also clearly be seen in the results. Due to this assumption, the magnitude of the creep strain rate results are very inaccurate. However, the overall pattern is still reliable to assess the effects of the parameters as stated in the research questions. For future research it is essential that the creep and fatigue properties of the F135 rotor blade material are available.

The last two assumptions regarding that no interaction between the creep and LCF damage accumulation is considered and that for the LCF a stress spectrum from zero stress to maximum stress is assumed as one cycle follow directly from the lifing analysis model available at the NLR. This lifing analysis model is currently the state-of-the-art at the NLR. For future analysis it is recommended to investigate the performance of the FE-SAFE software package, which is an addition to Abaqus CAE. FE-SAFE features thermo-mechanical fatigue analysis with unique capabilities for creep-fatigue interaction. Because it is developed by the same company as Abaqus CAE, the interaction between the programs might be very suitable.

5.6. FUTURE RESEARCH

As stated repetitively, for future research it is recommended to acquire the actual geometry and material properties for the F135 rotor blades. Without the exact material properties it is not possible to generate accurate results regarding creep and LCF behaviour. Next to this it is recommended to generate a CFD model based on the actual geometry of the F135 rotor blades, from which the pressure loading on the blade can be determined. From the actual geometry also the dovetail configuration can be implemented. Lastly, it is recommended to investigate the possibilities of the FE-SAFE program, which features thermo-mechanical fatigue analysis with unique capabilities for creep-fatigue interaction. Since this is developed by the same company as Abaqus CAE a good interaction between both programs might be possible.

6

CONCLUSIONS AND RECOMMENDATIONS

In this chapter the conclusions and recommendations regarding the research are provided. The conclusions are divided into conclusions considering the gas turbine simulation model, the heat transfer model, the thermo-mechanical model, the lifing model and general conclusions. These conclusion will answer the research questions as stated in chapter 1.

6.1. CONLUSIONS

The objective of this research was to develop a preliminary lifing analysis tool for the F135-PW-100 engine by designing a thermodynamic model coupled to a lifing model. A thermodynamic model has been developed and successfully been coupled to a lifing model. Therefore the objective of this research has been achieved.

Regarding the research question to what extend the methodology of previous lifing analysis as performed by the NLR can be applied to this research the following can be stated. Most part of the methodology as previously integrated in the lifing analysis was also applicable to this research. Two differences are that for previous analyses also flight data could be recorded and coupled to the model. No flight data was available yet for this research since it is proprietary information. When flight data is available in the future, the GSP model designed in this research offers good possibilities to integrate the flight data. Another difference is that for previous research a CFD model could be coupled to perform the heat transfer analysis. Without access to the detailed geometry of the F135 rotor blades, a CFD model has been replaced by an analytical model in Matlab for this research.

The gas turbine simulation model has been designed in GSP using performance data found in open source literature, theory to determine the unknown engine characteristics and lastly analysis by synthesis to optimize the design point. The model shows stable behaviour for the design point, as well as for afterburner mode and for off-design analysis. The design point shows the following main characteristics for take-off.

- Inlet mass flow of $147\frac{kg}{s}$.
- Bypass ratio of 0.57.
- Fuel flow of $3.15\frac{kg}{s}$.
- Turbine inlet temperature of $2175K$.
- Dry thrust of $125903N$.
- Overall pressure ratio of 28.2.
- Thrust specific fuel consumption of $0.090\frac{kg}{Nh}$.

The most interesting differences compared to the F100-PW-220 engine which powers the F-16 are the increase in inlet mass flow, fuel flow and turbine inlet temperature. The inlet mass flow has been increased with 44%, the mass flow has been increased with 142% and the turbine inlet temperature has approximately been increased with 18%.

A heat transfer model has been developed in Matlab and Abaqus CAE. The temperatures have been derived from theory and the heat transfer coefficients have been estimated using Nusselt number correlations.

The correlations found were suitable to integrate into the model, without knowing much about the geometry. Next to the heat transfer model, a thermodynamic model and lifing model have been developed in Abaqus CAE. For the thermo-mechanical model thermal loading en centrifugal loading are applied. Case studies have been performed to assess the affect of variations in the power setting, the amount of cooling air, the pattern factor and the TBC thickness. For all cases the trailing edge of the blade is found to be the most critical location. The following can be concluded on the effect of the power setting.

- The maximum temperature at take-off is found to be $1427K$. At idle-mode this temperature is reduced with 35%. The location of maximum temperature for both cases is at the trailing edge of the blade.
- For take-off the maximum Von Mises stress found is in the order of $550MPa$, for idle this is decreased to the order of $300MPa$.
- The creep strain rate shows similar results as the Von Mises stress.
- For take-off most part of the blade is able to sustain 73 cycles, for idle mode this is increased to 973 cycles.

The following can be concluded regarding the effects of the amount of cooling air.

- When decreasing the amount of cooling air by 5% and increase of maximum temperature of approximately 1% is found. The location of the maximum temperature remains the same for both situations, at the trailing edge of the blade.
- No significant difference is found in the Von Mises stresses.
- The creep strain rate shows similar results as the Von Mises stress.
- When decreasing the amount of cooling air by 5% the amount of cycle to LCF failure is reduced with 4%.

The following can be concluded regarding the effects of the pattern factor.

- When decreasing the $RTDF$ by 5% a decrease in maximum temperature of approximately 2% is found. The temperatures on the root and tip of the blades have been increased by approximately 2%.
- No significant difference is found in the Von Mises stresses.
- Decreasing the RTDF positively effects the creep strain rate.
- When decreasing the $RTDF$ by 5% a decrease of 12% is found for the cycles to LCF failure.

The following can be concluded regarding the effects of the TBC thickness.

- When increasing the TBC thickness from $400\mu m$ to $600\mu m$ the maximum temperature is decreased by approximately 4%.
- No significant difference is found in the Von Mises stresses.
- Increasing the TBC thickness provides slightly lower creep strain rate results.
- When increasing the TBC thickness from $400\mu m$ to $600\mu m$ an increase of 18% is found for the cycles to LCF failure.

6.2. RECOMMENDATIONS

For this research a lifing analysis tool has been developed on a preliminary level, based on open source literature data. For future development of the tool the following improvements considering the data validation, but also the methodology are proposed.

- It is recommended to get access to the performance data, material data and detailed geometry data of the rotor blades of the F135 engine. When this data is available, the gas turbine simulation model can be validated. Also performance data regarding the combustor exit temperature profile would be a great addition to determine the actual radial and circumferential temperature distribution. Regarding the detailed geometry it is advised to build a CFD model to perform the heat transfer analysis. With the material data, exact life prediction can be provided by the lifing model.
- For future operability of the gas turbine simulation model transient simulations based on recorded flight data are preferred. In this manner the actual operations performed with the engine can be coupled to the lifing model.
- Currently an assumption for the blade wall temperature is used to determine the radiation heat transfer coefficient and the internal temperature distribution. For future research it is recommended to either implement an iteration between the blade temperature calculations and the external and internal heat

transfer characteristics or use a conjugate heat transfer methodology. For computation efficiency a conjugate heat transfer analysis could be implemented in the CFD model in which the calculations of the external and internal flow and heat transfer are coupled together with the blade conduction.

- Lastly, it is recommended to look into the possibilities of using the program FE-SAFE, which features thermo-mechanical fatigue analysis with unique capabilities for creep-fatigue interaction. Since this is developed by the same company as Abaqus CAE a good interaction between both programs might be possible.

A

GAS TURBINE SIMULATION PROGRAM

In this appendix the theory behind the performance simulations within GSP will be summarised. The theory in this appendix is summarised from [23] and [45].

A.1. PERFORMANCE SIMULATION

For the design of a gas turbine engine, several design points exist which correspond to a certain level of performance required, e.g. take-off power or end-of climb power. Therefore, each design point (DP) is critical for the application of the engine. A gas turbine engine is optimized for these operating conditions. Operating conditions outside of the DP scope, such as changes in power setting or atmospheric conditions, the gas turbine exhibits off-design (OD) performance. For performance simulation in GSP, one DP is required as reference, the reference point (RP).

At OD conditions, differences can occur for the components with respect to the reference performance. For steady-state OD performance calculations, the assumption is made that all parameters are time-independent, leading to a set of time-independent non-linear differential equations representing the engine, satisfying the mass, energy and momentum conservation equations.

Transient performance includes the time variation of state variables. By integrating the time derivatives in the equations representing the model, the transient engine behaviour is modelled in a quasi steady-state.

In GSP the various component performance levels are matched to each other such that the conservation laws are satisfied. In order to model the component performance characteristics, a number of performance parameters are described. Dimensional analysis is used to minimise the number of performance parameters, to the four parameters as provided in table A.1. In table A.1 also the corrected parameters are provided. These corrected parameters are normalized to ambient atmospheric conditions. Furthermore, θ and δ can be described as in equation A.1 and A.2, respectively.

$$\theta = \frac{T}{T_{amb}} \qquad \text{(A.1)}$$

$$\delta = \frac{P}{P_{amb}} \qquad \text{(A.2)}$$

Table A.1: Non-dimensional and corrected parameters used for component performance.

Description	**Non-dimensional parameter**	**Corrected parameter**
Mass flow	$\frac{\dot{m}\sqrt{R \cdot T_{inl}}}{P_{inl} D^2}$	$\frac{\dot{m}\sqrt{\theta}}{\delta}$
Shaft rotational speed	$\frac{N \cdot D}{\sqrt{R \cdot T_{inl}}}$	$\frac{N}{\sqrt{\theta}}$
Pressure ratio	$\frac{P_{inl}}{P_{exit}}$	$\frac{P_{inl}}{P_{exit}}$
Efficiency	η	η

As a fifth parameter, the Reynolds number is required. However, since the performance effects due to Reynolds number variations due to changes in altitude are mostly small, it can be neglected. The main effect of the Reynolds number is on the component efficiency. In GSP, this can be taken into account.

Since the working medium is fixed in a specific gas turbine configuration, the universal gas constant R often is omitted from the non-dimensional parameters. Also, because the gas turbine simulation model considers the same machine, the diameter D will remain constant and can be omitted.

A.2. SOLUTION METHODOLOGY

To explain the solution method, a simple five component GSP turbojet gas turbine model will be used as example. The model is shown in figure A.1. the gas path components used in this model are an inlet, a compressor, a combustor, a turbine and an exhaust. An engine control component is added above the combustor to control the fuel flow.

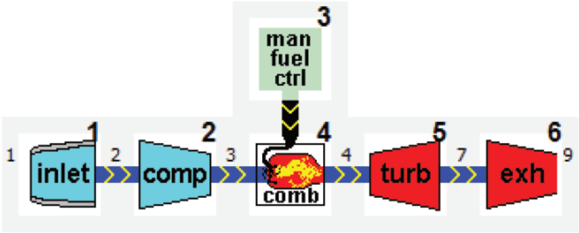

Figure A.1: Example five component gas turbine model in GSP

In GSP, the operating point of the engine is numerically represented by the models state vector, which is subsequently defined by the state variables. For this basic turbojet model containing five gas path components, four state variables are required to specify the model state. The state vector for this basic turbojet model is provided in equation A.3. The state variables are normalised in order to avoid numerical instabilities.

$$\overline{S} = \begin{bmatrix} s_1 \\ s_2 \\ s_3 \\ s_4 \end{bmatrix} = \begin{bmatrix} \frac{W}{W_{des}} \\ \frac{N}{N_{des}} \\ \frac{\beta_c}{\beta_{c,des}} \\ \frac{\beta_t}{\beta_{t,des}} \end{bmatrix} \tag{A.3}$$

The first state variable considers the air mass flow. The air mass flow is required to define the state of the inlet component. The second and third state variable come forth of the compressor component. The design point of the compressor contain the shaft speed, pressure ratio and the isentropic efficiency. To combine the latter two, a β parameter is defined. This β parameter is represented by β-lines in the compressor map. These lines are used to provide a relation between the corrected mass flow and the pressure ratio. The last state variable represents a similar β parameter, but then for the turbine component. For this turbojet model, the purpose of the turbine is to drive the compressor. The parameters used to define the operating point of the turbine are combined in the turbine component map. Also in this map β-lines are used to relate the mass flow and pressure ratio. No extra state-variables are required for the combustor, since the fuel flow, the combustion efficiency and the pressure loss are user specified.

To obtain a valid operating point, all component model performance should match each other and all conservation laws should be satisfied. In order to achieve this, error equations are defined. When the maximum relative error is below a user specified iteration accuracy threshold, an operating point is stated valid. For the example model the error equations are as defined in equation A.4.

$$\begin{aligned} E_1 &= W_2 f(s_1) - W_{comp} f(s_2, s_3) \\ E_2 &= P_{comp} - P_{turb} \\ E_3 &= W_4 - W_{turb} f(s_2, s_4) \\ E_4 &= W_7 f(s_2, s_4) - W_{exh} f(A_9, P_7, T_7) \end{aligned} \tag{A.4}$$

In GSP a multi-variable Newton-Raphson algorithm is used to iteratively determine an approximation of a valid OD point. The error equations are linearised for the initial state (usually the DP). For all error equations the partial derivative with respect to each state variable is determined. These partial derivatives together form the *Jacobian matrix* of $m \times m$, see equation A.5, m being the number of state variables.

$$J = \begin{bmatrix} \frac{\delta E_1}{\delta S_1} & \cdots & \frac{\delta E_m}{\delta S_m} \\ \vdots & \ddots & \vdots \\ \frac{\delta E_1}{\delta S_m} & \cdots & \frac{\delta E_m}{\delta S_m} \end{bmatrix} \tag{A.5}$$

For the current operating point, defined by state vector $\overline{S}$, the Jacobian represents a linear approximation of the non-linear gas turbine model. This is analytically formed in equation A.6.

$$\Delta\overline{E} = \mathbf{J} \cdot \Delta\overline{S} \tag{A.6}$$

Rewriting equation A.6 by taking the inverse of the Jacobian and by looking at a small variation between two operating stages, equation A.6 can be rewritten as described in equation A.7. the new equilibrium operating point is determined through equation A.7.

$$\overline{S_{i+1}} = \overline{S_i} + \mathbf{J^{-1}} \cdot \Delta\overline{E_i} \tag{A.7}$$

In order to prevent the overshoot of one or more error variables, a default change of 5% per iteration step is defined for each state variable. This is done by adding a scaling factor to equation A.7. With the scaling factor, the final equation for the iterative process is provided in equation A.8.

$$\overline{S_{i+1}} = \overline{S_i} + f \cdot \mathbf{J^{-1}} \cdot \Delta\overline{E_i} \tag{A.8}$$

B

LOAD CASES RESULTS FROM GSP

In this appendix the results from GSP for four case studies are provided. The case studies that have been analysed are the following.

- Load case 1:
    - Cooling air mass flow of 25% of the compressor exit mass flow is used.
    - Engine load situation at take-off is considered.
- Load case 2:
    - Cooling air mass flow of 20% of the compressor exit mass flow. This is divided in 16% HPT cooling and 4% LPT cooling
    - Engine operation at take-off is considered.
- Load case 3:
    - Cooling air mass flow of 25% of the compressor exit mass flow is used.
    - Engine operation at cruise, so idle-mode is considered. For idle-mode a TIT of 1200K is used.
- Load case 4:
    - Cooling air mass flow of 20% of the compressor exit mass flow. This is divided in 16% HPT cooling and 4% LPT cooling
    - Engine operation at cruise, so idle-mode is considered. For idle-mode a TIT of 1200K is used.

The above four case studies are analysed with GSP and the results of GSP are subsequently used as input for the thermal and mechanical analysis. The results as shown in table B.1 are used as input for the thermal and mechanical analysis.

Table B.1: Results for load cases 1, 2, 3 and 4.

Parameter	**Case 1**	**Case 2**	**Case 3**	**Case 4**	**Unit**
W_{25}	93.63	93.63	37.30	37.51	$\frac{kg}{s}$
W_4	73.14	78.03	28.37	30.44	$\frac{kg}{s}$
W_{41}	84.38	88.02	32.85	34.44	$\frac{kg}{s}$
W_{45}	89.99	93.01	35.10	36.45	$\frac{kg}{s}$
W_F	3.15	3.36	0.50	0.53	$\frac{kg}{s}$
T_{t_3}	807.8	807.8	543.6	544.4	K
T_{t_4}	2175	2175	1200	1200	K
$T_{t_{41}}$	2013.7	2037.9	1117.1	1129.5	K
$T_{t_{45}}$	1672.4	3.36	0.50	0.53	K
P_{t_3}	25.716	25.716	7.403	7.443	Bar
$P_{t_{41}}$	24.688	24.688	2.968	3.111	Bar
ρ_{t_4}	3.922	3.922	2.025	2.036	$\frac{kg}{m^3}$
$\rho_{t_{41}}$	3.922	3.922	2.025	2.036	$\frac{kg}{m^3}$
C_{P_3}	1100.5	1100.5	1038.4	1038.6	$\frac{J}{kgK}$
C_{P_4}	1376.0	1376.0	1211.4	1211.4	$\frac{J}{kgK}$
$C_{P_{41}}$	1349.3	1353.4	1192.3	1195.2	$\frac{J}{kgK}$
$C_{P_{45}}$	1349.3	1353.4	1192.3	1195.2	$\frac{J}{kgK}$
R_3	287.05	287.05	287.05	287.05	$\frac{J}{kgK}$
R_4	287.17	287.17	287.03	287.03	$\frac{J}{kgK}$
R_{41}	287.15	287.15	287.03	287.03	$\frac{J}{kgK}$
R_{45}	287.00	287.00	287.03	287.03	$\frac{J}{kgK}$
μ_{41}	$7.14 \cdot 10^{-5}$	$7.14 \cdot 10^{-5}$	$4.83 \cdot 10^{-5}$	$4.83 \cdot 10^{-5}$	$\frac{Ns}{m^2}$
γ_3	1.353	1.353	1.382	1.382	$[-]$
γ_4	1.264	1.264	1.311	1.311	$[-]$
γ_{41}	1.268	1.267	1.312	1.312	$[-]$
γ_{45}	1.280	1.278	1.334	1.332	$[-]$
RPM_2	15200	15200	12020	12031	$[-]$

C

Material Properties

This appendix provides the material properties for CMSX-4 and the TBC.

C.1. CMSX-4 Properties

For the analysis the material properties of the superalloy CMSX-4 will be used. This is a second generation Nickel-based superalloy. As was mentioned in section 2.4, a second generation superalloy can be expected for the F135 rotor blades. The material properties for CMSX-4 are provided in tables C.1 and C.2. The density of CMSX-4 is $8.0\frac{kg}{m^3}$. These material properties are provided by the NLR. The yields strength as a function of temperature for CMSX-4 is provided in figure C.1.

Table C.1: Thermal conductivity and expansion and specific heat of CMSX-4.

Thermal conductivity $\frac{W}{mK}$	**Temperature** K	**Thermal expansion** $\frac{m}{mK}$	**Temperature** K	**Specific heat** $\frac{J}{kgK}$	**Temperature** K
17.3	810	$1.30 \cdot 10^{-5}$	298	$481 \cdot 10^{6}$	537
22.0	1033	$1.35 \cdot 10^{-5}$	700	$607 \cdot 10^{6}$	1093
28.2	1255	$1.59 \cdot 10^{-5}$	1144		
		$1.80 \cdot 10^{-5}$	1366		

Table C.2: Elastic properties of CMSX-4.

Young's modulus MPa	**Poisson ratio** –	**Shear modulus** MPa	**Temperature** K
124883	0.35	133418	293
122653	0.35	130283	373
114966	0.35	122307	573
106594	0.35	116626	773
102398	0.36	112769	873
97540	0.36	109062	973
94779	0.36	106869	1023
91967	0.36	104518	1073
88426	0.36	102397	1123
84351	0.36	100187	1173
79162	0.36	99078	1223
72958	0.37	94727	1273

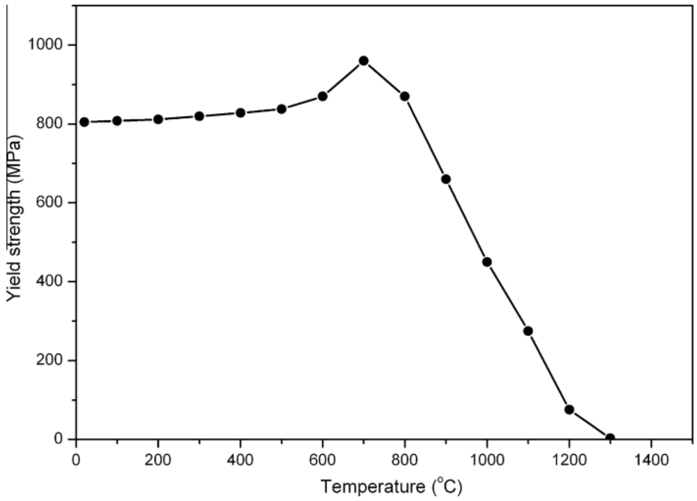

Figure C.1: Yield strength of CMSX-4 over temperature. [46]

C.2. TBC PROPERTIES

For the thermal barrier coating a conductivity of $0.8\frac{W}{mK}$ is assumed and the thickness is assumed to vary between $400-600\mu m$. The effect of the TBC will be incorporated in the heat transfer coefficient as was shown in equation 4.30. [37]

BIBLIOGRAPHY

[1] Ministerie van Defensie nederland kan motoronderhoud f-35 uitvoeren. `https://www.defensie.nl/actueel/nieuws/2014/12/11/nederland-kan-motoronderhoud-f-35-gaan-uitvoeren`. Accessed: 2017-05-04.

[2] C. Bolkcom. Joint strike fighter (jsf) program: Background, status, and issues. Library of Congress Washington DC Congressional Research Service, 2003.

[3] Lockheed Martin Aeronautics Company f-35 lightning ii. `http://www.lockheedmartin.com/us/products/f35.html`. Accessed: 2017-05-12.

[4] P.M. Bevilaqua. Inventing the f-35 joint strike fighter. In *47th AIAA Aerospace Sciences Meeting Including the New Horizons Forum and Aerospace Exposition, Orlando, Florida. AIAA*, volume 1650, 2009.

[5] M. Daly. *Jane's Aero-engines, issue 22*. IHS, 2007.

[6] Pratt & Whitney f135 engine for f-35a conventional takeoff and landing (ctol). `http://www.pw.utc.com/F135_Engine`. Accessed: 2017-05-12.

[7] B.L. Koff. Gas turbine technology evolution: a designers perspective. *Journal of propulsion and power*, 20(4):577–595, 2004.

[8] S. Trimble. The heat is on. *Flight International*, pages 22–25, 2013.

[9] S.W. Kandebo. Pratt claims record turbine temps in jsf engine tests. *Aviation Week & Space Technology*, 154(25):76–76, 2001.

[10] Han et al. *Gas Turbine Heat Transfer and Cooling Technology*. Taylor & Francis, 2000.

[11] A. Giampaolo. *Gas Turbine Handbook*. The Fairmount Press, 2006.

[12] O. Younossi et al. Military jet engine acquisition: Technology basics and cost-estimating methodology. Technical report, RAND Corp. Santa Monica CA, 2002.

[13] J. Kurzke. Preliminary design, von karman institute for fluid dynamics lecture series 2002–2003. *Aero Engine Design: A State of the Art*, 2003.

[14] A.S. Lee et al. Modeling of the performance of a f100-pw229 equivalent engine under sea-level static conditions. In *45th AIAA/ASME/SAE/ASEE Joint propulsion conference and exhibit*, 2009.

[15] G.W. Goward. Progress in coatings for gas turbine airfoils. *Surface and coatings technology*, 108:73–79, 1998.

[16] Wadley Research Group high temperature coatings. `http://www.virginia.edu/ms/research/wadley/high-temp.html`. Accessed: 2017-06-07.

[17] J.C. Williams et al. Progress in structural materials for aerospace systems. *Acta Materialia*, 51(19):5775–5799, 2003.

[18] G.A. Danko. By leaps and bounds: The realization of jet propulsion through innovative materials and design. In *Key Engineering Materials*, volume 380, pages 135–146. Trans Tech Publ, 2008.

[19] N.P. Padture et al. Thermal barrier coatings for gas-turbine engine applications. *Science*, 296(5566):280–284, 2002.

[20] W. Gostic. Application of materials and process modeling to the design, development and sustainment of advanced turbine engines. *Superalloys 2012*, pages 1–12, 2012.

[21] C.J. Daniele J.F. Sellers. Dyngen: A program for calculating steady-state and transient performance of turbojet and turbofan engines. 1975.

[22] W.P.J. Visser. Gas turbine engine simulation at nlr. Technical report, Netherlands Aerospace Laboratory, 11 1995.

[23] W.P.J. Visser et al. Technical manual of the gas turbine simulation program. Technical report, NLR, 04 2014.

[24] Philip P Walsh and Paul Fletcher. *Gas turbine performance*. John Wiley & Sons, 2004.

[25] Dr. M. Gallo. *Heat Transfer Basics, Lecture 5*. AE4237: Heat Transfer Problems in Gas Turbines (Delft University of Technology). 09 2015.

[26] Rama SR Gorla and Aijaz A Khan. *Turbomachinery: design and theory*. CRC Press, 2003.

[27] Dr. Ir. M. Pini. *Turbines, Lecture 7*. AE4206: Turbomachinery). 11 2016.

[28] RCW De Koning. Development of a parametric 3d turbomachinery blade modeler. 2015.

[29] Arthur H Lefebvre. *Gas turbine combustion*. CRC press, 1998.

[30] S. Colantuoni et al. Aero-thermal design of a cooled transonic ngv and comparison with experimental results. *AGARD, Heat Transfer and Cooling in Gas Turbines 25*, 1993.

[31] S Larry Dixon and Cesare Hall. *Fluid mechanics and thermodynamics of turbomachinery*. Butterworth-Heinemann, 2013.

[32] A.B. Mehendale et al. Influence of high mainstream turbulence on leading edge heat transfer. *Journal of Heat Transfer*, 113(4):843–850, 1991.

[33] A.J. Glassman. *Turbine Design and Application*. NASA, 1994.

[34] H. Cohen et al. *Gas Turbine Theory*. Longman Group Limited, 1996.

[35] Ethirajan Rathakrishnan. *Instrumentation, measurements, and experiments in fluids*. CRC Press, 2007.

[36] EA Avallone, IT Baumeister, and Ali Sadegh. *Marks' Standard Handbook for Mechanical Engineers. 10*. New York: McGraw-Hill, 2006.

[37] Julian D Osorio, Alejandro Toro, and Juan P Hernandez-Ortiz. Thermal barrier coatings for gas turbine applications: failure mechanisms and key microstructural features. *Dyna*, 79(176):149–158, 2012.

[38] George P Liang. Turbine blade with multi-pass cooling and cooling air addition, October 31 2000. US Patent 6,139,269.

[39] R. Viskanta A.M. Huber. Effect of jet-jet spacing on convective heat transfer to confined, impinging arrays of axisymmetric air jets. *International Journal of Heat and Mass Transfer*, 37(18):2859–2869, 1994.

[40] J. Taler D. Taler. Simple heat transfer correlations for turbulent tube flow. In *E3S Web of Conferences*, volume 13. EDP Sciences, 2017.

[41] S Acharya, V Eliades, and DE Nikitopoulos. Heat transfer enhancements in rotating two-pass coolant channels with profiled ribs: Part 1—average results. In *ASME Turbo Expo 2000: Power for Land, Sea, and Air*, pages V003T01A035–V003T01A035. American Society of Mechanical Engineers, 2000.

[42] D.E. Metzger et al. Developing heat transfer in rectangular ducts with staggered arrays of short pin fins. *Journal of Heat Transfer*, 104(4):700–706, 1982.

[43] Satoshi Hada and Taku Ichiryu. Turbine blade and gas turbine, May 22 2012. US Patent 8,182,203.

[44] W.F. Lammen et al. Phm demonstrator for small gas turbines. Technical report, Netherlands Aerospace Laboratory, 11 2016.

[45] M.L. Verbist. Gsp modelling elements and numerical methods. Technical report, Delft University of Technology, 02 2013.

[46] Chinnapat Panwisawas, Harshal Mathur, Jean-Christophe Gebelin, Duncan Putman, Catherine MF Rae, and Roger C Reed. Prediction of recrystallization in investment cast single-crystal superalloys. *Acta Materialia*, 61(1):51–66, 2013.